

STRUCTURE AND REACTIVITY OF VICINAL Pt AND LOW-INDEX Cu/Pd SURFACES

THÈSE N° 1218 (1994)

PRÉSENTÉE AU DÉPARTEMENT DE PHYSIQUE

ÉCOLE POLYTECHNIQUE FÉDÉRALE DE LAUSANNE

POUR L'OBTENTION DU GRADE DE DOCTEUR ÈS SCIENCES

PAR

ELMAR HAHN

Physicien diplômé de la Rheinische Friedrich-Wilhelms-Universität, Bonn
de nationalité allemande

acceptée sur proposition du jury:

Prof. K. Kern, rapporteur
Prof. W. Benoit, corapporteur
Prof. G. Comsa, corapporteur
Prof. W. D. Schneider, corapporteur
Prof. K. Wandelt, corapporteur

Lausanne, EPFL
1994

Résumé

Cette thèse concerne l'étude de la structure et de la réactivité de surfaces métalliques, par microscopie à effet tunnel et spectroscopie infrarouge.

La structure de la face vicinale (997) du platine a été étudiée par microscopie à effet tunnel. A température ambiante, la surface montre une structure très régulière, avec des terrasses dont la largeur moyenne est de 20.2\AA avec une distribution des largeurs très étroite. La face vicinale subit deux transitions de phases structurales. La largeur des terrasses et la hauteur des marches sont doublées par un recuit à une température comprise entre 600K et 900K dans une atmosphère de $5 \cdot 10^{-8}$ mbar d'oxygène. Au-dessus de 950K, on observe la formation de larges facettes (111) dont l'extension s'accroît si la température augmente. Les facettes sont toujours en coexistence avec des régions à structure initiale (997). Cette transition de phase est apparemment causée par la forte tendance des terrasses (111) de platine à se reconstruire.

Les spectres vibrationnels de molécules (CO , $\text{CO} + \text{H}_2$, N_2O , NO_2) adsorbées sur du Pt(997) ont été étudiés par spectroscopie infrarouge. Le CO occupe en priorité les sites localisés sur les marches du substrat avant de s'adsorber sur les terrasses où le CO forme une structure $c(4 \times 2)$. En présence d'une atmosphère d'hydrogène à $T_S > 150\text{K}$, le CO préadsorbé désorbe. En revanche, la saturation de la surface par une monocouche complète d'hydrogène à $T_S = 165\text{K}$ empêche l'adsorption subséquente de CO ou d'autres molécules, sans changer pour autant la structure de la surface. La mise en évidence de cette méthode de passivation chimique ainsi que l'obtention d'une structure régulière de Pt(997) suggèrent la possibilité d'utiliser cette surface en tant qu'élément optique pour des jets atomiques. Le NO_2 et le N_2O s'adsorbent sans se dissocier à la surface et forment des multicouches solides à $T_S < 100\text{K}$.

La croissance des couches minces de cuivre sur la face (110) du palladium ainsi que l'adsorption du CO sur ce système ont été étudiées. L'anisotropie de diffusion des adatoms sur cette surface détermine la forme des îlots de cuivre. A basse température ($\leq 300\text{K}$), les adatoms se déplacent exclusivement le long de la direction $[1\bar{1}0]$ du

substrat, ce qui conduit à la formation d'agrégats 1D à bas recouvrement (≤ 0.1 monocouches). A $T_S > 300\text{K}$, la migration le long de $\{001\}$ est activée et l'on observe la formation d'îlots 2D. Une analyse quantitative de la forme des îlots en fonction de la température a été effectuée en vue de déterminer les barrières de diffusion le long de $[1\bar{1}0]$ (0.51eV) et de $[001]$ (0.75eV).

En fonction de la température de déposition, trois types de croissance de films minces de Cu sur Pd(110) sont observés. A $T_S < 400\text{K}$, une croissance 3D a lieu. Entre 400K et 500K , la première couche de Cu est complétée avant que la nucléation des îlots 3D commence. Entre 500K et 700K , on observe une croissance couche par couche. Des films plus épais que 5 monocouches sont comprimés le long de $[1\bar{1}0]$.

Sur des surfaces Cu/Pd(110) avec $\Theta_{Cu} < 1$, le CO occupe à $T_S = 150\text{K}$ non seulement des sites au-dessus d'un atome de Cu et entre deux atomes de Pd, comme on pourrait s'y attendre par comparaison avec les métaux isolés, mais occupe aussi des sites au-dessus d'un atome de Pd. Ce changement de site d'adsorption induit par la présence de Cu indique une modification "chimique" du substrat. Cette modification est d'un caractère mésoscopique (40\AA autour des îlots de cuivre) et est apparemment causée par des forces élastiques. A un recouvrement $\Theta_{Cu} > 1$, des pics d'absorption de CO adsorbé sur des terrasses plates du Cu et des clusters 3D de Cu sont présents. La largeur et la position des pics caractérisent les différents types de croissance du Cu et montrent en plus la formation d'un alliage CuPd à haute température.

Le système Cu/Pd(100) a été étudié de la même manière. La barrière de diffusion des adatoms est de 0.28eV . A une température inférieure à 450K , on observe une croissance couche par couche presque idéale jusqu'à 5 monocouche environ. Les films de Cu subissent une transition de phase cfc \rightarrow tétragonale, dépendant de la température et de l'épaisseur de la couche. A $\Theta_{Cu} < 1$, le CO occupe des sites localisés entre deux atomes de Pd et au-dessus d'un atome de Cu. Le rapport entre les deux pics correspond à Θ_{Cu} . Au-dessus de 450K , on observe la formation d'un alliage CuPd.

Abstract

By means of a combination of Scanning Tunneling Microscopy and Reflection Absorption Infrared Spectroscopy, structure and chemical reactivity of metallic surfaces were investigated.

The vicinal Pt(997) surface, close to the hexagonal (111) face, exhibits a very regular terrace-step structure with a narrow terrace width distribution around the nominal value of 20.2\AA , if well prepared. When heated in $5 \cdot 10^{-8}$ mbar oxygen at temperatures between 600K and 900K, terrace width and step height doubling occurs. Pt(997) is thermally unstable towards faceting. Above $T_S > 950\text{K}$, the surface undergoes partial phase separation into large (111) facets and regions of the undisturbed structure. The faceting proceeds via a nucleation-and-growth mechanism and appears to be driven by the tendency of the (111) facets to reconstruct.

The adsorption of CO as well as the coadsorption of CO and hydrogen was studied by RAIRS. CO adsorbs preferentially on step edges before populating top- and bridge-sites on the (111) terraces. At higher coverages, a $c(4 \times 2)$ -CO overlayer is formed on the terraces. In the presence of a hydrogen atmosphere at $T_S > 150\text{K}$, the nearly complete removal of adsorbed CO is observed. On the other hand, covering the surface with a full monolayer of hydrogen at $T_S = 165\text{K}$ provides its complete passivation against adsorption from the residual gas, without affecting the terrace-step-configuration. The structure of Pt(997) and the available passivation method demonstrate the ability of the surface to serve as diffractive element in atom beam optics. Additional studies concern the adsorption of N_2O and NO_2 on Pt(997). Both species adsorb molecularly on Pt(997) and form solid multilayers at $T_S < 100\text{K}$.

The growth of thin Cu films on Pd(110) and the CO adsorption properties of this bimetallic system were investigated. The anisotropy of Cu adatom diffusion on this surface (the migration barriers are found to be $E_{D,[1\bar{1}0]} = 0.51\text{eV}$ and $E_{D,[001]} = 0.75\text{eV}$) determines the shape of submonolayer Cu islands. In the case of very low coverages

($\Theta_{Cu} \leq 0.1 \text{ ML}$) and low deposition temperatures ($T_S \leq 300 \text{ K}$) 1D Cu aggregates are formed along $[1\bar{1}0]$. At higher temperatures, migration along $[001]$ is activated and 2D islands start to grow. Depending on T_S , Cu shows 3 different film growth modes: 3D growth at $< 400 \text{ K}$, layer-plus-island-growth at $400 \text{ K} \leq T_S \leq 500 \text{ K}$. Layerwise growth occurs at $500 \text{ K} < T_S \leq 700 \text{ K}$, layers thicker than 5ML are uniaxially compressed along $[1\bar{1}0]$.

On Cu/Pd surfaces with $\Theta_{Cu} < 1$, CO adsorbs at $T_S = 150 \text{ K}$ not only on Pd bridge sites and Cu on-top sites, as would be expected from the results on the pure metal surfaces, but occupies also Pd on-top sites. This change in adsorption site indicates a "chemical" modification of the Pd substrate by the Cu deposit. The modification is of mesoscopic character, penetrating up to 40 \AA onto uncovered Pd terraces and appears to be induced by surface stress effects. In the Cu multilayer range, CO absorption bands on flat Cu layers and 3D Cu clusters are observed. Peak positions and peak widths characterize the different Cu growth modes and reveal high temperature CuPd intermixing.

The system CO/Cu/Pd(100) was investigated in the same way. The migration barrier for Cu adatoms on the Pd substrate is determined to be 0.28 eV . At deposition temperatures between 300 K and 450 K Cu grows in a nearly perfect layer-by-layer mode up to about 5ML. At deposition temperatures below 370 K , Cu forms a pseudomorphic body-centered-tetragonal (bct) bulk phase, at higher temperatures, bct growth sets in at a critical film thickness. In the Cu submonolayer range, CO adsorbs on Pd bridge and CO on-top sites, the ratio of the peak intensities is proportional to the Cu coverage. At temperatures above about 450 K , CuPd intermixing takes place.

Table of contents

1. Introduction: surface structure and surface chemistry	1
2. Experimental methods	5
2.1 Scanning Tunneling Microscopy (STM)	5
2.1.1 General principles	5
2.1.2 The beetle STM	7
2.2 Reflection Absorption Infrared Spectroscopy (RAIRS)	9
2.2.1 General principles of a RAIRS experiment	9
2.2.2 The Fourier Transform Infrared Spectrometer	11
2.2.3 Infrared spectra of adsorbed molecules	14
3. Experimental setup	19
4. STM and RAIRS studies on Pt(997)	23
4.1 Introduction and motivation	23
4.2 The structural phases of Pt(997)	26
4.2.1 The nominal phase	26
4.2.2 Orientational instability of Pt(997)	29
4.3 Complete chemical passivation of Pt(997)	34
4.3.1 CO on clean Pt(997)	35
4.3.2 Hydrogen adsorption on a CO precovered surface	38
4.3.3 CO adsorption on a hydrogen precovered surface	41
4.3.4 Structure of the H/Pt(997) surface and conclusions	41
4.4 Nitrogen dioxide and nitrous oxide on Pt(997)	43
5. Submonolayer and multilayer growth of Cu on Pd(110)	49
5.1 Introduction	49
5.2 The Pd(110) surface	50

5.3 Submonolayer island shapes and Cu adatom diffusion on Pd(110)	52
5.4 The growth of thin Cu films on Pd(110)	64
5.4.1 $T_S \leq 350\text{K}$	64
5.4.2 $350\text{K} < T_S \leq 500\text{K}$	70
5.4.3 $T_S > 500\text{K}$	75
6. CO chemisorption on Cu/Pd(110)	79
6.1 Introduction	79
6.2 RAIRS studies of CO on Cu/Pd(110)	83
6.3 Cu induced CO adsorption site change on Pd(110)	92
6.4 High temperature CuPd intermixing	96
7. Growth and CO adsorption properties of Cu films on Pd(100))	101
7.1 Cu adatom diffusion on Pd(100)	101
7.2 The growth of thin Cu films on Pd(100)	103
7.2.1 Bulk structural properties of bct copper	103
7.2.2 The structure of Cu films on Pd(100)	106
7.2.3 CuPd intermixing at $T_S \geq 500\text{K}$	114
7.3 CO adsorption on Cu/Pd(100)	117
8. Outlook	127
References	129

1. Introduction: surface structure and surface chemistry

In recent years the experimental and theoretical progress in the understanding of structural, dynamic (phonons) and electronic properties of surfaces has been considerable. The relation between surface structure and chemical reactivity, on the other hand, is not well established, despite its technological importance. One reason for this disproportion is the possible assignment of dynamic and electronic properties to surface symmetry and periodicity. The lateral translational invariance of a single crystal surface facilitates the theoretical approach; classical methods of structure analysis like x-ray diffraction, low energy electron diffraction or ion scattering are ideal tools for the investigation of periodic surface structures.

Chemical properties of surfaces, however, can essentially be determined by deviations from the periodic arrangement of atoms. Structural defects like steps, kinks or vacancies can act as active sites for surface reactions and thus play a key role in the understanding of surface chemistry. Two examples: the dehydrocyclization of linear hydrocarbon species on Pt surfaces depends dramatically on the crystal orientation. The highest efficiency was obtained on a regularly stepped (557) surface, whereas on the flat (111) and different high-index surfaces with steps and kinks cracking of the hydrocarbon chains is the dominant process [Gil81]. In the hydrogen-oxygen reaction on Pt(111), on the other hand, the presence of surface steps retards water production by trapping H atoms, hindering them to react further to form H_2O . Other defects, probably kinks, are found to be 10^3 times more reactive than normal terrace sites [Ver92].

A detailed understanding of the elementary processes involved in surface chemistry like adsorption, diffusion, reaction and desorption and their dependance on physical properties of the surface is required in order to pass from simple reactions on model catalysts (like single crystal metal surfaces) to processes of industrial interest and should finally lead to theories with quantitative predictive power.

Microscopy as a local method providing direct, real space images of surface topography is particularly appropriate in this respect. Field ion microscopy, transmission electron microscopy, atomic force microscopy and scanning tunneling microscopy are available techniques permitting atomic-scale surface studies. The latter instrument was used to investigate chemical processes on semiconductor surfaces at the atomic level, for instance the spatial distribution of the reaction of Si(111) with NH_3 [Wol88], determining the reactivity of the different types of atoms in the (7×7) unit cell, however without being able to obtain direct information on the chemical species present on the surface.

But the identification of specific reaction mechanisms and transient intermediates is an important condition which has to be fulfilled in order to describe a catalytic surface process completely. Conventional inelastic electron tunneling spectroscopy is a well-known technique focusing on the identification of molecules introduced onto the oxide barrier of tunnel junctions by analysing the position of jumps in the tunneling conductance dI/dV at the excitation thresholds of characteristic molecular vibrations, with a detection limit of 1/30 monolayer [Wol78]. Scanning tunneling spectroscopy is successfully employed to investigate electronic states on semiconductor surfaces with atomic resolution [Win93]. But it is a more difficult task to obtain useful vibrational spectra of *single* molecules adsorbed on a surface by this technique. The problem of adsorbate diffusion can be alleviated by means of cooling, but it is not yet possible to overcome the sensitivity problem in order to extract unambiguous adsorbate-specific information from the complex current-voltage curves characterising the sample-STM tip electronic interaction [Eig93].

A promising tool for the investigation of surface reactions in real time and real space is the recently developed photoelectron emission microscope [Eng91], by means of which new catalytic phenomena in the oxidation of CO_2 on Pt(110) were discovered. However the spatial resolution of this instrument is currently limited to 100 nm

and its application is restricted to systems with sufficient work function contrast. The lack of methods which would be able to identify the nature of molecular species with nanometer-scale spatial resolution requires the combination of classical spectroscopic techniques like electron energy loss spectroscopy or surface infrared spectroscopy together with microscopic methods in order to elucidate the relation between geometric and electronic surface structure on the one hand and surface chemistry on the other hand.

In this thesis, research work on structural properties of metal crystal surfaces and their influence on the most simple chemical reactions, the adsorption and coadsorption of molecules, is presented. The results were obtained by a combination of scanning tunneling microscopy (STM) and reflection absorption infrared spectroscopy (RAIRS). This particular combination was chosen because of several reasons: infrared spectroscopy requires no instrumentation inside the vacuum chamber, thus the STM can be used without any technical restrictions. The techniques are applicable to both metal and semiconductor surfaces and are able to work under "real pressure" conditions (mbar range).

In chapter 2, both methods are briefly introduced, chapter 3 contains a description of the experimental setup. In chapter 4, STM and RAIRS studies of the vicinal Pt(997) surface are presented. The interest in this particular surface came from its possible use as an optical element for atom beams, specially as a monochromator or analyser in the helium scattering technique employed in our group. A detailed analysis of the surface structure and chemical reactivity were needed in order to ensure a reliable operation of this element.

Chapters 5-7 deal with investigations of the bimetallic catalyst Cu/Pd. These experiments were performed in two steps. In a first step, thin Cu films were deposited on two different single crystal Pd surfaces with (110) and (100) orientation, respectively. Phenomena like submonolayer Cu island formation, Cu adatom diffusion and

the growth mode of Cu films as functions of the deposition temperature were studied. In a second step, the vibrational spectra of CO molecules adsorbed on Cu/Pd surfaces with various compositions were analysed. The influence of Cu island shapes, Cu film morphology, surface stress effects and CuPd alloying on the adsorption properties of adsorbed CO was revealed.

2. Experimental methods

2.1 Scanning Tunneling Microscopy

2.1.1 General principles

As the name implies, this instrument is based on two principles. *Scanning* devices like the stylus transducer [She88] are popular instruments to measure surface topographies. A stylus is drawn over the more or less rough surface of a sample. The vertical displacements of the stylus are amplified and a framed scanned section of the surface is obtained. This method requires mechanical contact between sample and stylus tip, the finite tip radius is determining the resolution of the instrument (typically some μm). *Tunneling* of electrons through an insulator, on the other hand, is a physical effect of great technologic importance known since 1928 [Fow28].

The idea of Binnig and Rohrer [Bin82] was to scan surfaces without bringing sample and tip into direct mechanical contact by using the tunneling current through the vacuum gap to measure the sample-tip distance. The current between tip and sample can be estimated by calculating the tunneling current between two flat, parallel electrodes [Som33]:

$$I_T \sim \frac{V_T}{s} \exp(-A\sqrt{\phi} s) \quad (2.1)$$

where $A \approx 1.025(\text{eV})^{-1/2} \text{\AA}^{-1}$, ϕ the average workfunction, V_T the applied tunnel voltage and s the distance between the plates. Although this is a coarse approximation for the electrical interactions between sample and tip in a STM, the exponential dependence of the tunneling current on the sample-tip distance is described correctly. I_T changes by an order of magnitude for every \AA change of s , if typical values for the work functions of the two metal electrodes (4eV) are assumed. Fig.2.1 shows the principle of operation of the scanning tunneling microscope [Bin82]. The tip is mounted onto a rectangular piezodrive P_x, P_y, P_z . P_x and P_y scan the tip in a plane parallel to the surface. The control unit CU applies a voltage V_z to the piezo P_z

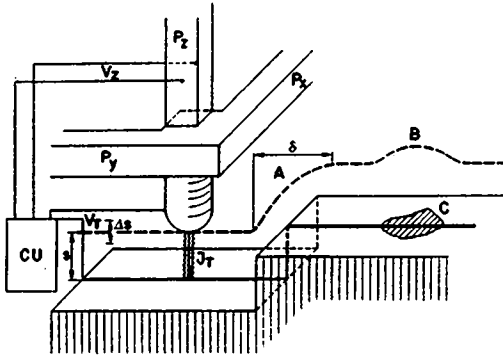


Fig.2.1: Principle of the Scanning Tunneling Microscope after Binnig and Rohrer (from [Bin82]).

such that the current I_T remains constant during scanning. When the work function ϕ is constant, the tip moves at a constant distance s over the sample, for instance over a surface step A. Thus the z -movement of the tip reflects the topography of the surface. This is however only the case for a electronically homogeneous surface, e.g. a clean single crystal metal surface. For adsorbed atoms or molecules, this straightforward interpretation no more holds. Thus when the work function changes (zone C), corresponding changes in s occur according to eq.(2.1).

STM theories try to determine the tunneling current I_T as a function of the tip position \vec{r}_o and the tunneling bias V_T . The first quantitative STM theory by Tersoff and Hamann [Ter83] calculated I_T by means of first-order perturbation theory:

$$I_T = \frac{2\pi e}{\hbar} \sum_{\mu,\nu} f(E_\mu)(1 - f(E_\nu + eV_T)) |M_{\mu,\nu}|^2 \delta(E_\mu - E_\nu) \quad (2.2)$$

where $f(E)$ is the Fermi function, $M_{\mu,\nu}$ is the tunneling matrix element between states ψ_μ of the tip and ψ_ν of the surface and E_μ the energy of the unperturbed state ψ_μ . The microscopic structure of the tip is poorly known and in the initial theory it was considered to be of minor importance. Therefore it has been approximated as locally spherical with radius of curvature R where it approaches nearest the sample. The matrix element was evaluated only for s -wave functions of the tip. In the case of low temperature and small V_T , one obtains $I_T \sim \exp(2kR)V_T\rho(\vec{r}_o, E_F)$, where

$k = \hbar^{-1} \sqrt{2m\phi}$ (m : electron mass) and ϕ is the work function assumed to be equal for sample and tip.

$$\rho(\vec{r}_o, E_F) = \sum_{\nu} |\psi_{\nu}(\vec{r}_o)|^2 \delta(E_{\nu} - E_F) \quad (2.3)$$

is the local density of states at E_F (Fermi level of the sample) at the position \vec{r}_o of the tip. Since $|\psi_{\nu}(\vec{r}_o)|^2 \sim \exp(2k(R+d))$ (d : sample-tip distance), one obtains $I_T \sim \exp(-2kd)$ like in equation (2.1).

The important result of Tersoff and Hamann is that the STM image represents a contour map of constant surface local density of states (LDOS) at the Fermi level. However, STM experiments achieving atomic resolution show frequently corrugations much larger than the LDOS corrugation [Win89]. More elaborated theories were thus required, taking into account the detailed electronic tip state. Chen [Che91] established a microscopic theory in terms of a localized surface state on the tip and a two-dimensional array of independent localized states on the sample and showed that with p- and d-states on the tip, corrugation amplitudes of STM images can be orders of magnitude greater than the Fermi-level LDOS. Other authors proposed elastic deformations of the tip due to adhesive sample-tip interactions in order to explain atomic resolution STM imaging of close-packed metal surfaces [Win89].

2.1.2 The beetle STM

The so-called beetle STM [Bes86] (fig.2.2) consists of a microscope disc (aluminium) which holds four piezoceramic tubes. Each tube is provided with several metal electrodes on the inner wall and on the outside to which the electrical connections are made by thin wires. The inner tube holds the STM tip, the outer tubes are provided with small metal spheres and act as positioners. The three support pins are attached radially to the support disk and serve to carry the microscope by means of the z-manipulator. The STM can be lowered down onto the sample holder and

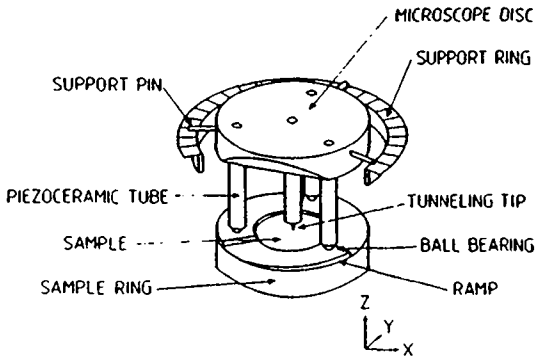


Fig.2.2: Sketch of the Besocke STM (from [Fro89]).

subsequently mechanically decoupled. The sampler holder consists mainly of a molybdenum ring with three ramps cut into it, each 0.4mm high and spanning an arc of 120° [Fro89]. The coarse tip approach is achieved by a collective motion of the outer piezo tubes rotating the microscope clockwise. The microscope is screwing itself down the ramps and thus moves the tip towards the sample. When the tip comes within tunneling distance to the surface, the tip approach is automatically stopped. Sample scans can now be performed by the inner piezo tube.

In order to investigate different regions of the sample, the inner piezo tube can be moved relative to the sample by bending the three outer tubes. By applying asymmetric voltage ramps to the outer piezos, the STM can move over macroscopic distances (some mm). The different moving modes of the STM (linear motion or rotation) are achieved by applying either the same signals to the outer piezo tubes (linear motion) or individual signals to each contact of the piezos which results in a tangential bending of the positioners relative to the microscope disc and thus a rotation of the microscope. The electrical signals bend the piezo tubes slowly to one side and then quickly to the opposite side, so that the microscope disc can not follow this action due to its inertia. This results in a sliding of the metal spheres over the surface of a ramp and a movement of the STM.

The advantages of this microscope design are the following:

- * The microscope is temperature compensated to first order since the thermal

expansion of all four piezo tubes is equal, leaving the tip to sample distance unchanged upon temperature variations. This facilitates temperature-dependent measurements with fast temperature equilibration and slow drift.

- * The design is simple and compact. The STM has no mechanical contact to the environment because the tip approach does not require mechanical connections in UHV.

- * The sample can be attached to the sample manipulator during STM experiments, allowing its full temperature control and preventing at the same time complicated sample transfer mechanisms.

2.2 Reflection Absorption Infrared Spectroscopy (RAIRS)

2.2.1 General principles of a RAIRS experiment

The study of molecular vibrations by infrared spectroscopy has contributed an important part to our knowledge about the bonding and symmetry of molecules in the gaseous, liquid and solid phase [Her45]. Thus it appeared only natural to extend infrared spectroscopy to provide a useful technique for the study of molecules in the adsorbed phase. The main difficulty which arises from such an approach is the low concentration of molecules with which infrared radiation can interact. A monolayer adsorbed on a single crystal surface (1cm^2) provides about 10^{14} absorbers, orders of magnitude less than in a typical bulk sample (10^{19}). Vibrations of molecules adsorbed on metal surfaces have to be investigated by a reflection method, since the metal is nontransparent to infrared radiation. A first attempt to overcome the sensitivity problem was to reflect the infrared beam several times (up to 35 reflections) from the surface under study by a special geometric arrangement [Pic 59]. However in 1966, Greenler showed by a comparatively simple, classical electrodynamic model that under certain conditions a single reflection is sufficient to obtain useful spectra. Thus Greenler provided the basic foundations for today's RAIRS-experiments [Gre66].

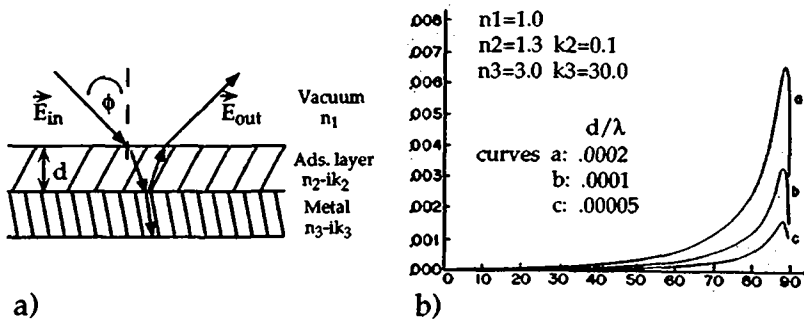


Fig.2.3: a) Three-layer-model of Greenler. ϕ denotes the IR light incident angle, $n_j - ik_j$ is the optical constant of the layer j .
b) Absorption factor A as a function of angle of incidence for light polarized perpendicular to the surface with three different values of d/λ (from [Gre66]).

The main results of this analysis can be estimated from the amplitude and phase changes of infrared light upon reflection from a metal surface [Hay85,1], which are provided by the classical Fresnel formula [Hec74]. The light component polarized parallel to the metal surface undergoes a phase shift of 180° upon reflection, whereas its amplitude remains nearly unchanged. The resulting electric field at the surface thus vanishes and no interaction of the infrared light with molecular vibrations having their dynamic dipole moment parallel to the surface is possible (the so-called "surface selection rule").

Greenler [Gre66] introduced a three-layer-model (vacuum/adsorbed layer/metal) (fig.2.3a), for which he solved the wave equations and calculated an absorption factor $A = (R^0 - R)/R^0$, where R^0 is the reflectance of the system with a nonabsorbing adsorbate and R is the reflectance of the complete system. Fig.2.3b shows the calculated absorption factor for the light component polarized perpendicular to the surface as a function of the incident angle ϕ and d/λ , where d is the thickness of the adsorbed layer and λ the infrared light wavelength. The absorption factor A shows a

sharp maximum for large values of ϕ . The results of the three-layer-model for metals can be summarized as follows:

- 1.) Only molecular vibrations with a finite component of their dynamic dipole moment perpendicular to the surface are dipole-active.
- 2.) The RAIRS-experiment is most effective near grazing incidence angles.
- 3.) The absorption is largest for highly reflecting metals and for adsorbates with high absorption coefficient k .

Until recently it was believed that vibrational modes which are not dipole-active are not observable in surface infrared spectroscopy. New instrumental developments allowed the extension of RAIRS measurements to lower frequencies, and dipole-forbidden frustrated translations (for H on W(100) on Mo(100) [Cha85]) and rotations (for CO on Cu(100) and Cu(111) [Hir90]) were detected. Here the interaction with the infrared light is indirect: while the infrared activity of the former was explained by coupling to substrate phonons, the latter are observed due to their coupling to allowed electronic absorptions of the metal substrate [Per92]. They appear as "positive", anti-absorption peaks, since no adsorbate-induced energy absorption occurs if the molecular vibration and the collective motion of the metal electron gas are resonant.

2.2.2. The Fourier Transform Infrared Spectrometer

The FTIR spectrometer (fig.2.4) is based on the design of the classical two-beam interferometer by Michelson [Mic91,1]. It consists of two mutually perpendicular mirrors, one of which can move along an axis that is perpendicular to its plane. The radiation from the infrared light source is split by a beamsplitter, partially reflected to the fixed mirror and partially transmitted to the moving mirror. Back at the beamsplitter, the two beams recombine. Because of the effect of interference, the intensity of the light passing to the detector depends on the difference in the optical

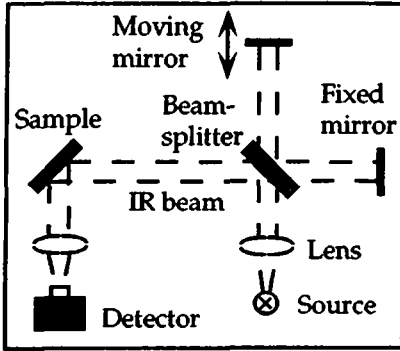


Fig.2.4: Sketch of the
Michelson interferometer

path of the beams in the two arms of the interferometer and the light wavelength.

Generally, so-called Globars consisting of a silicon rod resistively heated are used as light sources. For each wavelength in the continuous spectrum of these thermal emitters, the interference conditions are different. Thus the detector measures at any position the sum of the interfered intensities corresponding to each wavelength. This sum, the so-called interferogram $I(x)$, (x : position of the moving mirror) contains the total spectral information in a Fourier transform spectrometer. By performing the Fourier transformation of the position-dependent interferogram $I(x)$ the spectrum $I(\tilde{\nu})$ ($\tilde{\nu} = 1/\lambda$: wavenumbers in cm^{-1}) can be calculated:

$$I(\tilde{\nu}) = \int_{-\infty}^{+\infty} I(x) \exp(-2\pi i x \tilde{\nu}) dx \quad (2.4)$$

Equation (2.4) shows that in theory, such a spectrum could be measured with infinitely high resolution if the moving mirror could travel an infinitely large distance. In practice, this distance is limited to a few centimeters. To a first approximation, two wavenumbers separated by $\Delta\tilde{\nu}$ are only resolved if the optical path difference is increased to the point $(\Delta\tilde{\nu})^{-1}$ where the two waves are in phase for the first time

after zero path difference. Thus, the resolution $\tilde{\nu}_{res}$ of the spectrometer is given by

$$\tilde{\nu}_{res} = \frac{1}{2\Delta_{max}} \quad (2.5)$$

where Δ_{max} is the maximum mirror travel distance. For the MATTSON Galaxy 6020 spectrometer used in our experiments the maximum resolution is 0.125cm^{-1} , corresponding to a mirror travel distance of 4 cm.

The finite mirror travel corresponds mathematically to the multiplication of the infinite interferogram (between $x = -\infty$ and $+\infty$) by a boxcar function, which is unity between $-\Delta_{max}$ and $+\Delta_{max}$ and zero at all other points. It is well known that the Fourier transform of the product of two functions is the convolution of the Fourier transforms of each function. Thus a real spectrum is the convolution of the ideal spectrum with the Fourier transform of the boxcar function, which is a sinc-function $\text{sinc}(x)=\sin(x)/x$. The oscillations of the sinc-function affect the shape of narrow peaks and may distort peak intensities. A way to overcome this problem is to weight the interferogram with a so-called apodization function which decreases smoothly with increasing $|x|$ value [Gri86]. This reduces the oscillations and smoothes the spectra. However it also reduces the effective instrumental resolution. The RAIR spectra of this work have been weighted by a triangular apodization function.

A computational problem arises from the fact that an interferogram is not sampled at infinitesimally small increments of the mirror position x , as (2.4) would suggest. In fact, the sampling frequency is limited by computer storage capacity and digitalization time. A simple linear interpolation between each measured point would result in a stepping of the spectrum. A far smoother spectrum can be obtained by "zero-filling" of the interferogram [Gri75], that means by adding a certain number of zeros to the data array before Fourier transforming (in general at least 8 times more than the number of discrete measured points the interferogram contains). Triangular apodization and zero-filling are the only routinely performed numerical modifications

of the measured spectra in this work. If other data manipulations were necessary, this is noted in each case.

2.2.3 Infrared spectra of chemisorbed molecules

In the following, a brief general treatment of the vibrational spectra of molecules chemisorbed on metal surfaces is presented. Characteristic features like vibrational frequencies and frequency-shifts, line shapes and intensities will be discussed. The vibrational behaviour of adsorbed CO is chosen as an example since most of the RAIRS experiments in this work deal with this molecule, which is the by far best studied chemisorbed species on metals.

An N-atom species has $3N$ degrees of kinetic freedom. Three of these are translations, three are rotations (two for a linear species) and $3N-6$ are vibrations ($3N-5$, respectively). When the molecule becomes adsorbed on a solid, all degrees of freedom are converted to vibrations. Of the 6 vibrational modes of adsorbed CO, only the internal C-O stretching mode ν_1 has a frequency above 500cm^{-1} and thus lies within the range accessible to conventional IR detectors used in the present studies. In general, the gas phase vibrational frequency of $\nu_1=2143\text{cm}^{-1}$ is shifted to lower frequencies when CO adsorbs on a metal surface. This is due to the interaction with the image dipole and, more importantly, due to the chemical bonding. The latter effect allows the use of vibrational frequencies as fingerprints to indentify the adsorption site. The downward shift can be understood when considering the details of the adsorbate-metal bonding. CO has the electron configuration $(1\sigma)^2(2\sigma)^2(3\sigma)^2(4\sigma)^2(1\pi)^4(5\sigma)^2$ [Her45]. The CO-metal bond is formed by electron transfer from the 5σ -orbital to the metal with electron "backdonation" of the metal d-electrons into the unoccupied $2\pi^*$ -orbital of the molecule [Bly64]. With respect to the internal C-O bond, the 5σ -orbital is weakly bonding and the $2\pi^*$ -orbital is strongly antibonding. Thus the C-O bond is weakened upon adsorption and the corresponding vibrational frequency

is lower than that in the gas phase. It is believed that the higher the coordination of the molecule, the larger is the amount of backdonation. In general, the following empirical relation holds [Ngu78]:

Linear (on top) CO	2130-2000 cm ⁻¹
Twofold bridged CO	2000-1880 cm ⁻¹
Threefold bridged CO	1880-1800 cm ⁻¹
Fourfold bridged CO	<1800 cm ⁻¹

This statement must however be considered with some caution, especially in the case of coadsorption of CO together with other molecules. For instance, top-site CO in coadsorption with alkali-metal atoms exhibits vibrational frequencies down to 1300 cm⁻¹ [Wes86].

With increasing coverage, the vibrational frequency of adsorbed molecules undergoes a shift, usually to higher frequencies. Two effects contribute to this frequency shift. The first is vibrational coupling between adsorbed molecules that results from electrostatic dipole interactions and is called *dipole* shift or *dynamic* shift. The second, the *chemical* or *static* shift is a result of the redistribution of electronic charge when the coverage is increased. Both contributions can be separated experimentally in RAIRS [Woo82] by performing isotopic mixture experiments. For instance, an isolated ¹³C¹⁶O surrounded entirely by ¹²C¹⁶O molecules experiences no dynamic shift due to its neighbours, simply because their vibrational frequencies are different enough. However the ¹³C¹⁶O is in a chemical sense indistinguishable from its neighbours and undergoes the same static shift as a ¹²C¹⁶O. Such isotope mixture measurements reveal that the dynamic shift is always positive and amounts to 25-50 cm⁻¹ [Hay85,1]. The static shift, however, can be positive or negative, depending on the substrate. Typical values are -27 cm⁻¹ to -60 cm⁻¹ for CO on Cu [Woo82] and +60 cm⁻¹ for CO on Pd (see e.g. chapters 6 and 7).

The dependence of the chemical shift on the substrate was first explained by

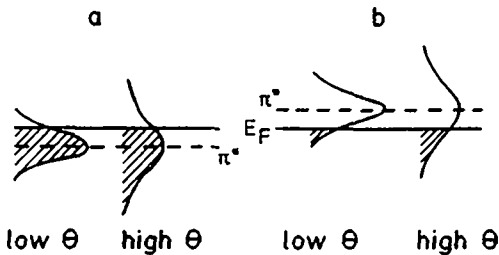


Fig.2.5: Diagram showing the variation in occupation of a broadened $2\pi^*_b$ state for the cases in which the state lies (a) below and (b) above the Fermi level of the metal (from [Woo82]).

Woodruff et al. [Woo82]. Their argument is based on the fact that the amount of $2\pi^*$ -backdonation depends on the relative energies of the metal Fermi level and the CO $2\pi^*$ -antibonding orbital. Due to the interaction with the metal, this state splits up into a $2\pi^*_a$ -state and a $2\pi^*_b$ -state [Mes82]. The former is antibonding with respect to the CO-metal bond and lies well above the Fermi level, whereas the latter is a bonding state. If $2\pi^*$ -backbonding is strong (like for transition metals), the $2\pi^*_b$ -state lies slightly below E_F , in the case of weak backbonding (on noble metals) it lies above E_F (fig.2.5). When the CO coverage increases, the $2\pi^*_b$ -level broadens as a result of increasing overlap of the bands. This broadening leads to a change in its occupation number. If the center of the band is located below E_F , the band becomes more depleted, if its position is above E_F , it becomes increasingly occupied. Keeping in mind that the $2\pi^*$ -level is antibonding with respect to the C-O bond, the C-O stretching frequency undergoes an upward shift in the first and a downshift in the second case.

Compared to this more qualitative interpretation of the chemical shift, the coverage dependent dynamic shift can be calculated accurately by means of classical electrodynamics [Per81, Mah78]. We consider a complete monolayer of identical

molecules at positions \vec{x}_i . The dipole moment \vec{p}_i induced by an external field \vec{E}_i can be written as

$$\vec{p}_i = \alpha_A \vec{E}_{local} = \alpha_A (\vec{E}_i - \sum_{i \neq j} U_{ij} \vec{p}_j), \quad (2.6)$$

The local electric field \vec{E}_{local} is a sum of the applied field \vec{E}_i and the field from the other dipoles \vec{p}_j and their image dipoles [Jac62]:

$$\sum_{i \neq j} U_{ij} \vec{p}_j = \sum_{i \neq j} \frac{\vec{p}_j - 3\vec{n}(\vec{n}\vec{p}_j)}{|\vec{x}_i - \vec{x}_j|^3} \quad (2.7)$$

where \vec{n} is the unit vector in the direction $(\vec{x}_i - \vec{x}_j)$. α_A is the microscopic polarizability of one single adsorbed molecule

$$\alpha_A = \alpha_e + \frac{\alpha_v}{1 - (\omega/\omega_A)(\omega/\omega_A + i\gamma)} \quad (2.8)$$

where α_e and α_v are the electronic and vibrational polarizabilities, ω_A is the singleton frequency of isolated molecules, ω the frequency of the external field and γ the damping. The translational invariance of the problem allows to solve equation (2.6) by Fourier transformation:

$$\vec{p}_i = \sum_q \vec{p}_q e^{i(\vec{q}\vec{x}_i - \omega t)} \quad \vec{E}_i = \sum_q \vec{E}_q e^{i(\vec{q}\vec{x}_i - \omega t)} \quad (2.9)$$

Infrared light with wavelengths much larger than the adsorbate unit cell will only excite $\vec{q} = 0$ modes (modes without momentum transfer). If the damping γ is infinitesimally small, the following relation between the singleton frequency ω_A and the vibrational frequency Ω shifted by the dipole-dipole-interaction can be deduced, assuming that \vec{p}_i and \vec{E}_i are oriented perpendicular to the surface:

$$\left(\frac{\Omega}{\omega_A} \right)^2 = 1 + \frac{\alpha_v \tilde{U}(0)}{1 + \alpha_e \tilde{U}(0)} \quad (2.10)$$

In the case of partial coverage $\theta < 1$ the formula has to be modified as follows:

$$\left(\frac{\Omega}{\omega_A} \right)^2 = 1 + \frac{\theta \alpha_v \tilde{U}(0)}{1 + \theta \alpha_e \tilde{U}(0)} \quad (2.11)$$

The dipole interaction between adsorbed molecules causes a deviation from a linear dependance between coverage and absorption intensity. The above cited theory [Per81, Mah78] provides a formula which shows how the integrated absorbance depends on the dielectric screening due to the electric polarizability of neighbouring molecules:

$$\int A d\omega \sim \frac{\theta \alpha_v \tilde{U}(0)}{(1 + \theta \alpha_e \tilde{U}(0))^2} \quad (2.12)$$

The main difficulty in using (2.11) and (2.12) is the poorly known dependence of the polarizabilities on the physical and chemical environment. However, in some cases, particularly at low coverages, the assumption of a similar linear increase in integrated intensity with coverage is sufficient to determine thermodynamic quantities or to compare absorption cross sections of various adsorbed species [Hay85,1].

While the vibrational linewidths of molecules in the gas phase or of physisorbed layers on insulators [Hei90] are typically smaller than 0.1 cm^{-1} , the internal vibrational modes of molecules chemisorbed on metal surfaces exhibit half-widths in the range between 5 cm^{-1} and 100 cm^{-1} (full width at half maximum FWHM). Both homogeneous and inhomogeneous broadening contribute to the observed linewidths. One factor in the homogeneous line broadening is the finite lifetime of the vibrationally excited state [Gad84]. Coupling of the adsorbate mode to the atomic displacement field of the crystal lattice (phonons) or to the density fluctuation field of the substrate electron gas (electron-hole pair creation) are the mechanisms allowing dissipative amplitude decay. Also pure dephasing without net energy transfer gives rise to homogeneous line broadening. Nonequivalent vibrational frequencies of adsorbed molecules result in inhomogeneous line broadening. This is either due to a lack of order in the adsorbed overlayer or to the occupation of nonequivalent adsorption sites. Especially at low coverages, where molecules are adsorbed into a lattice gas or in small islands broad, often asymmetric vibrational peaks are observed (see also chapter 6.1).

3. Experimental setup

All experiments were carried out in a stainless steel UHV system (base pressure $1 \cdot 10^{-10}$ mbar). It consists of two chambers, in the following called "preparation chamber" and "STM/IR chamber". The complete vacuum system is shown in fig.3.1. Fig.3.2 displays a schematic 3D view of the apparatus. The preparation chamber is equipped with the usual techniques for sample preparation and control, i.e. an ion gun (fixed ion energy 800eV), an Auger electron spectrometer with cylindrical mirror analyser and a reverse view LEED. The STM/IR-chamber contains the scanning tunneling microscope described in chapter 2.1.2 and in detail in Ref. [Röd91], a quadrupole mass analyser and a Knudsen cell, which is used for the evaporation of copper. The vacuum system of both chambers can be decoupled by a gate valve in order to perform STM- or RAIRS-experiments under "real" pressure conditions (mbar range). A second gate valve disconnects the vacuum system from the 340l/s turbomolecular pump which is turned off in order to avoid vibrational perturbations when STM-measurements are made. The whole apparatus is attached by springs to the ceiling of the laboratory, the springs being the only mechanical contact of the vacuum chamber to the "environment" during tunneling.

The FTIR spectrometer and the infrared optics are situated in two dry-air purged Perspex chambers (fig.3.3). These chambers are linked to the "STM/IR-chamber" by self-made KBr windows [Dam87]. The infrared beam taken from the spectrometer passes through a polariser ("wire-grid" type with 1200 lines/cm) and is focused by a KBr lens through one of the windows onto the sample at an angle of incidence of $85 \pm 1^\circ$. The reflected IR-light leaves the UHV-chamber through a second window and is finally focused by a parabolic mirror onto either a liquid-nitrogen cooled mercury-cadmium-telluride detector or an indium antimonide detector depending on the wavelength range under study.

A long travel manipulator (600mm travel range) translates the sample along the

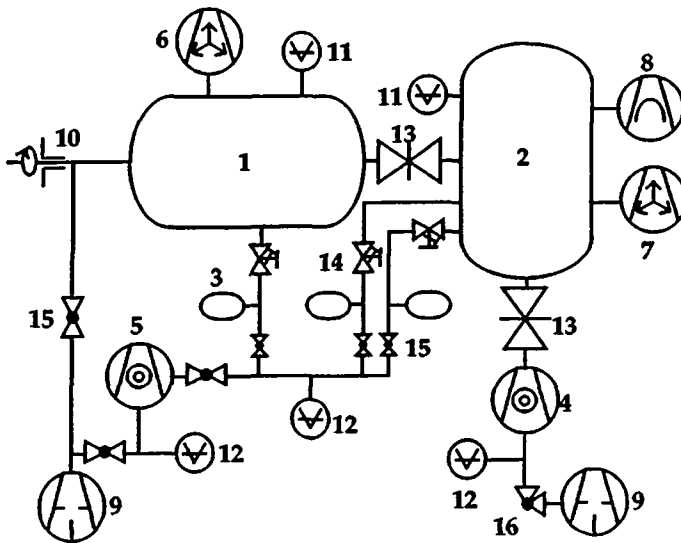


Fig.3.1: Sketch of the vacuum system:

- | | |
|--------------------------------|---|
| 1 STM/IR chamber | 9 Rotary vane pump |
| 2 Preparation chamber | 10 Differentially pumped rotary feedthrough |
| 3 Gas inlet system | 11 Ionisation gauge head |
| 4 Turbomolecular pump (340l/s) | 12 Pirani gauge head |
| 5 Turbomolecular pump (50l/s) | 13 Bellows-sealed gate valve |
| 6 Ion pump (60l/s) | 14 Leak valve |
| 7 Ion pump (230l/s) | 15 Seal valve |
| 8 Titanium sublimation pump | 16 Seal valve |

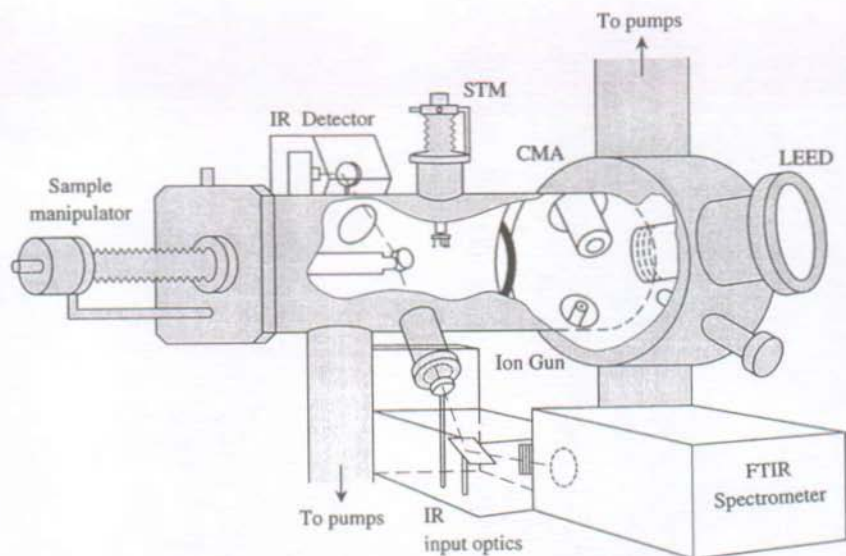


Fig.3.2: Schematic view of the UHV apparatus: on the right hand side the sample preparation chamber, on the left hand side the STM/IR chamber.

main axis of the UHV system, the sample can be rotated around this axis. The sample holder, provided with the STM ring, is directly mounted to a liquid helium cryostat, which allows the sample to be cooled down to 20K, by electron bombardment it can be heated up to 1400K. The temperature range for tunneling experiments, however, is limited by vibrations due to the liquid helium flow and the piezo tube depolarisation temperature and is thus restricted to the range 150-550K.

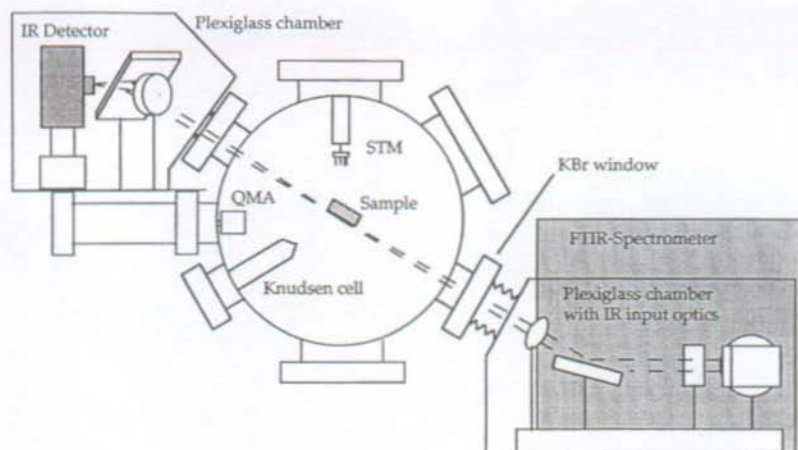


Fig.3.3: Sectional view of the STM/IR chamber showing the infrared beam path.

4. STM and RAIRS studies on Pt(997)

4.1 Introduction and motivation

The interest in a scanning tunneling microscopy and infrared spectroscopy study on the vicinal Pt(997) surface arose initially from the search for technical improvements of the helium scattering method. Thermal Energy Atom Scattering (TEAS), which provides information on surface structure, surface phonons and crystal growth, has become a powerful tool during the past 15 years due to the development of monochromatic He beam sources ($\Delta E/E = 0.02$) and high performance time of flight (TOF) techniques for energy resolved measurements [Hul92]. Nevertheless a substantial increase in energy resolution and/or transfer width is still necessary in order to approach new physical problems. This requires further monochromatisation of the helium beam as well as an improvement of the energy analysis which can hardly be provided by the TOF technique for technical reasons and beam intensity problems [Hah90]. Therefore, it was recently proposed [Kuh92,1] to use surface diffraction as dispersive device in a Helium Triple Axis Spectrometer. An analogous experiment was first realized by Estermann, Frisch and Stern [Est31] using LiF crystals. This classical experiment demonstrated the reality of deBroglie waves associated with material particles.

Fig.4.1a (next chapter) schematically shows the vicinal Pt(997) surface, which is obtained by cutting a Pt crystal with an angle $\alpha = 6.45^\circ$ with respect to the close-packed (111) plane. Nominally, the surface consists of (111) terraces 20.2\AA in width separated by monatomic steps 2.27\AA in height. It is ideally suited as a dispersive element for He waves: its regular arrangement provides a stepped reflection grating in analogy to the so-called Echelette-grating in classical optics. The close-packed (111) terraces act as mirrors for the thermal energy helium atoms and more than 70% of the incoming intensity is reflected in the specular direction at $T_s=150\text{K}$ [Bor89]. If the scattering geometry is chosen suitably (the necessary condition is the coincidence

of the specular direction of the terraces and a diffracted order of the macroscopic (997) plane), the reflected beam intensity can be concentrated in one single high-order diffraction peak [Com79]. Intensity losses are thus minimized when Pt(997) is employed as a monochromator for the incoming He beam or as an analyser for the energy distribution of the atoms scattered by the sample surface. In principle, its energy resolution is only limited by the finite divergence of the helium beam which smears out the dispersive wavelength separation of the Echelette.

However, two requirements must be fulfilled for the vicinal platinum surface to serve as a dispersive device in atom optics:

i.) If the "real" Pt(997) surface showed deviations from the strictly periodic terrace-step structure, a broadening of the diffraction peaks of the He atoms scattered in a slightly nonspecular direction would occur. This would of course affect the performance of the surface as monochromator or analyser [Kuh92,1]. In chapter 4.2.1, STM studies are presented, which were performed in order to ensure if Pt(997) exhibits no severe structural irregularities.

ii.) The adsorption of residual gas molecules reduces the He reflectivity of the terraces due to diffuse scattering. In order to ensure a maintenance-free operation for several hours or even days it is therefore necessary that the surface can be made inert to the ambient residual atmosphere (10^{-10} mbar). By combined STM/RAIRS studies a method for the complete long-term passivation of Pt(997) was developed (chapter 4.3) [Hah93].

Besides the mentioned direct motivation for the present study of Pt(997), vicinal surfaces are of general interest. From a technological point of view surface steps play a central role in many surface chemical and physical problems, including catalysis and epitaxial growth (see also chapters 5-8). On the other hand, on the fundamental level they constitute model systems to study the relation between surface structure and surface energy. If α is the misorientation angle, the total energy of the vicinal

surface (per unit area) is given by [Jay83]:

$$\gamma(\alpha, T) = \gamma_o(T) + \frac{\beta(T)}{h} |\tan \alpha| + \frac{B(T)}{a_{\parallel} h^3} |\tan \alpha|^3 \quad (4.1)$$

The first term γ_o is the surface energy of the low index plane (per unit area) while $\beta(T)$ is the energy per unit length to form a step of height h . The thermal dependence of β comes from the possibility of exciting kinks at the step edges. The third term $B(T)$ accounts for interactions between neighbouring steps, a_{\parallel} being the unit vector along the step edge.

Of the vicinal metal surfaces studied up to now by STM only a few are more or less strictly periodic, thus showing their nominal structure, namely Ni(771) [Haa91], Cu(117) [Poe90] and Cu(1,1,11) [Rou92]. For these surfaces, the step-step interaction energy $B(T)$ is repulsive and stabilizes the ordered superlattice of equally spaced monatomic steps. Due to the delicate balance between step and terrace energies, stable vicinal surfaces can undergo morphological changes as a function of temperature and/or impurity concentration. At elevated temperatures thermal disorder through kink excitation competes with the order established by the repulsive step-step interaction. The Au(332) and Au(755) surfaces are indeed found to be kink-rich with extremely varying terrace widths even at 300K [Adz92]. The step formation energy can eventually disappear at high temperatures according to $\beta(T) \sim \exp(-c/\sqrt{T_R - T})$, resulting in a roughening transition of the low index facet at T_R [Swe78]. The thermal dependence of $\gamma(T)$ might also induce reconstructions or thermal faceting. Vicinal Si surfaces close to (111) are observed to be instable towards faceting driven by the $(7 \times 7) \rightarrow (1 \times 1)$ reconstruction of the (111) [Wil91] terraces whereas vicinal Pb surfaces close to (111) undergo faceting driven by surface melting [Pin93]. On a stepped Pt(100) surface, coexistence of step-free, quasi-hexagonally reconstructed domains and unreconstructed, stepped domains was observed in a temperature range between 1620K and 1820K [Wat93].

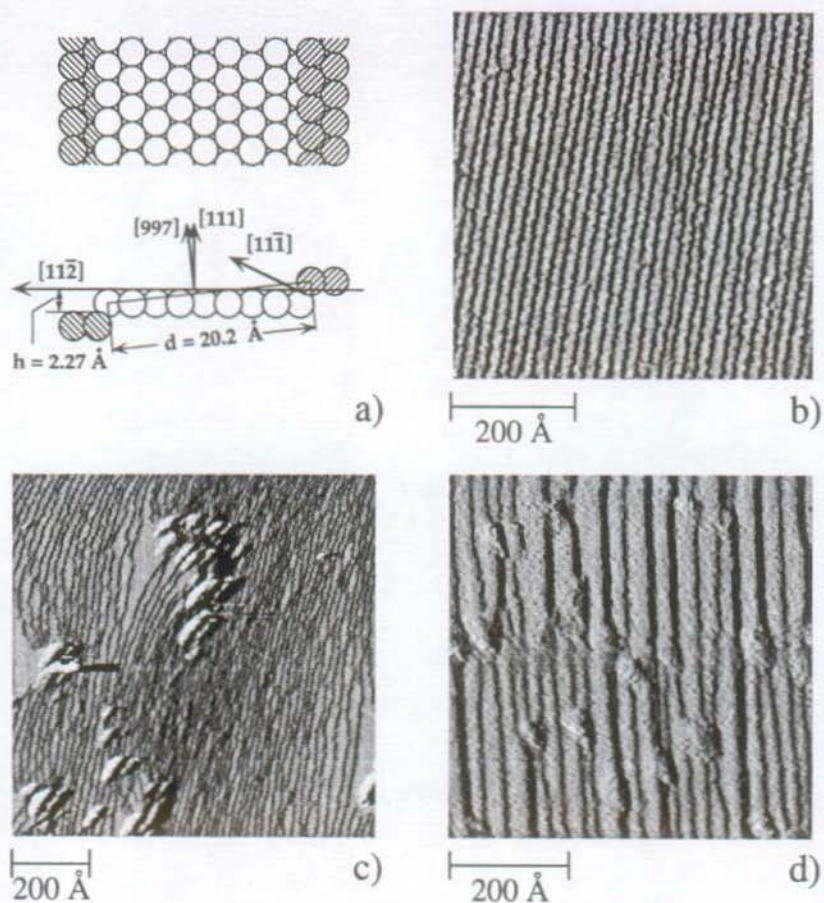
In chapter 4.2.2 temperature and impurity induced changes in the surface morphology of the vicinal Pt(997) surface are reported. Upon oxygen adsorption at temperatures between about 600K and 900K step doubling occurs while flashing the crystal to temperatures above 950K leads to partial faceting of the surface. In a final chapter 4.4 I will summarize briefly RAIRS studies on the adsorption of NO₂ and N₂O on Pt(997).

4.2 The structural phases of Pt(997)

4.2.1 The nominal phase

The crystal was oriented, cut by spark erosion and polished to the desired orientation to within 0.1°. It was cleaned by repeated cycles of argon ion bombardment (ion energy 800eV) at 800K and subsequent annealing at 900K for several minutes. This procedure resulted in a sharp LEED pattern with hexagonal symmetry and an energy dependent splitting of the spots, as expected for a vicinal surface close to fcc(111). Fig.4.1b displays a 600Å×600Å STM image of Pt(997). After careful preparation as described above, the surface shows a terrace-step arrangement close to its nominal structure, with terrace widths varying moderately around their nominal width of 20.2Å. Measurements of the step heights revealed that only monatomic steps occur. However the surface turned out to be highly reactive and a successful preparation depended crucially on parameters like the background pressure during annealing. In the presence of impurities, typically clusters supposed to be residual carbon, the steps are pinned during the annealing procedure and the local terrace-step order is lost (fig.4.1c).

Fig.4.1: (next page) a) Schematic top- and side view of the stepped Pt(997) surface
b) 600Å×600Å STM image of the clean, well-prepared Pt(997) surface. All images in figs.4.1 and 4.3 were recorded in the differential mode, which means that the



derivatives of the lines of constant current were recorded. The dark lines represent therefore downward steps.

c) Pt(997) with ca. 5% residual carbon (image size $860 \text{ \AA} \times 860 \text{ \AA}$)

d) $600 \text{ \AA} \times 600 \text{ \AA}$ STM image of the oxygen-reconstructed Pt(997) surface, showing terrace width and step height doubling

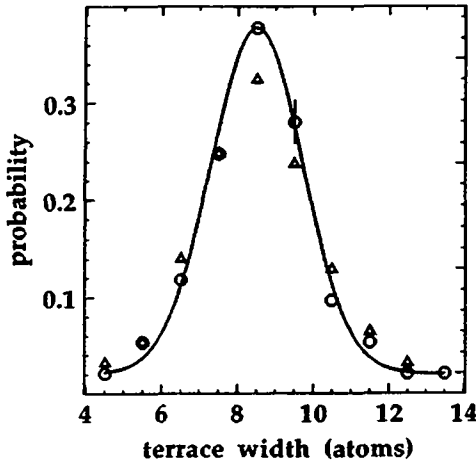


Fig.4.2: Terrace width distribution of Pt(997) in units of atoms. In the histogram the data within ± 0.5 atom about the possible lattice distance of 7,8,9 atoms etc. are assembled. Circles: well prepared surface. Triangles: after flash to 900K and rapid cooling (50K/s) to room temperature. Line: Best fit to the WB model.

In view of a more quantitative characterization of the clean, well ordered Pt(997) surface, the distribution for the distances between neighbouring steps by analysing about 1000 individual line scans from 12 STM images has been calculated (fig.4.2). The measured distribution is compared with the predictions of the terrace-step-kink model (TSK) [Wee80] and a model of Williams and Bartelt (WB, solid line) [Bar90,1]. The TSK model assumes no energetic interactions between the steps. However, the migration of a step is limited by its inability to cross neighbouring steps. This leads to a decrease in the entropy of migration and an effective entropic repulsion between steps. The potential felt by a migrating step is therefore an infinite square-well potential of width $2L$, with L corresponding in reality to the average distance between two steps. The probability of a step to pass through x , the coordinate perpendicular to the step edge, is given by the one-dimensional wavefunction $P_{TSK}(x, L) = (1/L) \cos^2(\pi x/2L)$. To calculate from $P_{TSK}(x, L)$ a terrace-width distribution function requires many-body quantum mechanics, associating every step

with a quantum mechanical particle. The result [Bar90,1] is an asymmetric function with a bias against small step separations. The present data for Pt(997) are clearly not consistent with the TSK distribution: the surface exhibits a gaussian distribution centered around the nominal width of 8.5 atom spacings (fig.4.2).

Such a distribution is indeed consistent with the WB model assuming the presence of an additional step-step energy $U(x)$. The WB model yields a symmetric step distribution function $P_{WB}(x) = (1/\sqrt{2\pi}) \exp(-x^2/2w^2)$, with the gaussian width parameter w depending on the exact shape of the potential $U(x)$ [Bar90,1]. $P_{WB}(x)$ turns out to be a good approximation for the terrace width distribution. Fig.4.2 shows the best fit to the Pt(997) data, which is obtained with $w = 2.9\text{\AA}$. For elastic or dipole-induced interactions of the form $U(x) = A/x^2$ the ratio w/L is a direct measure of the ratio of the step interaction strength A to the effect of the entropic interaction $g(T) \equiv B_{TSK}(T)$ within the TSK model. For Pt(997) ($L=20\text{\AA}$), $w/L=0.14$ and the A/g -ratio is determined to be $A/g = 59.6/|\vec{a}_\perp|$, where \vec{a}_\perp is the unit vector perpendicular to the step edge. Accordingly the magnitude of the step interaction term in the total free energy $\gamma(\alpha, T)$ is increased by two orders of magnitude compared to the TSK model: $B_{WB}(T) = 108 g(T)$.

An important result concerning the use of Pt(997) as an Echelette grating for He waves is the standard deviation of the terrace width distribution ($w = 2.9\text{\AA}$). As pointed out in Ref. [Kuh92,1], this is far below a limit where diffraction peak broadening would affect the performance of the surface as monochromator or analyser.

4.2.2 Orientational instability of Pt(997)

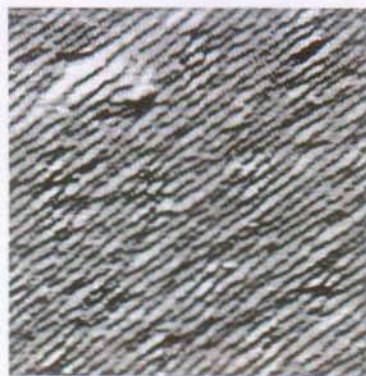
Measurements of Comsa et al. [Com80, Com82] showed that the surface structure of Pt(997) changes upon oxygen adsorption, provoking either step doubling or faceting, depending on temperature. When dosing the surface to oxygen at temperatures between 600K and 900K, terraces with double widths separated by double height

Fig.4.3: (next page) Thermal evolution of Pt(997): all images were obtained by flashing the crystal to the indicated temperatures and quenching to room temperature before imaging. a) 920 K, (image size $750 \text{ \AA} \times 750 \text{ \AA}$), b) 980 K ($1200 \text{ \AA} \times 1200 \text{ \AA}$), c) 1060 K ($1200 \text{ \AA} \times 1200 \text{ \AA}$), d) 1160 K ($1200 \text{ \AA} \times 1200 \text{ \AA}$), e) 1150 K ($880 \text{ \AA} \times 880 \text{ \AA}$), f) Schematic model of the partially faceted surface (in e) as obtained by STM line scans.

steps were observed. The so prepared surface remained stable upon cooling to room temperature and subsequent reduction in a hydrogen atmosphere. Upon heating in an oxygen atmosphere to 1200 K, partial faceting of the surface was observed.

Fig.4.1d shows a STM image of Pt(997) after the surface was heated in $5 \cdot 10^{-8}$ mbar oxygen at 700 K for about 30 minutes. The image was taken after quenching the crystal to room temperature. Step-doubled regions can be observed to coexist with small regions of the "nominal" single-step arrangement. The terrace-step ordering of the step-doubled regions is by far less regular than the order on the clean surface (fig.4.1b). The phase boundary between the double- and single-step regions appears to be stabilized by round spots, supposed to be oxygen islands or oxidised zones, which are imaged as bright bumps. They seem to prevent a further growth of the double terraces. Attempts to improve the ordering of the step-doubled regions, to obtain a completely reconstructed surface or to remove the impurities were not successful. Neither a choice of different annealing temperatures or oxygen pressures nor subsequent reduction of the surface in a hydrogen atmosphere changed the surface morphology substantially.

The STM measurements demonstrate that the partial faceting of Pt(997) is a property of the clean surface. Faceting begins upon flashing the crystal to temperatures above about 950 K [Hah94,2]. Oxygen exposure is not required to induce the reconstruction. Fig.4.3 demonstrates the thermal evolution of Pt(997). The images were obtained by flashing the surface to the indicated temperatures and subsequent



200 Å a)



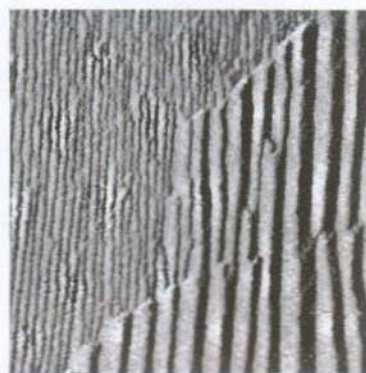
500 Å b)



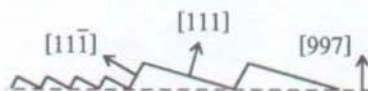
500 Å c)



500 Å d)



200 Å e)



f)

quenching (-50K/s) to room temperature in order to freeze in the obtained morphology (the efficiency of the freezing technique has recently been demonstrated by Michely et al. [Mic91,2] for island and defect structures on Pt(111)). Up to 900K the single-step vicinal arrangement is stable and shows only a slight increase in the width of the step-distance distribution (see fig.4.2). This behaviour demonstrates the absence of a thermal step roughening transition, which would result in a substantial broadening. Above 900K the surface morphology changes drastically. At 920K a low density of local distortions (about $4 \times 10^{-7} \text{ \AA}^{-2}$) is observed (fig.4.3a), and flat (111) terraces of double or triple width are generated. In contrast to the case in fig.4.1c where the step pinning is caused by impurities there is no indication for the presence of impurities in fig.4.3a. With increasing temperature the density and extension of the distortions increases. Upon flashing the surface to 980K (fig.4.3b) the distortion density amounts to $2 \times 10^{-5} \text{ \AA}^{-2}$ and the beginning of faceting is noticed, since the distorted terraces now extend up to three or four nominal terrace widths. Further temperature increase leads to a growth of the local (111) facets while their density remains nearly unchanged (1060K, fig.4.3c). At 1160K we finally observe fully faceted regions on the surface (fig.4.3d). Individual facets reach widths up to 300Å. The series of STM images clearly reveals a nucleation and growth mechanism of the thermal faceting. With increasing temperature first the number of nucleation centers increases until a saturation density is reached. Upon further heating the facet nuclei grow in size and finally whole surface regions become faceted via coalescence.

Fig.4.3e shows that upon faceting two phases coexist on the surface: fully faceted regions and regions where the nominal Pt(997) structure has "survived". The nominal single-step region shows still an almost perfect step ordering. The phase boundary between faceted and nominal regions is very abrupt and seems not to be stabilized by impurities. The image reveals also a surprising detail of the faceted region, the individual facets appear to be ordered in a nearly periodic one-dimensional pattern

with a lattice parameter of about 70 Å. The crystallography of the facets is indeed unique, the "hills" are close-packed (111) faces. This behaviour is illustrated in the schematic model in fig.4.3f, which has been inferred from STM line scans. After annealing the partially faceted surface for several minutes at 900 K, no faceted regions were observed anymore, indicating that the phase transition is reversible.

In the following the physical origin of the morphology changes of the vicinal Pt(997) surface will be examined. As already mentioned, the actual morphology is determined by the delicate balance between the step creation energy $\beta(T)$, the step-step interaction energy $B(T)$ and the terrace energy γ_0 . An initially stable surface will be subject to an orientational instability if a physical (temperature) or chemical (impurity) process affects selectively the energy costs of steps or the terrace energy or if the process affects both energies with different sign.

A transition from single to double height steps on a vicinal Ni surface close to (111) was recently observed by He scattering [Sib93]. The critical oxygen coverage necessary to induce the reconstruction was determined to be very close to the number of Ni step sites. This suggests that step doubling might be caused by the modification of the step energy $\beta(T)$. Obviously oxygen decoration lowers the energy cost for creation of double steps. The step repulsion energy decreases since double steps increase the average step separation. As a net result the stable surface morphology will be a regular vicinal structure with double height steps and double width terraces.

The thermal faceting, on the other hand, appears to be driven by a change in terrace energy γ_0 . At low temperatures the Pt(111) terraces are known to bear a substantial tensile stress of about 0.35 eV/Å² [Nee91]. The atom density at a surface under tensile stress is lower than optimal, therefore there is a tendency to lower the surface energy by increasing the density towards the optimum value. Pt(111) has therefore an inherent tendency to surface reconstruction through a transfer of excess atoms into the surface layer. Bott et al. [Bot93] and Sandy et al. [San93]

demonstrated recently that such a reconstruction can indeed be induced on Pt(111) by enhancing the Pt gas-phase chemical potential or heating the surface to above 1300K. In the reconstructed phase the excess surface atoms are accommodated in a domain wall network with a "unit cell" of about 100-300 Å. The mesoscopic domain wall network can only develop on sufficiently large terraces. So the temperature induced strain relief of the (111) terraces apparently drives the faceting of the Pt(997) surface.

A first indication for the presence of a domain wall network on the (111) terraces of the facets is given in the inset of fig.4.3d. The image reveals the presence of faint corrugation lines separated by about 50 Å. The proof for the reconstruction is given by helium diffraction measurements performed with the new three axes spectrometer build in our group. He diffraction profiles around the specular peak of the (111) show diffraction signatures which can be associated with a mesoscopic facet ordering and the terrace reconstruction (for details see [Hah94,2]). The inferred real space distance of 130 Å nicely agrees with the characteristic distance of the domain wall network of 100-300 Å as revealed by X-ray diffraction measurements [San93].

4.3 Complete chemical passivation of Pt(997)

As mentioned in chapter 4.1, a reliable long-time use of the Pt(997) surface for quantitative measurements in a helium spectrometer requires its passivation against adsorption of molecules from the residual gas atmosphere, consisting mainly of H₂, CO, CO₂, H₂O and hydrocarbons to a smaller extent. Upon adsorption of 0.05ML of CO, for instance, the specular He reflectivity of the (111) terraces is reduced by 50% [Poe83] due to the large diffusive scattering cross section of the CO molecules. Adsorption of H₂O or CO₂ has a comparable effect, but they stick to Pt(111) only at temperatures below 150K [Fis80, Liu91]. On the other hand, a Pt(111) surface covered by a full monolayer of hydrogen which is by far the largest component of the

residual gas, has a He reflectivity of about 80% of clean Pt(111) [Poe86] (hydrogen forms a (1×1) overlayer on Pt(111)).

By RAIRS measurements it will be shown in the following chapters that in addition, hydrogen-saturated Pt(997) is highly inert with respect to ambient gases. Because of the mentioned particular role of CO, I will concentrate on a quantitative analysis of the CO/H coadsorption on Pt(997).

4.3.1 CO on clean Pt(997)

The adsorption of CO on clean Pt(997) was studied by RAIRS and LEED in the temperature range of 100-350K. Fig.4.4 shows infrared absorption spectra of CO adsorbed at 300K as a function of increasing exposure. Initial adsorption leads to the formation of a band at 2061cm^{-1} (full width at half maximum (FWHM) 10cm^{-1}), shifting to 2072cm^{-1} with increasing coverage. A second, higher frequency band appears at 2082cm^{-1} upon CO exposure of 0.07L (1L (Langmuir)= 10^{-6} mbar · s). Its peak maximum shifts to 2090cm^{-1} at saturation coverage, its halfwidth decreases from 14.5cm^{-1} at 0.07L to 9cm^{-1} at saturation. The low frequency band decreases continuously in intensity and has disappeared at CO saturation coverage. Upon CO deposition at lower temperatures no substantial change is observed but a slight shift of the bands to higher frequencies (2101cm^{-1} at saturation and 100K). The occurrence of these two bands resembles those observed in the adsorption of CO on Pt(335) [Hay85,2; Lam90], where the first band was assigned to CO molecules at step edge sites, whereas the second band indicates the occupation of terrace on-top sites. A strong dipole-dipole coupling between the two modes that are close to each other in frequency leads to an intensity borrowing of the higher frequency band at the expense of the lower one, so that only one single line at saturation coverage remains.

In addition, at higher CO exposures ($>0.2\text{L}$) an absorption band in the bridging region around 1850cm^{-1} is observed. Fig.4.4b shows the bridge band at saturation

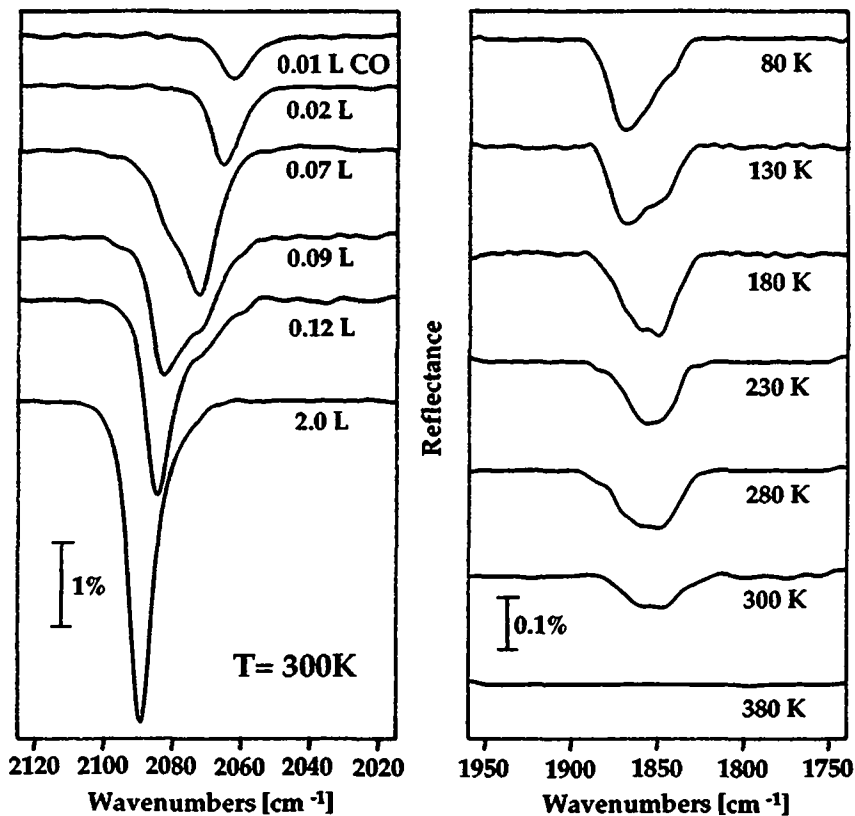


Fig.4.4: (a, left hand side) RAIR spectra of CO on Pt(997)-top and edge-sites adsorbed at $T_s=300\text{ K}$ as a function of exposure. Resolution 4 cm^{-1}

(b, right hand side) RAIR spectra of CO on bridge sites at saturation coverage as a function of adsorption temperature. Resolution 4 cm^{-1}

coverage as a function of CO deposition temperature. This band is most intense at the lowest temperatures, here the peak maximum is located at 1871 cm^{-1} and a



Fig.4.5: LEED pattern of the $c(4 \times 2)$ -structure of CO on Pt(997). $T_s=250$ K, exposure 0.5 L, electron energy 100 eV.

shoulder at 1853 cm^{-1} is present. When the CO adsorption temperature is increased, the low frequency shoulder grows and the peak maximum shifts downwards. At 230 K, the band becomes symmetric around 1850 cm^{-1} (FWHM 43 cm^{-1}). At higher temperatures the band loses intensity, above 350 K no bridge-bound CO is present anymore.

The complex behaviour of the peak shape suggest that several contributions are involved, as already known for CO on Pt(111) at low T_s [Tüs88]. On the flat surface a $c(4 \times 2)$ overlayer is formed at $\Theta_{CO}=0.5$, in which half of the CO molecules are adsorbed on on-top sites and the other half on bridge sites. (At $T_s=250$ K an order-disorder transition occurs [Sch89].) In the corresponding RAIR spectra, a single bridge peak is present at this coverage. For $\Theta_{CO} > 0.5$, a variety of compression structures is observed by LEED, explained by the presence of in-phase and anti-phase domains of the $c(4 \times 2)$ structure separated by "fault lines" of higher local CO density. Correspondingly, the behaviour of the bridging band becomes very complex, up to 8 different peaks can be distinguished depending on Θ_{CO} and T_s . This is interpreted by a superposition from different co-existing structures differing in the distribution of CO molecules between on-top and bridge sites [Tüs88].

On Pt(997), no ordered compression structures are observed by LEED at high CO coverages. However the $c(4 \times 2)$ superstructure is clearly present at exposures of about 0.5L, together with a diffuse background (fig.4.5). This is in contrast to LEED measurements of CO on Pt(112) [Hen89] and Pt(335) [Hay85,2] where no or different ordered structures were observed. This difference is obviously due to the larger width of the close packed terraces on Pt(997), being wide enough to permit the formation of $c(4 \times 2)$ -islands. The LEED pattern was very sensitive to the beam of the electron gun. The best ordered structure develops upon adsorption at 250K, while at higher temperatures the spots decrease in intensity and disappear at 350K together with the bridge bound CO observed by RAIRS. A CO exposure of >0.5 L leads only to an increase of the diffuse background, independent of T_s . This indicates the presence of disordered CO at higher coverages being adsorbed on different sites.

4.3.2 Hydrogen adsorption on a CO precovered surface

The coadsorption of hydrogen and CO on Pt(111) has been extensively studied by various techniques. Both TEAS [Ber87] and RAIRS [Hog88] experiments reveal that repulsive interactions in the mixed adlayer lead to the formation of pure CO islands of higher local coverage than the average CO coverage. At coverages even below $\Theta_{CO} = 0.1$, islands with local coverages up to 0.5 were observed by the appearance of the $c(4 \times 2)$ structure. The size of the islands was largest around 150K. In the presence of higher H_2 -pressures in the 0.001 to 0.1 mbar range the hydrogen induced desorption of preadsorbed CO is observed [Par90, Par91]. The repulsive H-CO interaction (6-8 kcal/mol in a nearest-neighbour model) reduces the desorption activation energy of CO (31kcal/mol at low coverage) to a value smaller than the heat of adsorption of hydrogen (19kcal/mol). Two or three hydrogen atoms are assumed to mediate the displacement of each CO molecule. The weaker bound CO in the compressed adlayer at $\Theta_{CO} > 0.5$ begins to desorb at 130K, whereas the $c(4 \times 2)$ adlayer at $\Theta_{CO}=0.5$ is

On Pt(997), no ordered compression structures are observed by LEED at high CO coverages. However the $c(4 \times 2)$ superstructure is clearly present at exposures of about 0.5L, together with a diffuse background (fig.4.5). This is in contrast to LEED measurements of CO on Pt(112) [Hen89] and Pt(335) [Hay85,2] where no or different ordered structures were observed. This difference is obviously due to the larger width of the close packed terraces on Pt(997), being wide enough to permit the formation of $c(4 \times 2)$ -islands. The LEED pattern was very sensitive to the beam of the electron gun. The best ordered structure develops upon adsorption at 250K, while at higher temperatures the spots decrease in intensity and disappear at 350K together with the bridge bound CO observed by RAIRS. A CO exposure of >0.5L leads only to an increase of the diffuse background, independent of T_s . This indicates the presence of disordered CO at higher coverages being adsorbed on different sites.

4.3.2 Hydrogen adsorption on a CO precovered surface

The coadsorption of hydrogen and CO on Pt(111) has been extensively studied by various techniques. Both TEAS [Ber87] and RAIRS [Hog88] experiments reveal that repulsive interactions in the mixed adlayer lead to the formation of pure CO islands of higher local coverage than the average CO coverage. At coverages even below $\Theta_{CO} = 0.1$, islands with local coverages up to 0.5 were observed by the appearance of the $c(4 \times 2)$ structure. The size of the islands was largest around 150K. In the presence of higher H_2 -pressures in the 0.001 to 0.1mbar range the hydrogen induced desorption of preadsorbed CO is observed [Par90, Par91]. The repulsive H-CO interaction (6-8 kcal/mol in a nearest-neighbour model) reduces the desorption activation energy of CO (31kcal/mol at low coverage) to a value smaller than the heat of adsorption of hydrogen (19kcal/mol). Two or three hydrogen atoms are assumed to mediate the displacement of each CO molecule. The weaker bound CO in the compressed adlayer at $\Theta_{CO} > 0.5$ begins to desorb at 130K, whereas the $c(4 \times 2)$ adlayer at $\Theta_{CO} = 0.5$ is

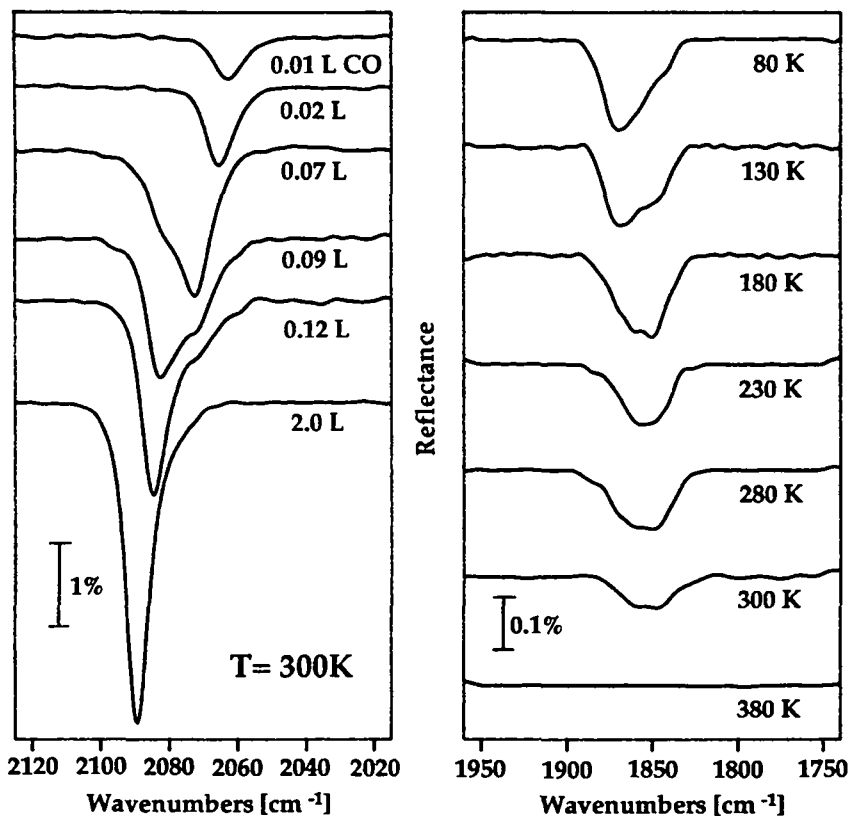


Fig.4.6: (a, left hand side) RAIR spectra of 0.1 L CO adsorbed at $T_s=165$ K as a function of subsequent H_2 -exposure at the same temperature. Resolution 4 cm^{-1} , 200 scans averaged.

(b, right hand side) RAIR spectra of CO at saturation coverage after predosing the surface with hydrogen at $T_s=165$ K. Resolution 4 cm^{-1} , 800 scans averaged.

more stable and is displaced only above 300 K.

On Pt(997) the nearly complete removal of CO in the presence of a hydrogen

atmosphere occurs already at temperatures above 150K. Fig.4.6a shows an example: a CO predose of 0.1L at 165K was chosen, the shoulder due to the edge-bound CO can still be seen. At the same temperature, the surface was then exposed to $5 \cdot 10^{-5}$ mbar hydrogen. An exposure of 3.000L hydrogen reduces the intensity of the CO band by a factor of 3, at 32.000L hydrogen it is reduced by a factor of 10. After an extended hydrogen treatment (100.000L H_2), only a weak band at 2069 cm^{-1} remains, corresponding to a small amount of CO adsorbed at step sites (less than 0.03ML, as estimated by a comparison of the integrated intensities of the step peak). No CO site conversion from top- to bridge-sites is observed upon hydrogen coadsorption, which would indicate CO island formation. Thus it can be concluded that preadsorbed CO is removed by the adsorbed hydrogen.

The differences to Pt(111), i.e. the considerably lower H_2 -pressure required to desorb CO and the lower desorption temperature, can be related to the details of the adsorption mechanism of hydrogen on Pt(111). It is well known that the adsorption of H_2 on Pt(111) is mediated by steps as dissociation sites [Ber75], at least at low temperatures. Hydrogen adsorption can not be inhibited by decorating the steps with CO [Len87]. Because the step density on Pt(997) is two orders of magnitude higher than on a well prepared Pt(111) surface, the sticking probability of hydrogen is substantially increased with respect to Pt(111) and a lower hydrogen pressure is sufficient to remove CO. In addition, the desorption activation energy E_d for terrace-bound CO on stepped platinum surfaces (27.4kcal/mol at low coverage to 23.3kcal/mol at saturation on Pt(335) [Luo92], 28.5-22.5kcal/mol on Pt(112) [McC77], 27-24kcal/mol on Pt(S)[6(111)x(100)] [Col77]) is lower than E_d for the more strongly bound CO on Pt(111) (32kcal/mol at low coverage to 28kcal/mol at $\theta=0.5$ [Ert77]). The reduced binding energy on the stepped surfaces which are closer to E_d of the CO in the compressed adlayer on Pt(111) (<23kcal/mol [Ert77]) may explain the removal of the terrace CO to occur already at lower temperatures. The studies [Luo92], [McC77]

and [Col77] found that CO is up to 8kcal/mol more tightly bound to the step sites than to the terrace sites. This difference can not be completed by the increased heat of adsorption of hydrogen on steps (3kcal/mol [Poe81]) and so the removal of the step CO remains incomplete.

4.3.3 CO adsorption on a hydrogen precovered surface

On Pt(111), adsorbed hydrogen reduces not only the CO saturation coverage but also the CO sticking coefficient even at low CO coverages [Jia92]. A full monolayer of hydrogen ($\theta_H=1$) prevents subsequent adsorption of CO even after extended exposure, as revealed by TEAS [Len87]. Fig.4.6b displays the IR spectra of CO at saturation coverage on Pt(997) predosed to hydrogen at 165K. The bottom spectrum presents CO on clean Pt(997) for comparison. Upon preexposure of 10.000L H₂, the CO absorption band intensity is reduced by a factor of 3. The higher CO exposure (10L) necessary to ensure saturation indicates the lowering of the sticking coefficient by preadsorbed hydrogen. Increasing the hydrogen predose leads to a further weakening and broadening of the CO absorption band, which in addition shifts to lower wavenumbers. After saturation with 60.000L H₂ only a weak band (FWHM 50cm⁻¹) centered at 2065cm⁻¹ remains, corresponding to about 0.03ML of CO supposed to be mainly adsorbed at step sites. Considering that the residual gas atmosphere in a standard UHV system contains about $1 \cdot 10^{-11}$ mbar CO, it would take more than 50 days until the indicated amount of 0.03ML CO has adsorbed and a noticeable reduction of the helium diffraction intensity would occur.

4.3.4 Structure of the H/Pt(997)-surface and conclusions

The coadsorption experiments reveal that covering the Pt(997) surface with a full monolayer of hydrogen provides a long-term passivation against CO adsorption. It is necessary to keep the crystal at a temperature of 165K to minimize hydrogen desorption [Poe86] and to prevent H₂O sticking to the surface, through direct adsorption

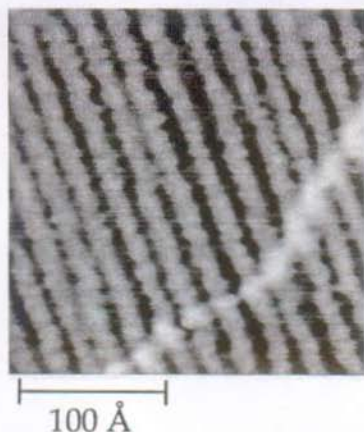


Fig.4.7: STM image of the hydrogen-saturated Pt(997) surface taken at $T_s=165$ K. The white dots represent a step running in a different direction, due to the slight misalignment of the crystal from (997).

or reaction with residual oxygen (the desorption temperature of H_2O from Pt(111) is 150 K [Fis80]). To conserve the complete hydrogen monolayer, the crystal must therefore be permanently exposed to an atmosphere of 10^{-9} to 10^{-8} mbar hydrogen. No quantitative analysis concerning the adsorption of hydrocarbons was performed, which are present to a certain amount in the residual gas. However, no evidence for C-H species were detectable on the surface even after long-time exposure of the passivated surface to the residual gas. It is indeed well known from previous hydrogen/ethylene coadsorption studies on Pt(111) [Ste82], that already a precoverage of 0.9 ML hydrogen reduces the sticking coefficient for ethylene by an order of magnitude. Also the amount of hydrogenate products decreases sharply at high H-precoverages. We can thus conclude that the H/Pt(997) surface with $\Theta_H = 1$ is completely passivated against residual gas adsorption at $T_s=165$ K.

In view of its use in helium diffraction, this result would be of no use if the surface underwent a structural change upon hydrogen exposure. As indicated by the absence of additional LEED spots, hydrogen forms a (1x1) structure on the terraces as expected from the Pt(111) data, from which it was also concluded that the hydrogen atoms are coordinated in threefold hollow sites. Fig.4.7 shows a STM image of the

H/Pt(997) surface ($\theta_H=1$) taken at 165K. Neither the average terrace width nor the terrace width distribution is markedly changed by the hydrogen overlayer. This is also consistent with a former TEAS study of H/Pt(997) [Poe81], which reported that a hydrogen monolayer does not change the positions and widths of the diffraction peaks with respect to the clean surface. Only the intensities of the higher order peaks are found to be reduced to about 60%.

To summarize this chapter, it has been shown by structural investigations and by the development of a chemical passivation method that the Pt(997) surface is suitable to serve as a diffractive element in atom beam optics. In fact the passivation technique is successfully employed in the helium scattering device in our institute.

4.4 Nitrogen dioxide and nitrous oxide on Pt(997)

Fig.4.8a shows RAIR spectra of N_2O on Pt(997) adsorbed at a surface temperature of $T_s=30$ K. Adsorption of small submonolayer doses (0.5L) produces an infrared band at 2235cm^{-1} . With increasing exposure, two other peaks at 583cm^{-1} and 1286cm^{-1} appear. The intensity of the bands does not saturate upon further exposure indicating the formation of a N_2O multilayer. At 7L, the three initial bands have slightly shifted to 2243cm^{-1} , 1290cm^{-1} , and 588cm^{-1} respectively, and two new bands at 2569cm^{-1} and 2348cm^{-1} have developed. The assignment of the infrared absorption bands is simple and follows that of the gas phase infrared spectrum of N_2O [Her45] (see table below).

Mode	Gas phase	on Pt(997)	
		(mono-)	(multilayer)
NNO-bending mode	589	583	588
NO-stretch	1285	1286	1290
NN-stretch	2223	2235	2243
NO-str. overtone	2563	-	2569

The small band at 2348cm^{-1} can not be associated with a vibrational mode of gas phase N_2O . However, gaseous CO_2 shows a very strong infrared band at 2349cm^{-1} [Her45]. Therefore it is assumed that some CO_2 has adsorbed during the measurements. CO_2 is present in the residual gas and as an impurity (0.1%) in the N_2O gas which was used as provided without further purification.

When heating the adsorbed multilayer to 75 K, the bands sharpen considerably (all bands exhibit a FWHM of 20cm^{-1} at 30 K and 14cm^{-1} at 75 K), indicating an ordering process (fig.4.8b). At 90 K, the multilayer has obviously desorbed. Finally, upon annealing at 110 K, no bands are present anymore. The observed desorption temperatures correspond exactly to those for the mono- and multilayer of N_2O on Pt(111) [Ave83] and Ir(111) [Cor90]. Like on these surfaces and despite the high step density on Pt(997), no dissociation of the N_2O molecules occurs. This can be concluded from the absence of infrared bands characterizing atomic O or N, or NO. In contrast, N_2O decomposes on Ni(100) [Hof87,2], Ni(110) [Sau81] and Ru(100) [Sch86].

On Pt(111), N_2O is bound through the nitrogen end of the molecule, the N-N-O axis being undistorted from linearity [Ave83]. The strongest evidence for this assumption is a NN-stretch mode blue-shifted by 80cm^{-1} from the gas phase value whereas for the other modes little or no adsorption induced shift was seen. The strong shift was explained by a stiffening of the NN bond as a result of kinematic coupling to the massive metal atom which is not outweighed by backdonation of electrons into the unfilled, N-N antibonding 3π -orbital of the molecule. On Pt(997) the observed shift of the mentioned mode is considerably lower, but it seems reasonable to assume a similar adsorption geometry.

The behaviour of NO_2 on Pt(997) is much more complex. This molecule shows a strong tendency to decompose on stainless steel walls. Therefore the steel tubes of the gas inlet were passivated in an acid bath before mounting and subsequently pumped and baked out daily before being filled with fresh NO_2 . Fig.4.9 presents a series of

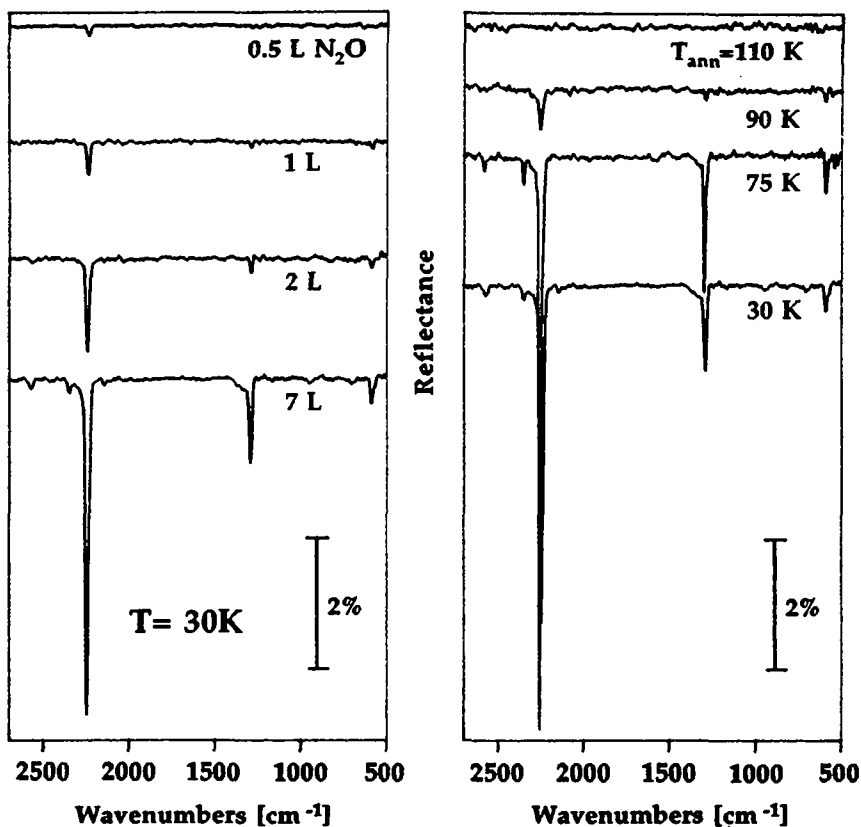


Fig.4.8: (a, left hand side) RAIR spectra of N₂O on Pt(997) adsorbed at $T_s=30$ K as a function of exposure. Resolution 4 cm⁻¹, 400 scans averaged.

(b, right hand side) RAIR spectra of 7 L N₂O adsorbed at 30 K (bottom spectrum) and after annealing at the indicated temperatures and recoiling to 30 K before spectra recording. Resolution 4 cm⁻¹, 400 scans averaged.

RAIR spectra as a function of NO₂ exposure at 80 K. Upon initial adsorption, a broad

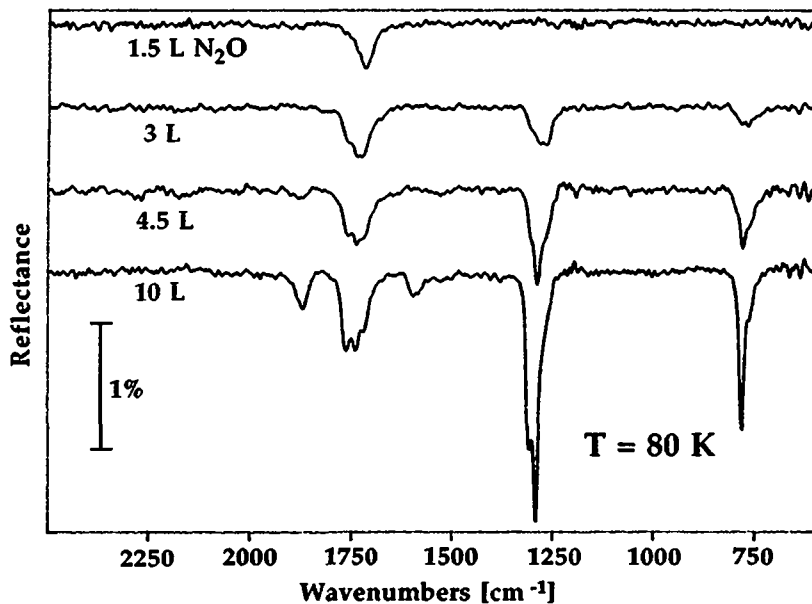


Fig.4.9: RAIR spectra of NO_2 adsorbed on Pt(997) at $T_s=80\text{ K}$ as a function of exposure. Resolution 2 cm^{-1} , 400 scans averaged.

absorption band at 1717 cm^{-1} is present. In the 3L spectrum, this peak develops a shoulder at 1750 cm^{-1} and two bands at 1273 cm^{-1} and 760 cm^{-1} are formed. With increasing coverage the band at 1750 cm^{-1} becomes more intense and develops into a doublet. A second, strong doublet at 1300 cm^{-1} can be seen, the band at 1273 cm^{-1} remains as a shoulder. The band at 760 cm^{-1} develops into a sharp peak at 781 cm^{-1} with a shoulder at 762 cm^{-1} . Finally, at the highest exposure (10L), two additional bands at 1870 cm^{-1} and 1592 cm^{-1} are observed.

The occurrence of the band at 1717 cm^{-1} shows that NO in on-top configuration is present on the surface. This was revealed by exposing the crystal directly to NO

and the detection of a similar peak. The bands at 760 and 1273 cm⁻¹ are assigned to the NO₂ bending mode and the ONO symmetric stretch mode (see table below).

Mode	Gas phase NO ₂	Solid N ₂ O ₄	on Pt(997)	
			(mono-)	(multilayer)
NO ₂ bend	750	750	760	781
ONO s-stretch	1318	1253	1273	1300
ONO a-stretch	1610	1734	-	1750

The other bands except the mode at 1870 cm⁻¹ are due to the formation of a solid N₂O₄ multilayer ([Tak80], [And91], [Sch86]; the band at 1590 cm⁻¹ is an overtone of the bending mode), which will not be treated further here. In the intermediate coverage range, the multilayer spectrum does not screen the monolayer, indicating that the chemisorbed monolayer retains its bonding integrity as the condensation of the multilayer proceeds. The spectra in the monolayer range are surprisingly different from those of NO₂ on Pt(111) [Bar87], where three bands at 795, 1180 and 1560 cm⁻¹ were observed, indicating C_s bonding symmetry. The formation of a Pt(111) μ -N,O-nitrito surface complex was proposed, the NO₂ being bound to the surface through an O and the N atom. On Pt(997), however, the asymmetric stretching mode is not observed and the symmetric stretch is much less red shifted. This indicates a bonding with higher symmetry (C_{2v}), most likely the molecule is bound through the nitrogen end to the Pt(997) surface, as on Ru(001) [Sch86]. The absorption feature at 1870 cm⁻¹ can not be due to a vibrational mode of NO₂ or N₂O₄. This is essentially the stretching frequency of NO in the gas phase (1873 cm⁻¹), chemisorbed NO₂ must therefore facilitate the uptake of NO from the background. A similar phenomenon was observed on Au(111) [Bar89], where the formation of a N₂O₃ compound is responsible for the NO uptake. From the presence of NO in the background gas due to decomposition of NO₂ on the sample chamber walls, it can be concluded that the presence of NO in the initial stages of adsorption is not a necessary

result of decomposition on the surface itself, but likely due to direct adsorption from the residual gas. This is confirmed by an annealing experiment (not shown). Upon heating to 140K, the NO₂ mono- and multilayer have both desorbed. The absorption band at 1717cm⁻¹ is still present, but not more intense than upon adsorption at 80K, showing the absence of thermal decomposition. Obviously background NO passivates the Pt(997) surfaces by occupying the step edge sites. Subsequently, NO₂ can adsorb molecularly on the terraces, as it does on Pt(111) [Bar87].

5. Submonolayer and multilayer growth of Cu on Pd(110)

5.1 Introduction

Theoretical and experimental investigation of thin film epitaxy has a long history which led to a classification into three growth modes: Volmer-Weber (VW), Stranski-Krastanov (SK) and Frank-van der Merwe (FM) growth (Fig.5.1). From a thermodynamic point of view, the behaviour of epitaxial films depends on the relative magnitudes of the surface free energies [Bau58]. One obtains the FM growth mode, if the condition $\gamma_{f,n} + \gamma_{i,n} \leq \gamma_s$ is fulfilled independent of the film thickness (n : number of layers). Here is $\gamma_{i,n}$ the interface energy per unit area, $\gamma_{f,n}$ and γ_s are the surface free energies of the film and the substrate per unit area, respectively. $\gamma_{i,n}$ contains the n -dependent strain energy in the film, which is caused by the structural misfit between adlayer and substrate. If the strain energy is positive and increases with the film thickness, then at a given n the FM condition is no longer valid and SK growth occurs. If the FM condition is not fulfilled even for $n=1$, three-dimensional islands grow from the very beginning (VW growth).

However, films are often grown under experimental conditions far from thermal equilibrium, for instance at low temperatures or high deposition rates. Here, additional factors like restricted surface atom mobilities lead to structures not expected from energetics. A transition from 2D to 3D growth can occur by the existence of an activation barrier preventing the descent of adatoms from the top of growing islands onto lower terraces. The height of the barrier depends on the size scale of the growing structures [Poe91]. Not only growth modes, but also island densities and island shapes can essentially be determined by kinetics, i.e. the average diffusion length Λ_A of impinging adatoms and the diffusion length of atoms adsorbed at the perimeter of existing islands Λ_L [Mo 91, Mic93, Röd93,2].

The particular interest for Cu/Pd surfaces arises from the use of copper-based

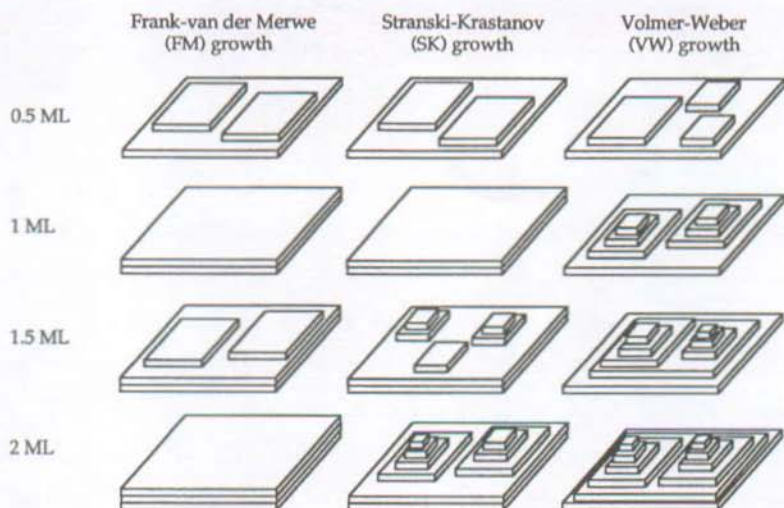


Fig.5.1: Schematic representation of different film growth modes: Frank-van der Merwe or twodimensional growth, Stranski-Krastanov or layer-plus-island growth and Volmer-Weber or three-dimensional growth.

bimetallic surfaces as hydrogenation or CO oxidation catalysts [Cho91] (for more details see chapter 6.1). By tailoring the composition of a bimetallic surface its catalytic activity and selectivity can be controlled. This is the motivation for this combined STM/RAIRS study of the interdependence of chemical and structural properties of different Cu/Pd surfaces.

Previous investigations revealed that copper grows in a layer-by-layer mode on Pd(111) [Ora89] and Pd(100) [Li 89], despite the large lattice misfit of 7%. To my knowledge, no studies of Cu on Pd(110) have been published so far.

5.2 The Pd(110) surface

Palladium is a metal with fcc crystal structure. Its (110) surface is unreconstructed

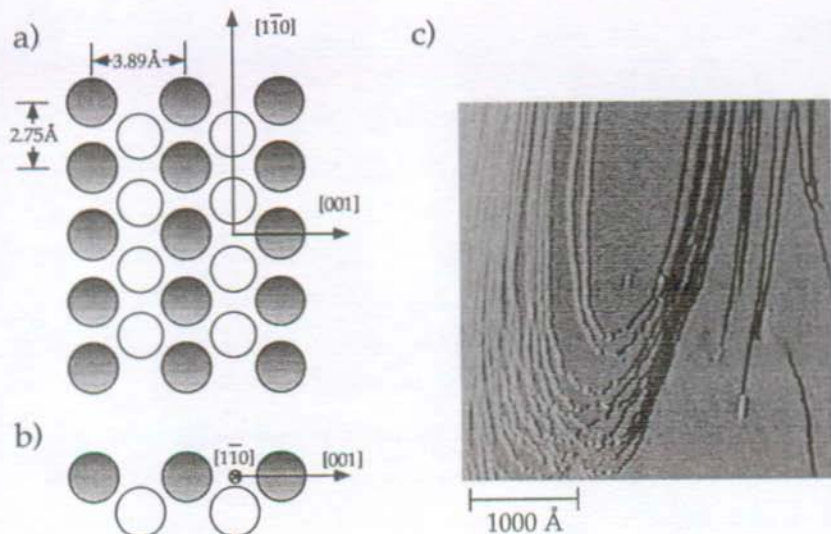


Fig.5.2: Schematic a) top- and b) side view of the Pd(110) surface. The dark circles represent the topmost layer atoms, the light circles are the atoms in the underlying layer.

c) 3500 Å × 3500 Å STM image of the Pd(110) crystal taken in the differential mode. The crystal directions can easily be identified by the shape of substrate steps: steps in the $[1\bar{1}0]$ direction appear smooth, $[001]$ steps appear rough. This difference is due to the higher energy necessary to create a kink in a $[1\bar{1}0]$ step. In the right part of the image, a few screw dislocations can be seen.

[Wol87] and shows a rectangular unit cell with interatomic spacings of 3.89 Å in the $[1\bar{1}0]$ direction and 2.75 Å in the $[001]$ direction. From inspection of fig.5.2a,b it becomes evident that the surface consists of closed packed atom rows separated by "channels" in the $[1\bar{1}0]$ direction. The crystal was prepared in UHV by repeated cycles (ca. 50 cycles in the initial preparation procedure) of 800 eV Ar ion sputtering at 700 K, heating in a $2 \cdot 10^{-6}$ mbar oxygen atmosphere at 620 K and annealing at 950 K. This

resulted in a sharp LEED pattern with low diffuse background. Auger spectra showed no contamination of the surface down to the noise limit of the analyser ($<0.01\text{ML}$). Residual carbon, however, is not detectable by Auger electron spectroscopy since its characteristic three-peak Auger signal at 270eV is completely overlapped by a Pd substrate peak. So the surface cleanliness with respect to carbon was directly verified by STM. The crystal showed an average terrace width of only 85\AA , unusually low for a well prepared low index metal surface, however individual terraces up to 2000\AA wide were observed occasionally (fig.5.2c). The high step density of the sample is not due to a miscut (nominally 0.2°) since up- and down steps are present to the same extent. It is rather attributed to the low step free energy for Pd(110) [Hör93]. Upon heating to 1200°C , a semioordered up-down-step configuration was observed [Hör93], the formation of which was assigned to step-step interactions and/or the presence of tensile stress [Zep93].

5.3 Submonolayer Cu island shapes and Cu adatom diffusion on Pd(110)

Fig.5.3 shows submonolayer copper islands grown on Pd(110) at very low coverages ($\Theta_{\text{Cu}} \leq 0.1\text{ML}$). Copper was deposited by means of the Knudsen cell at a constant rate of 10^{-3} monolayers per second ($1\text{ML}=9.35 \cdot 10^{14}$ atoms / cm^2) at the indicated substrate temperature T_S . The STM images were then taken at the same crystal temperature. All STM measurements were performed in the constant current mode at $0.2\text{-}1\text{V}$ positive or negative tip bias and $0.5\text{-}1.5\text{nA}$ tunneling current. No influence of the tunneling parameters or the sample-tip interaction on the apparent surface morphology was observed.

It becomes immediately evident from the images that the anisotropy of the surface and thus the anisotropy of the Cu adatom diffusion determines the Cu island shapes, especially at low temperatures. At $T_S < 300\text{K}$ (fig.5.3a), linear Cu chains exclusively oriented in the $[1\bar{1}0]$ direction of the substrate are formed. They reach an average

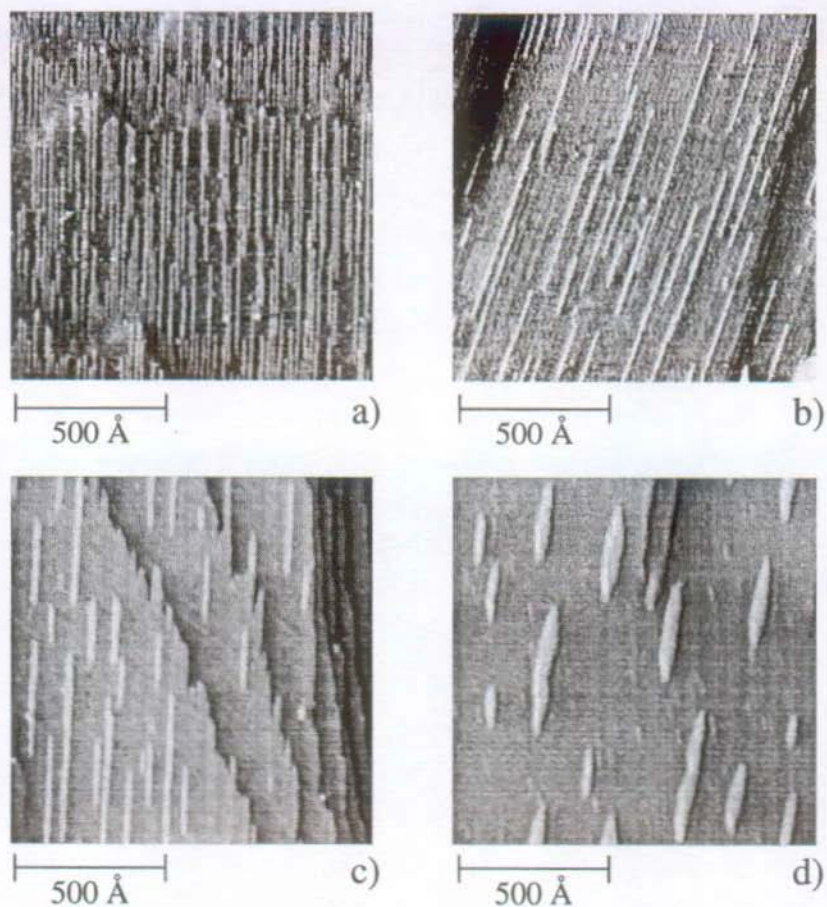


Fig.5.3: STM images of Cu islands grown and imaged on Pd(110) at four different temperatures and the same coverage $\Theta_{Cu}=0.1$ ML except for b) where $\Theta_{Cu}=0.07$ ML. Scale of the images $1200 \text{ \AA} \times 1200 \text{ \AA}$. Temperatures are a) $T_S=265 \text{ K}$, b) $T_S=300 \text{ K}$, c) $T_S=320 \text{ K}$, d) $T_S=350 \text{ K}$.

length of 50 atoms at $T_S=265 \text{ K}$ and $\Theta_{Cu}=0.1$. The chains nucleate partially on step edges running along $[001]$, but also on larger terraces. All chains are of uniform

width; the exact width can not be obtained directly from the image since atomic resolution is missing. The apparent width of a chain is 7\AA , its real width is smaller since the STM tip images a substrate step already 3\AA wide. The real width can however be inferred from the distribution of chain spacings in the $[001]$ direction. This distribution shows discrete peaks at multiples of an elementary distance of $4.0 \pm 0.2\text{\AA}$, corresponding to the inter-row spacings of two neighbouring Pd close packed rows. Cu island separations down to 2 elementary distances are present, indicating that the chains are *monatomic* in width (if the chains consisted of double rows, the minimum distance would be three Pd interatomic spacings) This was confirmed by counting the total chain length per unit surface area and comparison to the Cu coverage. At $T_S=300\text{K}$ (Fig.5.3b), linear Cu chains can reach lengths up to 1000\AA corresponding to aspect ratios as large as $A=300$ (the aspect ratio means here the ratio between the length and the width of an island). Above about 300K , two-dimensional islands begin to form, still being elongated in the $[1\bar{1}0]$ direction. At $T_S=350\text{K}$, typically lens shaped Cu islands are observed. It is obvious from fig.5.3 that the change in island shape with increasing deposition temperature is accompanied by a decrease in island density.

Both island densities and island shapes contain information on the Cu adatom diffusion lengths on Pd(110). Obviously, at $T<300\text{K}$, Cu atoms diffuse exclusively along the $[1\bar{1}0]$ "channels". Consequently, islands are formed as one-dimensional chains. At about 300K , diffusion across the channel walls sets in and 2D-islands start to form. A detailed interpretation of the present data can be done by following the analysis of the density of islands as a function of the substrate temperature as outlined by Mo et al. and Pimpinelli et al. [Mo 91, Pim92]. Their argument is based on the existence of an average "lifetime" τ_A for adatoms, which is controlled by two different collision rates (numbers of collisions per unit time and area): w_{AA} (collisions between two adatoms) and w_{AI} (adatom-island collisions). If two adatoms

meet, they are supposed to form a stable nucleus. An adatom arriving at an existing nucleus sticks to it and is therefore "lost". So the "death rate" of adatoms is

$$\frac{n}{t} = 2w_{AA} + w_{AI} \quad (5.1)$$

where n is adatom density (per cm^2). It can be shown that in a d -dimensional ($d=1,2$) random walk, the number of distinct sites that an adatom has visited after H hops is $H^{d/2}$ (for very large H 's). Defining a jump rate $J = H/t$ and a diffusion coefficient for adatoms $D = Ja^2$ (a : lattice constant), the number of sites that an adatom visits during its lifetime becomes $(D\tau_A/a^2)^{d/2}$. The probabilities that adatoms "die" due to a collision with another adatom ($n_B = n$) or with an island ($n_B = N$) is therefore $n_B a^2 (D\tau_A/a^2)^{d/2}$. Multiplying this with n/τ_A yields the collision rates w_{AA} and w_{AI} :

$$w_{AB} = n n_B a^{2-d} \frac{(D\tau_A)^{d/2}}{\tau_A} \quad B \in \{A, I\} \quad (5.2)$$

In the very beginning of the deposition process only adatoms are present, and eq. (5.1) becomes $n/t \approx 2w_{AA}$. At higher coverage Θ , the lifetime of adatoms is mainly controlled by incorporation into existing islands: $n/t \approx w_{AI}$. If we identify w_{AA} with the nucleation rate dN/dt and w_{AI} with the deposition rate $R = \Theta/t$ (since every deposited atom is captured by a preexisting island at higher coverages), we obtain

$$R = n N a^{2-d} \frac{(D\tau_A)^{d/2}}{\tau_A} \quad (5.3)$$

$$\frac{dN}{d(\frac{\Theta}{R})} = n^2 a^{2-d} \frac{(D\tau_A)^{d/2}}{\tau_A} \quad (5.4)$$

By some easy manipulations, we obtain from (5.3) and (5.4):

$$N^{\frac{2(d+1)}{d}} = \frac{2(d+1)}{d} \left(\frac{R}{D} \right) \Theta a^{\frac{(2d-4)}{d}} \quad (5.5)$$

R and Θ being externally controllable parameters, this equation establishes a simple relation between the adatom diffusion coefficient D and the number density of islands

which is directly accessible by STM. D is simply related to the diffusion prefactor \tilde{D} and the diffusion energy barrier E_D by

$$\frac{D}{a^2} = J = \tilde{D} e^{-\frac{E_D}{kT}} \quad (5.6)$$

Finally in the case of one-dimensional diffusion ($d=1$) we obtain:

$$N^{-1} = \frac{\tilde{D}a^4}{4R\Theta} e^{-\frac{E_D}{kT}} \quad (5.7)$$

In the case of isotropic diffusion ($d=2$) the following relation holds:

$$N^{-2} = \frac{\tilde{D}a^2}{3R\Theta} e^{-\frac{E_D}{kT}} \quad (5.8)$$

In the temperature range from 150 K to 420 K a detailed analysis of the Cu island density on Pd(110) as a function of the deposition temperature was performed [Buc93]. Coverage (0.1 ML) and deposition rate (10^{-3} ML/s) were the same for each deposition temperature. This particular coverage was chosen because the island density was observed to have saturated at 0.1 ML, whereas at higher coverage accidental island coalescence is not excluded. STM measurements were performed at deposition temperature (otherwise the analysis would be useless due to changes in surface morphology during annealing at the STM working temperature). The island counting from the STM images was only performed on large terraces ($>500 \text{ \AA}$) to ensure minimal interference with step regions.

Fig. 5.4 shows logarithmic plots of the overall surface density of Cu islands (in the lower part of the figure) and of the one-dimensional density of islands in the $\{001\}$ direction as functions of $1/T$. The island densities nicely reflect the transition from 1D to 2D growth. The overall island density shows Arrhenius behaviour in the entire temperature range studied, demonstrating that longitudinal diffusion is active down to the lowest measured temperatures. The island density in the $\{001\}$ direction remains constant for $T_S < 300 \text{ K}$, showing that diffusion across the Pd closed

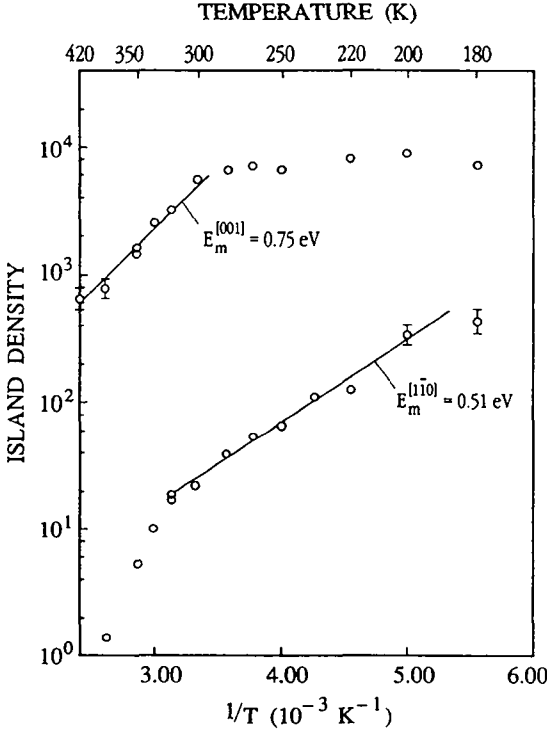


Fig.5.4: Arrhenius plot of the overall density of islands (lower part) and the transverse density of islands (upper part) in arbitrary units as a function of $1/T$.

packed rows does not contribute to the island formation below 300K. Cu atoms travel along the $[1\bar{1}0]$ direction without any transverse migration. In this temperature regime the island formation is a true 1D problem. In this case it is thus justified to consider the island density to obey equation (5.7). The overall Cu island density becomes the one-dimensional density in the $[1\bar{1}0]$ direction. Using the linear part of the lower curve in fig.5.4, an energy barrier of $E_{D,L} = 0.51 \pm 0.05 \text{ eV}$ is obtained for diffusion along the longitudinal $[1\bar{1}0]$ direction. For higher temperatures, both the total and the transverse island density decrease, indicating the onset of formation of two-dimensional copper islands.

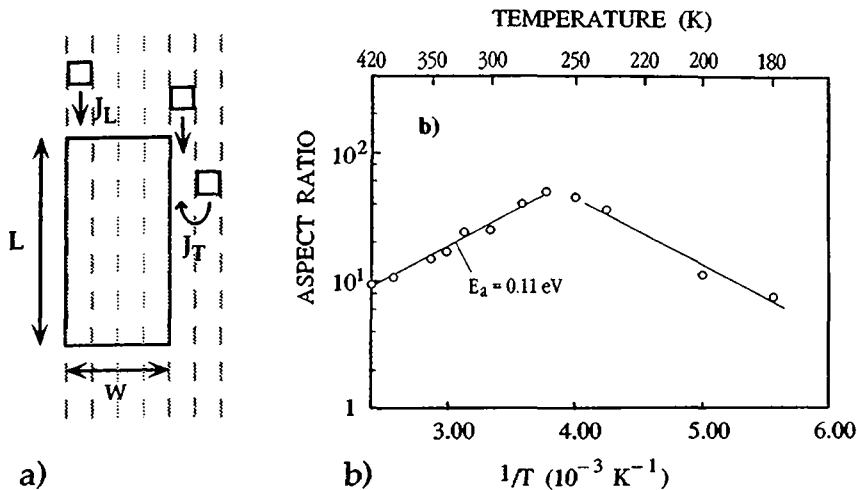


Fig.5.5: a) The island aspect ratio $A=L/W$ reflects the ratio of the growth rates of the islands in the $[1\bar{1}0]$ - (dotted lines) and $[001]$ direction. J_L and J_T are the jump rates in the corresponding directions.

b) Island aspect ratio as a function of $1/T$. The left part, the 2D diffusion regime, provides information on the ratio of the diffusion barriers in the two high symmetry substrate directions, the right part reflects the increase of island density with decreasing deposition temperature.

Information on the diffusion barrier in the $[001]$ direction was obtained by two methods. From the transverse island density as a function of $1/T$, we obtain with equation (5.7) and fig.5.4 (upper part) an energy barrier of $E_{D,T} = 0.75 \pm 0.07 \text{ eV}$ for transverse diffusion. The two-dimensional growth shapes of Cu islands on Pd(110) (fig.5.3) can also be described in a more intuitive manner by analysing the island aspect ratio as a function of deposition temperature. Supposing that atoms land on the surface in a random way and that the neighbourhood of the islands is continuously populated with "fresh" adatoms arriving from the gas phase. The aspect ratio A of

the islands (island length over island width) then reflects the ratio of the growth rates in the $[1\bar{1}0]$ - and the $[001]$ directions (fig.5.5). But while the growth rate of an island along $[1\bar{1}0]$ is proportional to the jump rate J_L , the growth rate along $[001]$ is less trivially related to J_T . As a matter of fact, it is faster than it would be expected just from the ratio J_T/J_L . The jump rate in the "easy" direction, at 300 K, is about 10^4 times faster than across the channel walls, as can be calculated from the energy barriers (it must be assumed that the prefactors \tilde{D}_i are equal, an assumption which seems to be justified for metal atoms on metal substrates [Tso92]). Thus every time a cross-channel migrating atom attaches to the lateral edge of an island, it forms instantaneously an immobile nucleus with another atom diffusing in the corresponding $[1\bar{1}0]$ channel. Then, this row is immediately filled up with atoms moving along this channel. To account for this effect, the transverse jump rate must be multiplied by an enhancement factor. This factor is difficult to estimate a priori since it depends on particular events on the microscopic scale but an estimation of this factor is given by the aspect ratio itself, since it reflects the probabilities for an atom migrating either along $[1\bar{1}0]$ or $[001]$ to encounter an existing island on its walk (fig.5.5). Therefore $A = J_L/(J_TA)$. As already mentioned, the jump rates are directly related to the diffusion coefficients by $D = Ja^2$, thus

$$\frac{J_L}{J_T} = \frac{\tilde{D}_L}{\tilde{D}_T} e^{\frac{E_{D,T} - E_{D,L}}{kT}} \quad (5.9)$$

If we set the prefactor ratio equal to one (see above), we finally obtain

$$\ln A = \frac{1}{kT} \frac{\Delta E_D}{2} \quad \Delta E_D = E_{D,T} - E_{D,L} \quad (5.10)$$

The experimental measurements of the aspect ratio A in the two-component driven diffusion regime shown in fig.5.5 do indeed exhibit the exponential variation as a function of $1/T$. The slope of fig.5.5 gives an activation energy of $\Delta E_D/2 = 0.11$ eV which within this model is in excellent agreement with the difference in energy

barriers obtained from island density analysis ($(E_{D,L} - E_{D,T})/2 = 0.12\text{eV}$). From the aspect ratio data also the stability temperature for isolated Cu adatoms can be determined. In the 1D regime A is a direct measure of the Cu chain length. By extrapolation to low temperatures a stability temperature of 140K can be estimated.

P.Fernandez et al. modeled the system Cu/Pd(110) via N-body interatomic potentials constructed in the framework of the Embedded Atom Method (EAM). The thermodynamic equilibrium structure at $T=0\text{K}$ of the system were studied as well as the dynamical evolution of the system, looking for the detailed Cu adatom diffusion mechanisms promoting cross channel displacements. Their results [Buc93, Mas93] shall be briefly summarized now.

In the EAM slab computations the total energy of a given $\text{Cu}_N/\text{Pd}(110)$ system is obtained by positioning N adatoms on top of the substrate and calculating the relaxation of the system at $T=0\text{K}$. Their adsorption sites correspond either to 1D chains along the $[1\bar{1}0]$ direction, or to 2D structures made of two $[1\bar{1}0]$ -chains of $N/2$ atoms each, separated by 3.89\AA (lattice parameter) along $[001]$. Binding energies are expressed as $E_B = E_{B,N}/N = ((E_N - E_0) - N(E_1 - E_0))/N$, where E_i is the total energy of the system with i adsorbed atoms ($i = 0, 1, N$). Energy barriers for diffusion, denoted by E_D , are calculated by constraining the motion of an atom to specific locations in the XY plane along a given diffusion path, with the rest of the system relaxing at $T=0\text{K}$.

The results, referring to up to $N=20$ adatoms, predict in agreement with the experiment an enhanced stability of the linear chain, by $\Delta E_B=0.085\text{eV}$ for $N=3$, 0.04eV for $N=10$ and still 0.03eV for $N=20$, decreasing linearly as a function of $1/N$ for large N , to yield an asymptotic value $\Delta E_B(N \rightarrow \infty) \approx 0.02\text{eV}$ (fig.5.6). This behaviour can be rationalized on the basis of an N-body interatomic potential, by extracting from the binding energies $E_{B,N}$ two, three and four body effective interactions $E_{F,N}$ and summing up all N-dependent contributions for a given cluster size.

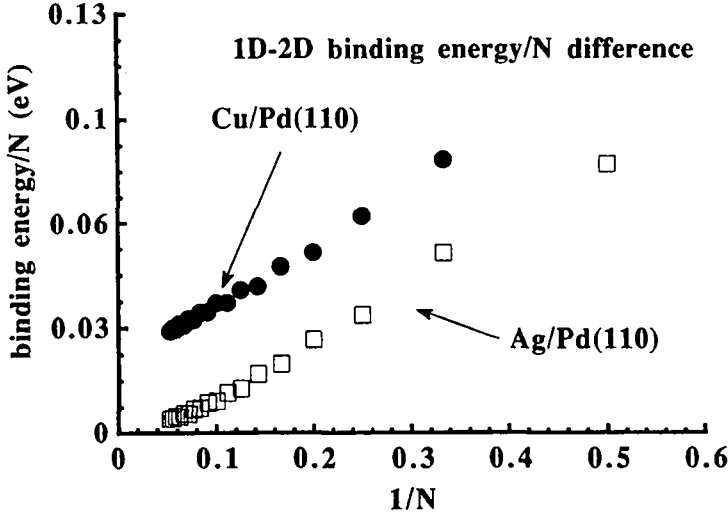


Fig.5.6: Difference in binding energy per atom between one- and twodimensional Cu and Ag islands as a function of the island size (N : island size in atoms, from [Mas93]). Whereas for Cu on Pd(110) the linear chain remains the stable island modification for $N \rightarrow \infty$, Ag chains on Pd(110) are only stable to about $N=25$.

$E_{F,2}$ turns out to be attractive and predominant for a pair of Cu adatoms in the nearest neighbour positions along $\{1\bar{1}0\}$ ($E_{F,2}=-0.244\text{eV}$), repulsive when two atoms are in second ($E_{F,2}=0.019\text{eV}$) and third ($E_{F,2}=0.038\text{eV}$) nearest neighbour positions and again attractive in the fourth ($E_{F,2}=-0.013\text{eV}$). The second and third configurations, however, exist only in the 2D structure, whereas the fourth ones are common to both arrangements but more numerous in the 1D structure. This has the effect of stabilizing the linear chain by as much as $\approx 1\text{eV}$ for $N=20$, a value that reduces to the calculated difference $\Delta E_{B,N} \approx 0.5\text{eV}$ when three and four body contributions are included. Structural relaxations are found to be crucial in establishing the tendency of structural stability.

However the correspondence between the $T=0\text{K}$ equilibrium structure and the ob-

served kinetic island growth shape at low temperatures is coincidental. Even if thermodynamics preferred 2D structures (this is for example the case for Ag on Pd(110), see figure 5.6), one might expect that the frozen cross-channel diffusion at low temperatures would lead to aggregation of 1D chains. Thus it can not be concluded from the experiment whether the linear Cu chains on Pd(110) are real equilibrium structures at $T \leq 300\text{K}$.

Concerning the diffusion properties of Cu on Pd(110) in the EAM calculation, simple hopping of the Cu adatom in the $[1\bar{1}0]$ and $[001]$ directions is characterized by barriers $E_{D,L}=0.32\text{eV}$ and $E_{D,T}=1.25\text{eV}$ and gives rise to an unrealistically large diffusion anisotropy, when compared to the experimental results. It is however known that more moderate differences (0.1eV to 0.2eV) between the two diffusion barriers are found upon inclusion of a cross exchange mechanisms in the $\{001\}$ direction [Liu91]. Here, the adsorbed Cu atom replaces a Pd atom in the first substrate layer leaving the Pd atom on top of the neighbouring $[1\bar{1}0]$ row (fig.5.7a,b). This process is characterized by an energy barrier $E_D(a \rightarrow b)=0.57\text{eV}$. Obviously such a mechanism produces CuPd surface alloying followed by self diffusion of the substrate atom rather than transverse diffusion of the heteroatom. As will be outlined in chapter 6.3 by CO adsorption studies, there is no evidence for CuPd intermixing at deposition temperatures below 700K. It is clear from fig.5.7 that a Pd atom on top of the first substrate layer in the vicinity of an incorporated Cu atom (situation in fig.5.7b) is energetically disfavoured by 0.15eV compared to the initial situation. So a more elaborated transverse diffusion mechanism is required to explain the experimental data.

According to Fig.5.7c-e, it has to be ensured that the original Cu adatom has to move across the close-packed rows, leaving the Pd substrate unchanged. This can be triggered by an exchange between two Pd atoms along the $[1\bar{1}2]$ direction leading to the configuration c), the energy barrier for this exchange being also equal

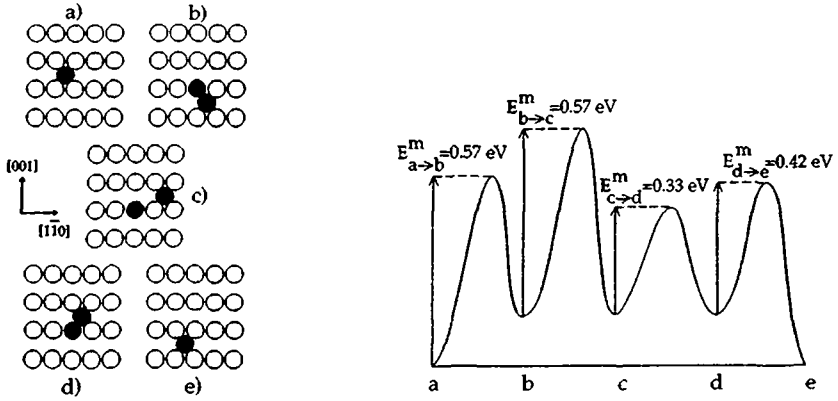


Fig.5.7: Left hand side: Suggested detailed mechanism for the migration of a Cu adatom along the [001] direction. Open circles: Pd atoms in the uppermost layer. Grey circles: Pd atom moved up to occupy an adsorption site. Dark circles: Cu adatom.

Right hand side: energy profile corresponding to the elementary diffusion steps displayed on the left hand side. E_m 's are the migration barriers.

to $E_D(b \rightarrow c) = 0.57 \text{ eV}$. This may be followed by a simple hopping of the Pd adatom along $[1\bar{1}0]$, which costs $E_D(c \rightarrow d) = 0.33 \text{ eV}$. Finally, a further PdCu exchange with $E_D(d \rightarrow e) = 0.42 \text{ eV}$ permits a migration of the Cu atom along the [001] direction (the final exchange can also occur between the Cu atom and another Pd adatom moving accidentally along a channel, without the intermediate step ($c \rightarrow d$)). The described combination is the most effective way to allow Cu diffusion along the transverse direction, as opposed to any mechanism requiring vacancy creation in the substrate, characterized by barriers as large as 0.9 eV . The above mechanism results also in a moderate diffusion anisotropy ($E_{D,T} - E_{D,L} = 0.25 \text{ eV}$), in full agreement with the experiment (0.24 eV).

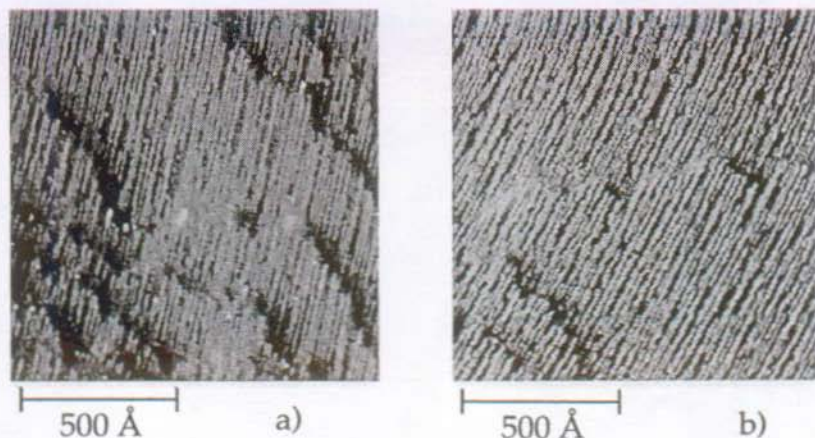


Fig.5.8: STM images of Cu submonolayer islands deposited at 270 K. Image sizes $1200 \text{ \AA} \times 1200 \text{ \AA}$. a) $\Theta_{\text{Cu}}=0.2$, b) $\Theta_{\text{Cu}}=0.5$

5.4 The growth of thin Cu films on Pd(110)

In the following chapter, STM investigations of the growth of thin Cu films ($\Theta_{\text{Cu}} \leq 10 \text{ ML}$) in the temperature range $270 \text{ K} \leq T_S \leq 600 \text{ K}$ will be presented [Hah94,3]. Copper was deposited at a constant rate of 10^{-3} monolayers per second. The deposition rate was calibrated by measuring the fraction of large substrate terraces which is covered by Cu islands upon submonolayer deposition at room temperature. Based on the accuracy and reproducibility of the deposition rate, all coverages in chapters 5 and 6 are exact to within $\pm 5\%$. The Cu layers were imaged at the same temperature where they were previously deposited, only films grown at $T_S=600 \text{ K}$ were quenched to room temperature before imaging.

5.4.1 $T_S \leq 350 \text{ K}$

As outlined in the previous chapter, Cu diffusion along the $[001]$ direction is completely frozen in below room temperature. At submonolayer coverages, exclusively

monatomic Cu chains oriented along $[1\bar{1}0]$ are formed. When the Cu coverage increases, the substrate "channels" are gradually filled and directly neighbouring Cu chains start to form two-dimensional islands (fig.5.8). Fig.5.9 displays a series of images characterizing the growth of Cu on the Pd(110) surface at $T_S=300\text{K}$. At this temperature and very low coverages (fig.5.9a), the majority of the islands is still monatomic in width and reaches lengths of hundreds of Å. With increasing coverage, however, the slow diffusion across the close packed Pd rows contributes to the island growth process. This is demonstrated in fig.5.9b, where at a coverage of $\Theta_{Cu}=0.35$ the Cu islands have an average width of 19Å , corresponding to about 5 close packed Cu rows. The islands are locked into a (1×1) structure on the substrate as indicated by a sharp (1×1) -LEED pattern without any additional spots and the flat imaging of the islands by STM. As suggested by the "icicles" growing outward from those substrate steps which run along the $[001]$ direction, defects on the Pd substrate act as centers for the nucleation of Cu islands. Inspection of fig.5.9b (or fig.5.3a) reveals that Cu "fingers" growing at step edges are found mostly at that kind of sites where a Cu island in the corresponding $[1\bar{1}0]$ substrate row is missing. This is due to the quasi one-dimensional diffusion properties of the system in this temperature range: a Cu atom landing on the surface moves along a $[1\bar{1}0]$ substrate row until it reaches a existing island. If the atom does not encounter an island in this substrate row, it will stick to the corresponding perpendicular step edge.

Increasing the coverage further to $\Theta_{Cu}=0.7$ (fig.5.9c), the gaps between the Cu islands are filled up, resulting in a growth of island widths (about 40Å in average) but also the onset of coalescence. At this coverage second layer nucleation is observed on top of the first layer Cu islands for the first time. The nucleation density in the second layer is much higher than on the Pd substrate (fig.5.9d) and the diffusion anisotropy is less marked, as is obvious by comparing the figs.5.9a and d. However, the second layer Cu islands are still exclusively oriented along $[1\bar{1}0]$. At temperatures

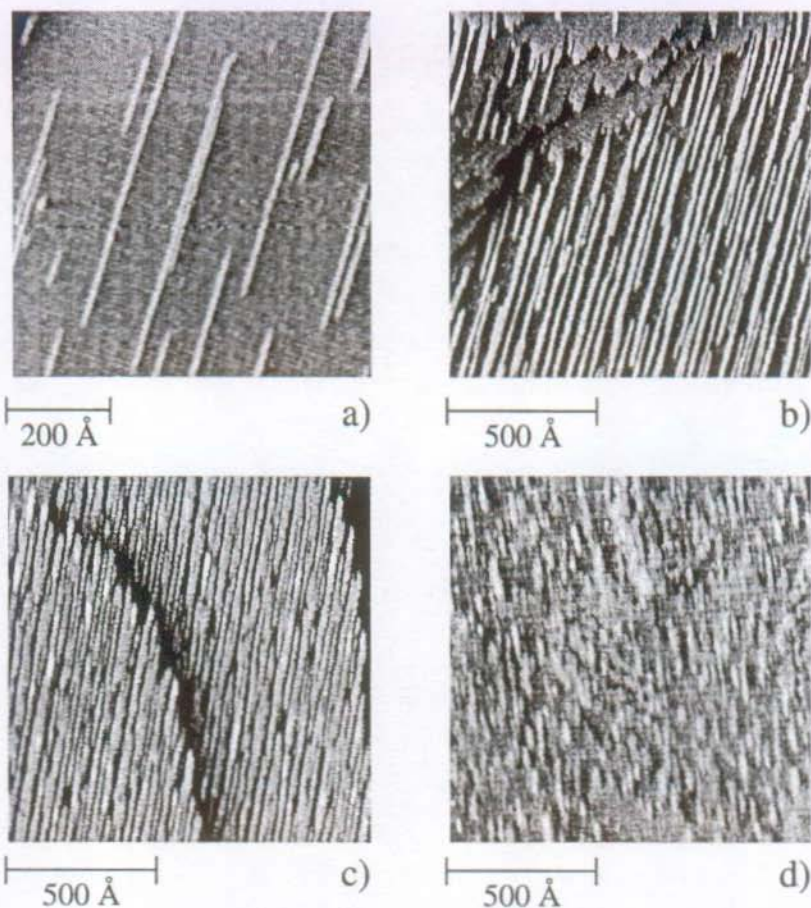


Fig.5.9: Cu growth on Pd(110) at $T_S=300$ K. All images span the size $1200 \text{ Å} \times 1200 \text{ Å}$, except for a) (size $670 \text{ Å} \times 670 \text{ Å}$). Coverages: a) $\Theta_{Cu}=0.05$ b) $\Theta_{Cu}=0.35$ c) $\Theta_{Cu}=0.7$ d) $\Theta_{Cu}=1.2$.

below about 350 K, thicker Cu layers appear rough and grainy, consisting of small Cu clusters of some ten Å in diameter.

By visual inspection of fig.5.9, a surprising detail attracts attention. While the

monatomic Cu chains at very low coverages appear as randomly distributed, two-dimensional Cu islands at intermediate submonolayer coverages appear to be arranged in an at least semiordered striped domain structure, a part of the islands shows a completely regular structure (lower part of fig.5.9b). To analyse the apparent mesoscopic order on a more quantitative level, histograms of the island distances along the [001] direction were evaluated. For a given Cu island, the distances to the first, second, third and all other neighbouring islands in the [001] direction have been measured. The data of 250 individual [001] line scans taken from 10 STM images have been compiled and are shown in histograms in fig.5.10 for coverages of $\Theta_{Cu}=0.07$ (a) and $\Theta_{Cu}=0.35$ (b). These histograms can be understood as one-dimensional island-island correlation functions. The distribution for the 1D Cu chains (fig.5.10a) shows indeed the absence of any long-range order, since all island-island distances are present with nearly equal probability (the scatter in the data is due to statistics). Only at the lowest distances ($\leq 20\text{\AA}$) a drop of the occurrence probability is noticed. This might be attributed to repulsive island-island interactions, giving rise to a depleted zone of some \AA around a Cu chain. The distance distribution of the two-dimensional islands at a coverage of $\Theta_{Cu}=0.35$, however, clearly reveals the presence of some long-range order. Distinct maxima at island separations of 40\AA , 80\AA and 120\AA are present. These values are multiples of the average island separation at this coverage (40\AA), showing an enhanced probability to find neighbouring islands at these particular positions. The loss of order with increasing distance from a given island strongly resembles the typical behaviour for glasses or liquids.

Mesoscopic domain ordering was previously observed on Si(100) [Men88], on clean Pd(110) [Hör93], on Au(111) [Bar90,2] and in the system Cu(110):O [Ker91]. The physical origins for these ordering phenomena are believed to be surface stress effects and/or electrostatic interactions in the latter case [Van93].

In the Cu/Pd(110) case, the Cu islands are considerably strained with respect to

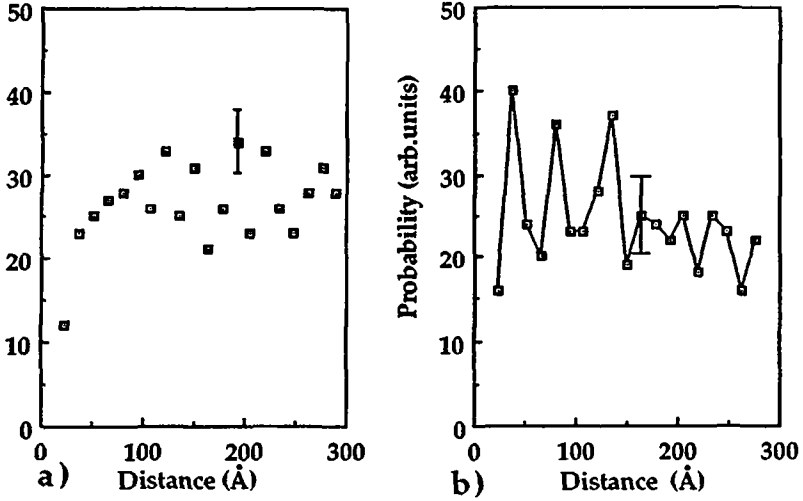


Fig.5.10: Histograms of island-island separations on Pd(110) along the [001] direction upon deposition of a) 0.07ML Cu, b) 0.35ML Cu at $T_S=300$ K.

the Cu bulk due to the 7% lattice mismatch between copper and palladium, keeping in mind that the Cu islands are locked into a (1×1) -structure on Pd(110). The strained Cu islands exert a force on the substrate which lowers the island energy at the expense of stress in the substrate. Assuming a mixed uniaxial phase of alternating stripes of Cu covered (coverage Θ and width L_A) and Cu free domains (coverage $1 - \Theta$ and width L_B), the energy per unit area of the domain structure is

$$\Delta E = \Theta \Delta E_O + \frac{F_S}{L} - \frac{C}{L} \ln \left(\frac{L}{\pi a} \sin(\pi \Theta) \right) \quad (5.11)$$

[Van93, Mar92]. Here $\Delta E_O = E_B - E_A$ is the difference of the surface energies of the phases A and B. $L = (L_A + L_B)/2$ is the average domain width, a is the lattice constant, F_S is the free energy of a Cu/Pd(110) step per unit length and C is a constant determined by the elastic properties and the difference of the surface stress

within the two domain types. It can be shown that for $|\Delta E_O| < C/(a \exp(F_S/C + 1))$, a periodic domain structure is favoured. The equilibrium periodicity of this ordered striped domain phase is obtained by minimizing ΔE at constant coverage Θ :

$$D = \pi a \csc(\pi\Theta) \exp\left(\frac{F_S}{C} + 1\right) \quad (5.12)$$

Recently it has been shown [Zep93] that there should exist a firm relation between this domain periodicity D at intermediate coverages Θ and the width of a single island at low island concentration ($L_O = L_A(\Theta \rightarrow 0)$), independent of the actual system (e.g. the constants F_S , C and a). This size ratio should be in the interval $1/4 < L_O/D < 1/3$.

At a first glance, this value is not consistent with the Cu/Pd(110) case. In the limit $\Theta \rightarrow 0$ the Cu islands are monatomic in width (i.e. $L_O = 2.57 \text{ \AA}$) while the average separation at medium coverages ($\Theta = 0.35$) is $D = 40 \text{ \AA}$, giving rise to a size ratio of $1/16$. However, at this coverage no ordering of the Cu chains occurs. As already mentioned, an ordered domain formation is preferred only above a critical coverage. For the present system this critical coverage is somewhere between $0.15 \text{ ML} < \Theta_{Cu} < 0.25 \text{ ML}$. At $\Theta_{Cu} = 0.2 \text{ ML}$ the average island width is 11 \AA . If we use this value as a width of a single island in the limit of small coverage, the resulting L_O/D ratio becomes 0.28 , which is within the predicted size ratio interval.

However, equations (5.11) and (5.12) are strongly valid only for fully equilibrated systems. It has been shown in chapter 5.3 that, at $T_S = 300 \text{ K}$, the shape of the Cu islands on Pd(110) is due to kinetic limitations. Thus it is not excluded that there exist kinetic pathways leading to the observed ordered structure during growth. In fact it has recently been shown by Wheeler et al. [Whe92] that during heteroepitaxial growth on a vicinal surface, for instance, a disordered step array can transform into an equally spaced step configuration if the growth velocity is chosen suitably.

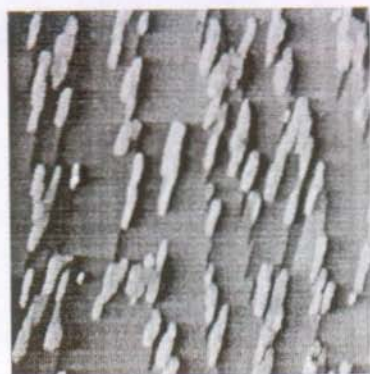
5.4.2 $350\text{K} < T_S \leq 500\text{K}$

Fig.5.11 displays the growth of Cu on Pd(110) at $T_S=400\text{K}$. At this temperature, most of the deposited submonolayer Cu diffuses to substrate step edges ($\Lambda_A > \Lambda_T$), as indicated by the "fingers" growing outward from steps. As a result, Cu wets the substrate in a pure step flow mode on narrow terraces. Isolated islands are formed only on very large terraces (fig.5.11a). The islands are elongated along the $[1\bar{1}0]$ direction of easy diffusion. Since Cu and Pd atoms situated in the same layer can not be distinguished by STM (no height difference in the images), it is difficult to determine the exact coverage where second layer islands begin to nucleate. From comparison with RAIRS measurements of CO on Cu/Pd(110) (see next chapter) it can however be concluded that the first layer is filled up to about $\Theta_{Cu}=0.9$ before second layer nucleation starts (fig.5.11b). Fig.5.11c shows that at this temperature Cu film growth proceeds via the Stranski-Krastanov mode. On the complete first monolayer, three-dimensional Cu clusters develop, their edges being accurately oriented along the high symmetry directions of the substrate. For an ideal three-dimensional film growth, it is necessary that atoms aggregate at the same level on which they land. Then the visible fraction A_n of the layer n follows a poisson law $A_n = (\Theta^n/n!) \exp(-\Theta)$, where Θ is the total coverage [Cha93]. For $\Theta_{Cu}=2.3$ fig.5.11d shows the corresponding Poisson law (with $\Theta=1.3$, since threedimensional growth begins after the completion of the first monolayer) and the data taken from the STM images. The experimental curve resembles the Poisson law, however interlayer mass transport can not be excluded from these data.

Fig.5.11b shows that isolated second layer islands do not nucleate homogeneously, but almost exclusively at definite positions: on the *upper* part of step edges. This phenomenon is elucidated in fig.5.12 at a coverage of $\Theta_{Cu}=1.2\text{ML}$. The dependence of the local surface morphology on the substrate step orientation is shown. In fig.5.12a, the steps are smooth and oriented parallel to the preferential growth direction of the



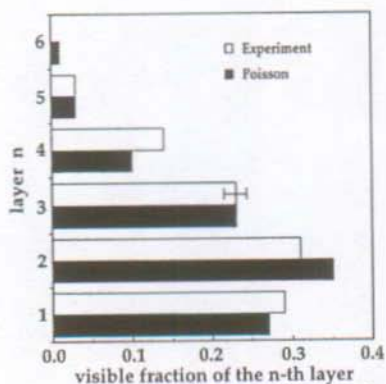
a)



b)



c)



d)

Fig.5.11: STM images showing Cu growth at $T_S=400\text{K}$. All images span the size $2100\text{\AA} \times 2100\text{\AA}$. a) $\Theta_{Cu}=0.45$ b) $\Theta_{Cu}=1.2$ c) $\Theta_{Cu}=2.3$

d) Histogram showing the visible fraction of the n-th layer in image c) and the corresponding Poisson law corresponding to an ideal three-dimensional Cu growth from the 2nd layer on.

Cu islands, $[1\bar{1}0]$. In fig.5.12 b(c), the steps deviate by 40° (b) and nearly 90° (c),

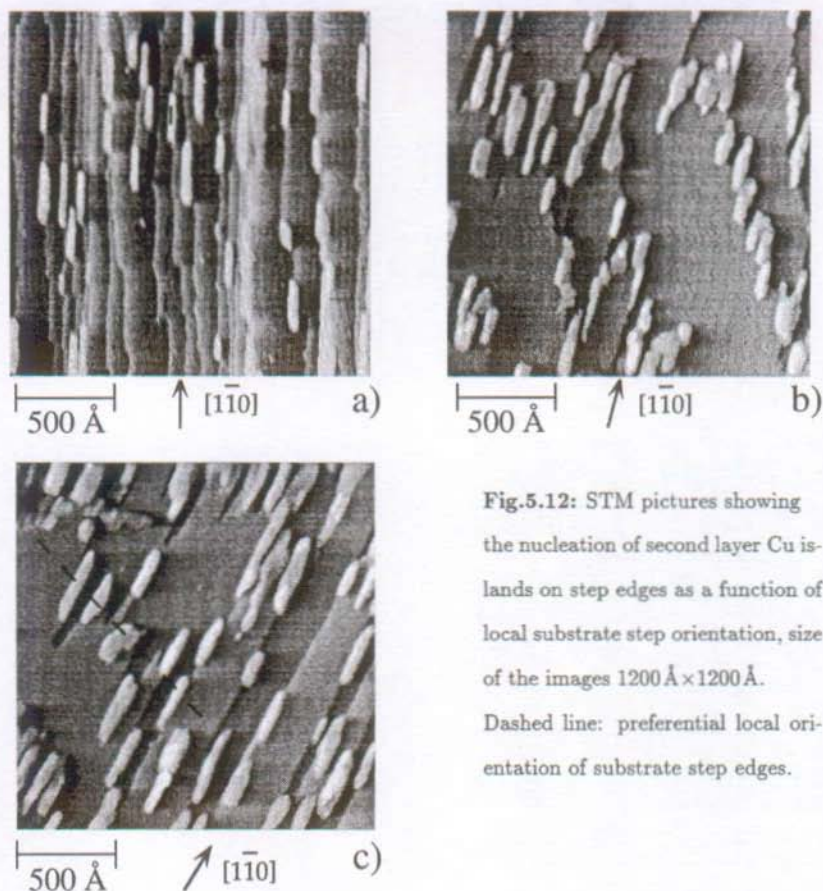


Fig.5.12: STM pictures showing the nucleation of second layer Cu islands on step edges as a function of local substrate step orientation, size of the images $1200 \text{ \AA} \times 1200 \text{ \AA}$.
Dashed line: preferential local orientation of substrate step edges.

respectively, from $[1\bar{1}0]$. With increasing deviation of the substrate step orientation from $[1\bar{1}0]$, the nucleation density in the second Cu layer increases. This is not surprising if we assume that also second layer Cu atoms move most easily along $[1\bar{1}0]$. According to the high diffusion length Λ_A at $T_S=400\text{K}$, islands will then nucleate preferentially on $[001]$ step edges. This argument holds also for fig.5.12a: almost exclusively kinks act as nucleation centers, if $[001]$ -steps are not available. To enable

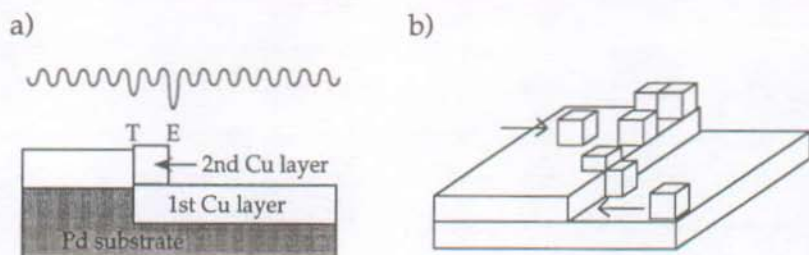


Fig.5.13: Two models for the preferential nucleation of Cu islands at descending step edges:

- a) Existence of a potential minimum near descending step edges.
- b) Interlayer exchange mechanism.

preferential second layer island formation on descending step edges, is it necessary that the adatom density and therefore the nucleation rate is enhanced in the vicinity of step edges. The following models may account for this.

The energy barrier for a downward motion of a Cu adatom from a Cu island onto the Pd substrate can easily be overcome, as the completion of the first monolayer demonstrates. On the other hand, the Cu-Cu step potential may be different, hindering the descent of Cu atoms onto lower Cu terraces. In this case the diffusing upper terrace adatoms hitting a descending step are (at least partially) reflected at the step edge. This leads to a higher adatom density near the step edge and thus to an increasing nucleation rate in the vicinity of descending step edges. But this does not explain why islands nucleate nearly exclusively in this regions. Herefore it must be assumed that besides the usual deep potential minimum at the ascending step edge, there exists a second minimum near the descending step edge, representing an attractive sink for adatoms. Such minima have indeed been observed in several

systems:

- * The deposition of Ir atoms on an Ir(111) surface with a central iridium cluster on it has been studied by field ion microscopy [Wan93,1]. A depleted zone, two atoms wide, around the cluster has been found due to trapping of adatoms by the ascending step edge. Additionally, the average number of adatoms condensed at sites close to the cluster edge was twice as high as in the interior - close to the descending step edge, adatoms are thus bound in deeper wells than in the central regions of the cluster.

- * At Cu coverages slightly above $\Theta_{Cu}=1$, the ascending step edge E is coated by a thin seam of second layer Cu (fig.5.13a), since film growth proceeds partially by step-flow starting from the ascending step edge. This might modify the potential for upper terrace adatoms at the transition line T between upper terrace and lower terrace Cu condensed at the step. This line can act as a sink for diffusing adatoms and enhance the possibility for nucleation along this line. The modified potential may for instance be due to a Cu-Cu layer distance slightly different from the Pd bulk interlayer spacing (although not seen in the STM images). Such a phenomenon was indeed observed for Au/Ru(0001) even for fourth layer island nucleation [Gün93].

A completely different model which seems courageous at first glance is the following (fig.5.13b). A Cu atom arriving at a [001] step edge is incorporated into it and pushes an edge atom onto the upper terrace. Such interlayer exchange mechanisms were also observed by Landman et al. [Lan93]. Three-dimensional clusters are transformed into two-dimensional islands (upon thermal annealing) by mechanisms leaving the uppermost atoms of the cluster in the center of the 2D island and not at the perimeter as one would expect naively. Model b) is simply the reverse process. If such an exchange mechanism is more time-consuming than a simple hop, the probability of island nucleation on step edges is enhanced.

Both models must explain why this special nucleation phenomenon is not observed at lower or higher substrate temperatures. At low T_S second layer adatom mobility

is low, the nucleation density is very high, preferential nucleation at descending step edges is not conspicuous. In addition, the energy barrier for the described exchange process can not be overcome. At high T_S , adatoms can easily leave the potential well at the transition line. Diffusion is fast and the growth proceeds via pure step flow starting from the ascending step edges.

5.4.3 $T_S > 500\text{K}$

At about $T_S=600\text{K}$, a transition to a twodimensional layer-by-layer growth occurs (fig.5.14). In the submonolayer range, Cu wets the substrate in a pure step-flow mode. Nucleation of Cu islands was never observed at this temperature, even on the largest terraces. As evidenced by a sharp (1×1) LEED pattern and the flat imaging by STM, the first Cu layers grow pseudomorphically on Pd(110). From a thermodynamic point of view, the formation of thick pseudomorphic Cu films is unfavourable since the strain energy in the film which arises from large lattice misfit of 7% between bulk Cu and Pd increases with the film thickness. However this strain is partially released by uniaxial compression of the film surface along the $[1\bar{1}0]$ direction from the 6th Cu layer on.

This compression is present in the STM images as a striped pattern with the stripes running along $[001]$ (figs.5.14c). The pattern corresponds to a buckling with a periodicity of $79 \pm 1 \text{ \AA}$. The height variation from light to dark stripes is about 0.5 \AA . The reconstruction persists up to the highest coverages studied ($\Theta_{Cu}=10\text{ML}$) without any measurable change of the periodicity or of the height modulation. By LEED, the reconstruction was not detectable due to the low resolution of our instrument. From the absence of any additional LEED spots and from the STM images it can however be concluded that the Cu atoms are still locked into their positions between the close packed atom rows of the underlying layer, but try to minimize surface stress by reducing the interatomic distances along $[1\bar{1}0]$.



500 Å

a)



500 Å

b)



500 Å

c)

Fig.5.14: Thin Cu film growth on Pd(110) at $T_S=600\text{K}$, size of all images $2400\text{Å}\times 2400\text{Å}$. a) $\Theta_{Cu}=1.1$ b) $\Theta_{Cu}=2.3$ c) $\Theta_{Cu}=10\text{ML}$.

Fig.5.15 shows a possible real space model of the reconstructed surface. From the observed periodicity of 79Å it can be calculated that the interatomic distance in the $[1\bar{1}0]$ direction is reduced to 2.66Å . Thus from the 6th layer on, 30 Cu atoms would be situated onto 29 atoms of the unreconstructed 5th layer. Regions where Cu atoms occupy near bridge sites alternate with regions where atoms rest in near fourfold hollow sites. This explains the buckling of the surface, which is still observed for thicker

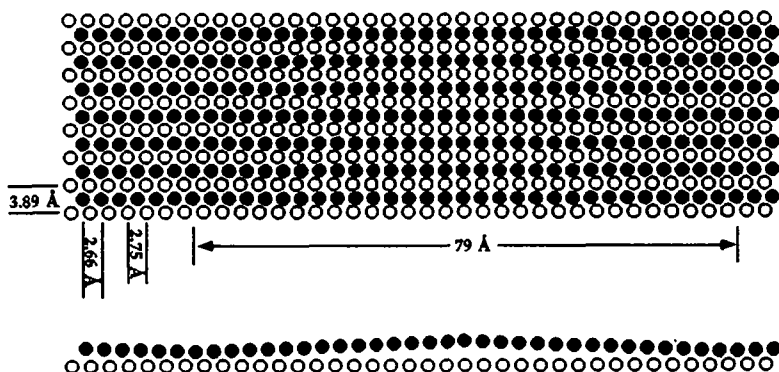


Fig.5.15: Model of the uniaxial compression of thicker Cu layers ($\Theta_{Cu} \geq 5\text{ML}$). The positions of 6th layer atoms (full circles) with respect to the unreconstructed 5th layer (open circles) are shown. a) top view b) side view

layers growing epitaxially on the first reconstructed layer. Obviously, maximum stress release can not be achieved by adopting the Cu bulk value of $3.61/\sqrt{2} = 2.55\text{\AA}$. This may be due to the rigid atom positions in the perpendicular direction, energetically preventing a further compression. A structure model must also take into account that the system will try to minimize the occupation of energetically unfavourized bridge sites. So the proposed model which assumes equal distances between the Cu atoms, has to be modified. In reality, more Cu atoms will be locked into fourfold hollow sites, whereas the atom density will be lower in the bridging regions. Finally it is noted that an increase of the dislocation density with the film thickness is observed. Both effects, the uniaxial compression and the dislocation formation contribute to the lowering of stress in the Cu film, thus layerwise growth can continue up to the 11th layer at least.

As revealed by CO adsorption studies, at temperatures above 600K CuPd intermixing occurs. This temperature region will be examined in chapter 6.4.

6. CO chemisorption on Cu/Pd(110)

6.1 Introduction

The study of the electronic and chemical properties of supported Cu layers on metal substrates is an area of active research. This interest partially originates from the fact that Cu appears as a component of several bimetallic catalysts dispersed over high-surface area supports. Such mixed-metal catalysts are superior to their single-metal counterparts in terms of chemical activity, selectivity and stability [Sin83]. The origin of these superior properties is not well understood, but generally discussed in terms of "ensemble" and "ligand" effects [Rod91]. The "ensemble" effect is a geometric argument based on the fact that a given reaction needs a certain number of surface atoms to occur. "Ligand" effects relate to electronic modifications of the active component by the nonactive metal, which may result in an enhanced activity of the mixed system. Among the numerous catalytical active bimetallic systems, Cu-Pd is a promising candidate: supported Cu-Pd particles have shown an enhanced catalytic activity in the oxidation of CO to CO₂ compared to the single metal surfaces [Cho91].

The chemisorption of CO is frequently used as a tool to characterize structural, electronic and chemical properties of bimetallic model systems. RAIRS studies of CO on Cu/Rh(100) [Kuh90, He 91], Cu/Ru(001) [Hof87,1] and Cu/Pt(111) [Rod92] and EELS studies of CO on Cu/Ni(111) [Gar89, Fen89] were reported. The classical techniques AES, LEED and TDS were used to investigate CO adsorption on Cu/Re(0001) and Cu/Mo(110) [He 90], on Cu/Pd(111) [Ora90] and Cu/Rh(111) [For85]. Later, the general tendencies arising from these studies will be compared to CO adsorption properties on Cu/Pd(110) and Cu/Pd(100). In contrast to the use of CO molecules as probes for the investigation of unknown surface structures, this work represents a different approach. CO is adsorbed on various Cu/Pd surfaces with well known morphologies previously characterized by STM. Therefore the CO vibrational properties

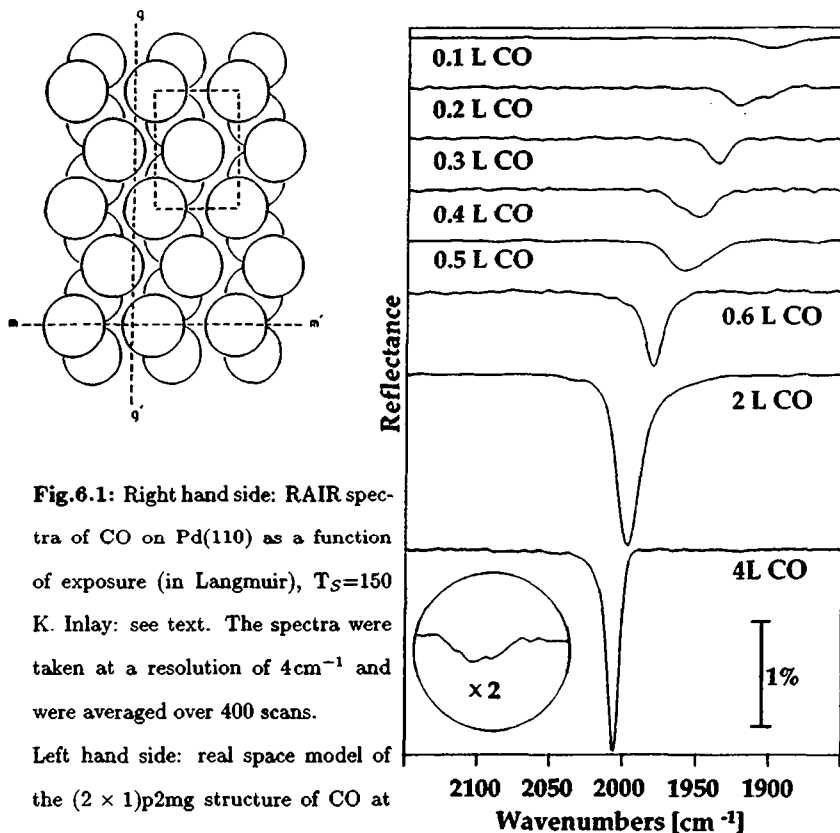


Fig.6.1: Right hand side: RAIR spectra of CO on Pd(110) as a function of exposure (in Langmuir), $T_S=150$ K. Inlay: see text. The spectra were taken at a resolution of 4cm^{-1} and were averaged over 400 scans.

Left hand side: real space model of the $(2 \times 1)p2mg$ structure of CO at saturation coverage $\Theta_{CO}=1$ (from [Che85]).

as a function of the Cu/Pd composition can be directly related to the STM work. However it will be outlined that CO adsorption studies provide valuable additional information on the substrate morphology, especially concerning the distribution of Cu and Pd in the same layer, since the two elements are undistinguishable in STM images [Hah94,1].

The IR spectra of CO adsorbed on clean Pd(110) at $T_S=150\text{K}$ as a function of

coverage are shown in fig.6.1. Initial adsorption leads to the formation of an infrared absorption band at 1900cm^{-1} . With increasing exposure it splits up in a doublet (1915cm^{-1} and 1902cm^{-1}). The low frequency band disappears upon exposure of 0.3 L, whereas the high frequency component shifts to 1935cm^{-1} . After an intermediate stage associated with the appearance of several bands in the region $1950\text{-}1990\text{cm}^{-1}$, a broad band at 1996cm^{-1} remains after 2L CO-exposure. The peak maximum shifts to 2007cm^{-1} , the linewidth decreases from 15cm^{-1} to 8cm^{-1} at saturation coverage. Previous studies [Rav89, Che85] investigated the adsorption of CO on Pd(110) in more detail by EELS, RAIRS and LEED. The IR spectra at low coverage are explained in terms of CO islands surrounded by a disordered "sea" as a result of low mobility at $T_S=150\text{K}$. With increasing exposure, domains with different local CO coverages from 0.5 to 1 are formed. The subsequent observation of a single peak spectrum indicates that all local domain coverages approach unity. Non-uniform domain sizes are revealed by the large peak halfwidth. Before saturation, the domains increase in size and ordering of the CO adlayer occurs to give a $(2 \times 1)\text{p}2\text{mg}$ LEED-pattern. This final structure was interpreted as CO molecules on twofold bridge sites which tilt alternately to the side in order to minimize steric repulsions (fig.6.1b).

The assignment of the band at 2007cm^{-1} is a matter of controversy, since the frequency lies in the "gray area" midway between typical values for bridge and top bonded species (see chapter 2.2.3). A recent TLEED study [Wan93,2] re-assigned the adsorbate to the top site, the CO molecule being tilted by 11° with respect to the surface normal. This interpretation is however in contradiction with other vibrational spectroscopy observations: upon direct exposure of the crystal to 10^{-7}mbar CO at 140K , a second, higher frequency band at 2095cm^{-1} develops (see inlay in fig.6.1). This was attributed to a "fast" compression due to adlayer immobility at low temperatures which results in the formation of small $(2 \times 1)\text{p}1\text{g}1$ islands with top-bound CO molecules at the domain boundaries, giving rise to the 2095cm^{-1} band [Rav89,

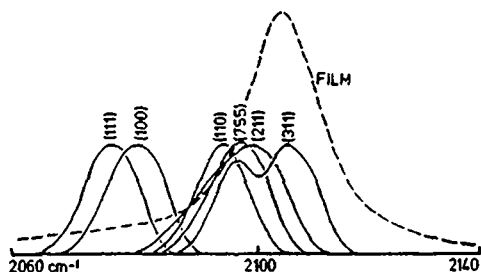


Fig.6.2: CO infrared spectra at saturation coverage on various Cu single crystal surfaces and on a Cu film (from [Pri78]).

Che85]. CO on Pd(100) shows a similar behaviour (see chapter 7.3 and [Bra78]). On Pd(111), three absorption bands develop depending on CO coverage and temperature, at 1895cm^{-1} , 1962cm^{-1} and 2110cm^{-1} , indicating the subsequent population of threefold hollow, twofold bridge and top sites [Kuh92,2; Guo89]. In addition, CO adsorption on thin Pd films deposited on metallic substrates results in high frequency ($>2100\text{cm}^{-1}$) absorption bands attributed to top-site species [Sel93]. To give a consistent interpretation, the CO/Pd(110) absorption band at 2007cm^{-1} must thus rather be assigned to bridge bonded CO, since the CO vibrational frequency increases when the coordination number decreases (see chapter 2.2.3). Further evidence for the correctness of the bridge-assignment of the 2007cm^{-1} band is provided by the analysis of CuPd intermixing experiments discussed in chapter 6.4. Keeping in mind this controversy, I will further refer to this band as the "bridge species".

Finally I note that upon adsorption at $T_S > 250\text{K}$, CO induces a (1×2) missing-row reconstruction on Pd(110) [Hu 90, Gau92].

RAIR spectra for on-top site CO on a variety of copper single crystal surfaces are shown in fig.6.2 [Pri78]. The spectra show the dependence of the CO stretching frequency on substrate atom coordinations. On the Cu(110) surface, two different ordered phases of CO were reported [Har84], a (2×1) structure at $\Theta_{\text{CO}}=0.5$ and a diffuse $c(5/4 \times 2)$ compression structure at the saturation coverage ($\Theta_{\text{CO}}=0.8$).

Fig.6.3 (next page): (left hand side) STM images of Cu on Pd(110) deposited at 400 cm^{-1} (see chapter 5.4)

(right hand side) RAIR spectra of CO on Cu/Pd(110) as a function of Cu coverage. Cu was deposited at 400 cm^{-1} , the spectra were taken at 150K after exposure of 10 L CO during cooling the sample from 250K to 150K. Resolution 4 cm^{-1} .

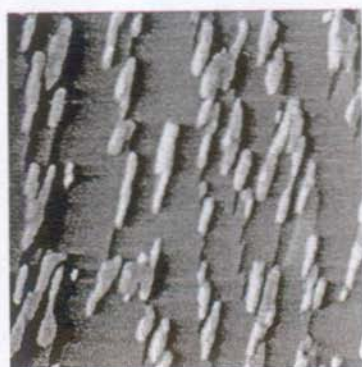
6.2 RAIRS studies of CO on Cu/Pd(110)

In fig.6.3 (left hand side) the growth mode of Cu on Pd(110) at $T_S=400$ K (Stranski-Krastanov growth with a critical thickness of one monolayer) is recalled. In the following, the changes in the Cu/Pd(110) surface morphology occurring with increasing Cu coverage will be directly related to the adsorption properties of CO on these surfaces. On the right hand side of fig.6.3 the infrared spectra of CO adsorbed on Cu/Pd(110) surfaces as a function of Θ_{Cu} are plotted. The indicated amount of copper was deposited at $T_S=400$ K. After recording the infrared background spectrum at $T_S=150$ K, the crystal was heated to 250K and exposed to 10^{-7} mbar CO upon recooling to 150K. The total exposure was 10L, ensuring saturation coverage. This procedure resulted in sharper infrared peaks, thus better ordered CO layers than upon direct exposure at 150K.

All RAIR spectra shown were recorded at a resolution of 4 cm^{-1} , averaged over 800 scans and are corrected for the baseline. The IR spectrum of CO on clean Pd(110) is displayed again for reference. At $\Theta_{Cu}=0.15$ a new, broad CO absorption feature centered around 2100 cm^{-1} appears. With increasing copper coverage it develops into two distinct bands at 2147 cm^{-1} (FWHM 25 cm^{-1}) and 2091 cm^{-1} (FWHM 32 cm^{-1}). The high frequency band has maximum intensity at $\Theta_{Cu}=1.05$, where its peak maximum has shifted down to 2136 cm^{-1} and its linewidth is reduced to 15 cm^{-1} . The two lower frequency bands at 2091 cm^{-1} and 2000 cm^{-1} decrease continuously in intensity as well as in frequency and disappear slightly above $\Theta_{Cu}=1$. In the Cu



2.3 ML Cu

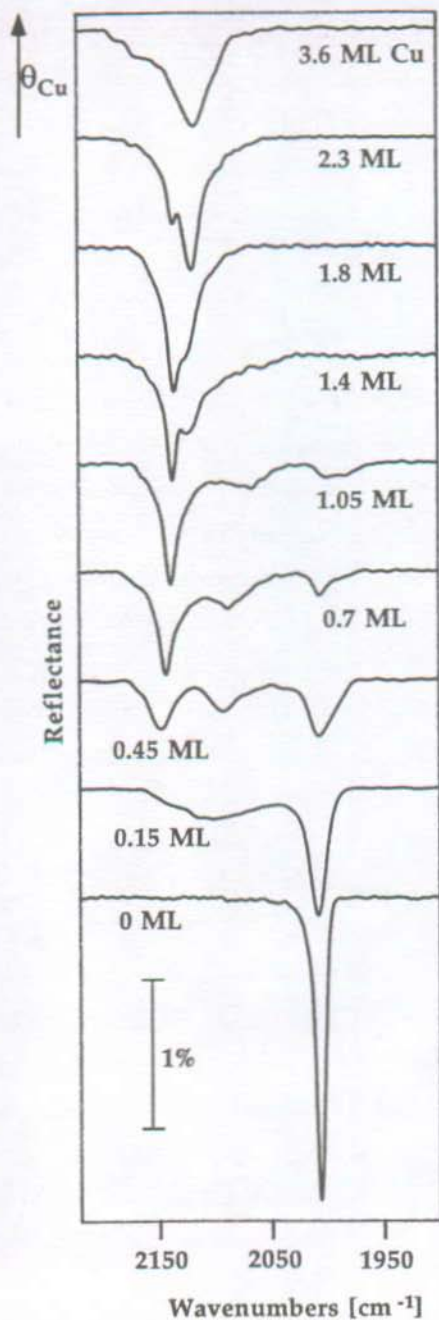


1.2 ML Cu



500Å

0.45 ML Cu



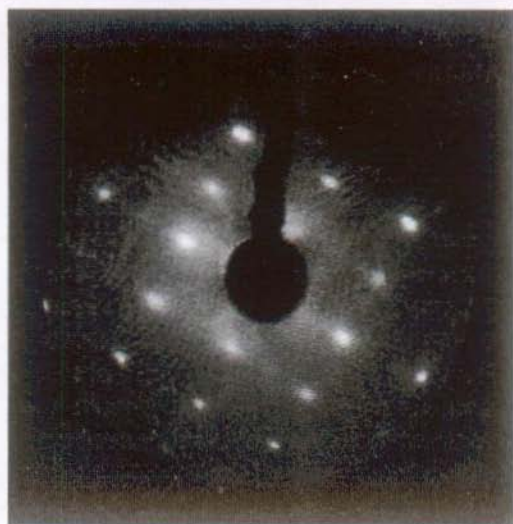


Fig.6.4: LEED pattern of the (2×1) structure of CO on Cu/Pd(110), $\Theta_{Cu}=1.0$ ML deposited at 400K. Electron energy 93eV.

multilayer range the absorption band at 2136cm^{-1} loses intensity without further frequency shift, whereas a new feature appears at 2120cm^{-1} (FWHM 25cm^{-1}) and is dominant above $\Theta_{Cu}=2$. At higher Cu coverages ($\Theta_{Cu}=3.6$), a broad band at 2110cm^{-1} remains. Its peak maximum shifts slowly towards typical values of CO on bulk Cu surfaces when the Cu coverage is increased furthermore. In fig.6.7 the relative intensities (normalized to the total CO infrared absorption) of the four absorption bands are displayed schematically as a function of Cu coverage.

By comparing STM and RAIRS data the assignment of the IR peaks to different CO adsorption sites can be done straightforward. The two high frequency bands, being the only ones present in the multilayer regime, correspond to CO molecules adsorbed on copper sites. The STM results suggest that CO adsorbed on the three-dimensional Cu clusters gives rise to the peak at 2120cm^{-1} whereas the band at 2136

cm^{-1} is associated with CO bound to Cu atoms in the first flat layer, both in on-top configuration. LEED measurements reveal that the CO molecules on the first flat Cu monolayer form an ordered (2×1) - structure (fig.6.4), giving rise to the sharp feature at 2136cm^{-1} . It is likely that this structure corresponds to the (2×1) -phase on Cu(110) at $\Theta_{\text{CO}} = 0.5$, however no CO compression structure like on bulk Cu(110) could be observed. On thicker 3D-Cu layers, no ordered LEED patterns (except (1×1)) appeared upon CO adsorption. The absorption band at $2091\text{-}2070\text{cm}^{-1}$ could be attributed both to CO/Cu species or to Pd-top site CO species (see chapter 6.1). But its disappearance at Cu coverages above $\Theta_{\text{Cu}}=1$ indicates that this band is due to CO on Pd substrate sites. Thus the population of the adsorption site, which gives rise to the small 2095cm^{-1} feature on the clean surface at high CO pressures, is dramatically increased in the presence of Cu islands.

Two observations confirm the assignment of this absorption peak to Pd top-site CO. Firstly, fig.6.5a shows the vibrational spectra of CO adsorbed on Cu/Pd(110) ($\Theta_{\text{Cu}}=0.45$) as a function of increasing CO coverage. The different Pd substrate sites are populated first whereas CO adsorbs on Cu sites only after higher exposure. The complex frequency behaviour of the band in the bridging region has been discussed in chapter 6.1. The peak maximum of the absorption band assigned to CO molecules on Cu sites exhibits only a very small (2cm^{-1}) coverage induced frequency shift. This behaviour is typical for CO/Cu systems [Woo82]. By contrast, the band assigned to CO bound on Pd top-sites undergoes a strong (28cm^{-1}) upward frequency shift, characteristic for CO adsorption on transition metals. The second indication concerns the CO desorption temperatures. Fig.6.5b shows vibrational spectra of 10L CO on Cu/Pd(110) ($\Theta_{\text{Cu}}=0.6$) adsorbed at $T_S=150\text{K}$, flashing to the indicated temperatures and recooled to 150K before spectra recording. Desorption of Cu-CO occurs at 230K , whereas the two lower frequency bands assigned to Pd sites disappear both only upon annealing at 350K . This indicates a strengthening of the bond between

cm^{-1} is associated with CO bound to Cu atoms in the first flat layer, both in on-top configuration. LEED measurements reveal that the CO molecules on the first flat Cu monolayer form an ordered (2×1) - structure (fig.6.4), giving rise to the sharp feature at 2136cm^{-1} . It is likely that this structure corresponds to the (2×1) -phase on Cu(110) at $\Theta_{\text{CO}} = 0.5$, however no CO compression structure like on bulk Cu(110) could be observed. On thicker 3D-Cu layers, no ordered LEED patterns (except (1×1)) appeared upon CO adsorption. The absorption band at $2091\text{-}2070\text{cm}^{-1}$ could be attributed both to CO/Cu species or to Pd-top site CO species (see chapter 6.1). But its disappearance at Cu coverages above $\Theta_{\text{Cu}}=1$ indicates that this band is due to CO on Pd substrate sites. Thus the population of the adsorption site, which gives rise to the small 2095cm^{-1} feature on the clean surface at high CO pressures, is dramatically increased in the presence of Cu islands.

Two observations confirm the assignment of this absorption peak to Pd top-site CO. Firstly, fig.6.5a shows the vibrational spectra of CO adsorbed on Cu/Pd(110) ($\Theta_{\text{Cu}}=0.45$) as a function of increasing CO coverage. The different Pd substrate sites are populated first whereas CO adsorbs on Cu sites only after higher exposure. The complex frequency behaviour of the band in the bridging region has been discussed in chapter 6.1. The peak maximum of the absorption band assigned to CO molecules on Cu sites exhibits only a very small (2cm^{-1}) coverage induced frequency shift. This behaviour is typical for CO/Cu systems [Woo82]. By contrast, the band assigned to CO bound on Pd top-sites undergoes a strong (28cm^{-1}) upward frequency shift, characteristic for CO adsorption on transition metals. The second indication concerns the CO desorption temperatures. Fig.6.5b shows vibrational spectra of 10L CO on Cu/Pd(110) ($\Theta_{\text{Cu}}=0.6$) adsorbed at $T_S=150\text{K}$, flashing to the indicated temperatures and recooled to 150K before spectra recording. Desorption of Cu-CO occurs at 230K , whereas the two lower frequency bands assigned to Pd sites disappear both only upon annealing at 350K . This indicates a strengthening of the bond between

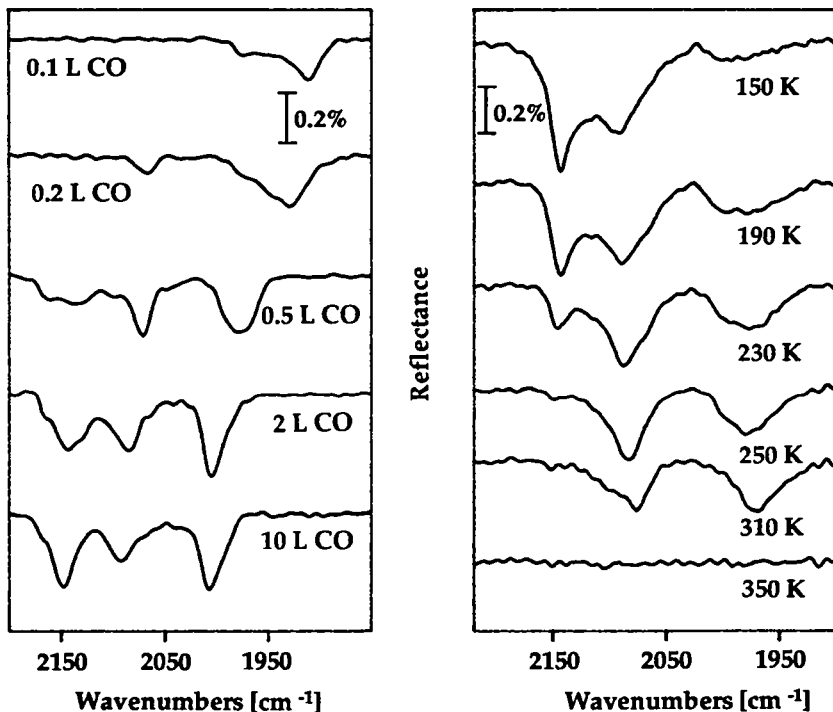


Fig.6.5: (a) RAIR spectra of CO on Cu/Pd(110) as a function of CO coverage. $\Theta_{Cu}=0.45$ ML deposited at 400 K. CO was adsorbed at 150 K. Resolution 4 cm^{-1} . (b) RAIR spectra of CO obtained after flashing the crystal to the indicated temperatures and recooling to 150 K. $\Theta_{Cu}=0.6$ ML deposited at 400 K. Resolution 4 cm^{-1} .

CO and supported Cu layers with respect to bulk Cu (CO desorbs from Cu(110) at 200 K [Har84]). On the other hand, upon submonolayer Cu deposition the Pd-CO bond is weakened. On clean Pd(110), the CO desorption temperature region extends to 500 K. These observations are indeed typical for noble metal layers deposited on transition metals [Hof87,1; Sch90].

Fig.6.6 (next page): (left hand side) RAIR spectra of CO on Cu/Pd(110) as a function of Cu coverage. Cu was deposited at 600K, the spectra were taken at 150K after exposure of 10L CO during cooling the sample from 250K to 150K. Resolution 4 cm^{-1} .
(right hand side) Identical measurements, Cu deposition temperature 300K.

It is impossible to explain both the increase in binding energy and the upward shift of the C-O stretching frequency with respect to bulk Cu surfaces within the same model. As outlined in chapter 2, chemisorption of CO on a metal surface generally results in a red shift of the CO vibrational frequency relative to the gas phase due to backdonation of electronic charge from the substrate into the antibonding CO $2\pi^*$ orbital. The observed C-O stretch frequency close to the gas phase value is probably due to a decrease of this backdonation as a result of charge transfer from Cu to the Pd substrate. The decrease in backdonation should be accompanied by a weakening of the CO-metal bond. However, exactly the opposite is observed. This is in fact a general tendency for CO adsorption on metal supported Cu layers [Rod92]. The strength of the metal-CO bond and the C-O stretching frequency increase or decrease simultaneously. Since the simple π -backdonation model fails, other theories are taken into consideration to explain the CO vibrational shifts [Ryb89, Pac91]. Interactions between the CO dipole moment and the positive charge on the metal to which the molecule is bound as well as the so-called Wall effect, this is the repulsion originating when the CO molecule stretches in the presence of the rigid surface, are supposed to contribute to the observed frequency behaviour.

The possible physical origin of the population of the 2090 cm^{-1} top-site species on Pd(110) in the presence of copper will be discussed in the next chapter. In view of some quantitative analysis of this phenomenon, the CO adsorption on Cu/Pd(110) surfaces will be discussed now for Cu deposition temperatures different from 400

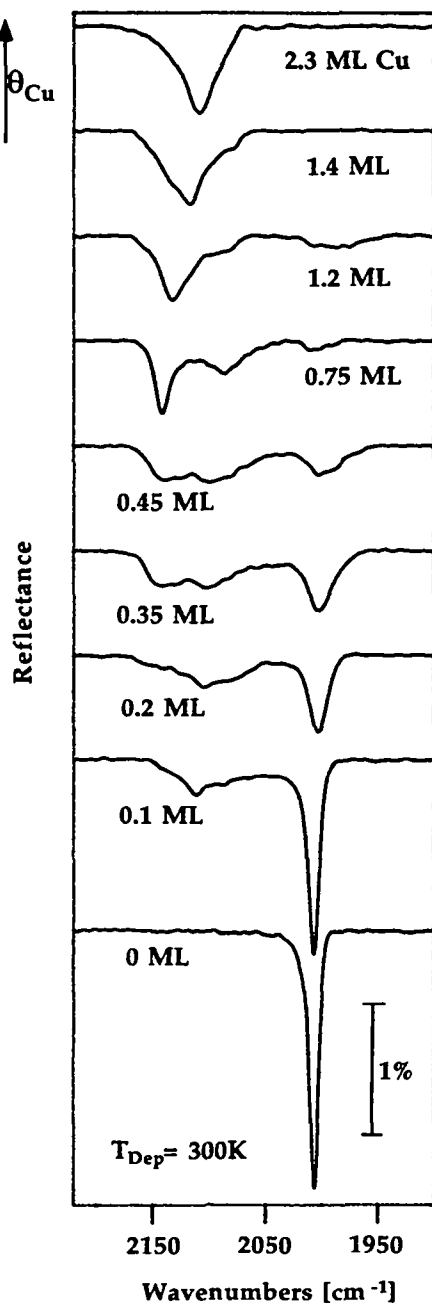
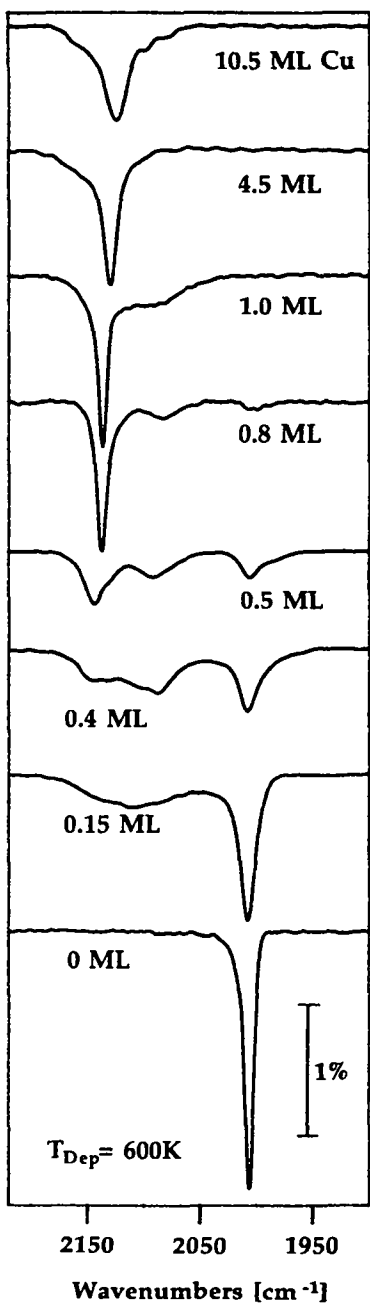


Fig.6.7 (next page): Integrated relative intensities of the infrared absorption bands of CO on Cu sites, on Pd-top sites (2090cm^{-1}) and Pd-bridge sites (2000cm^{-1}) as functions of Cu coverage and Cu deposition temperatures, obtained by peak fitting. The lines are "best fits by hand" to guide the eye.

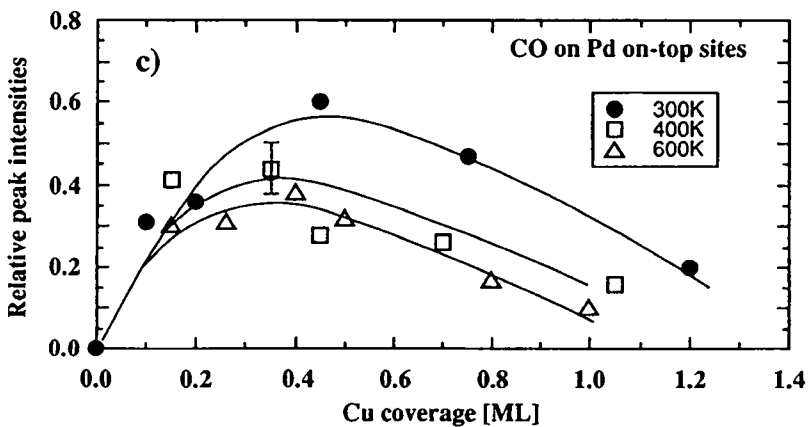
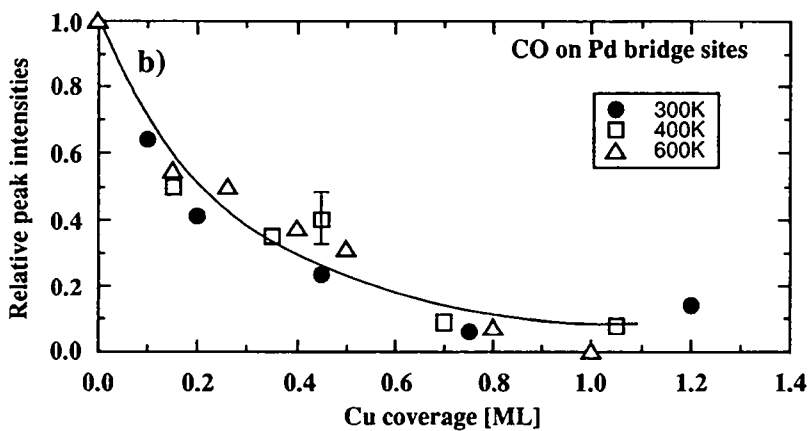
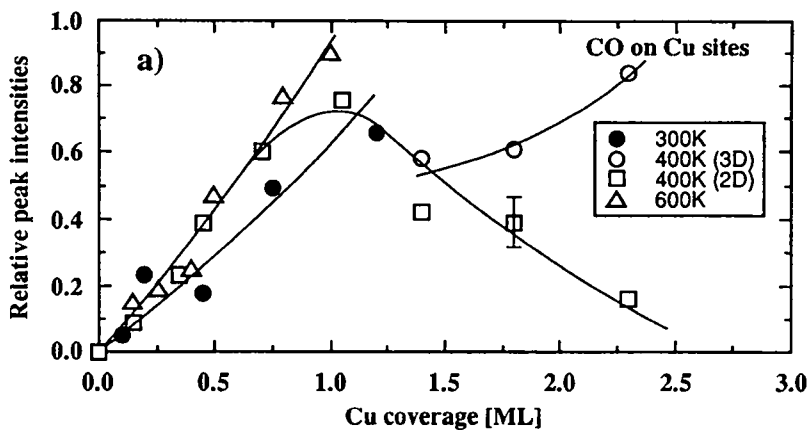
K. Fig.6.6 shows vibrational spectra of CO on Cu/Pd(110) with Cu deposited at $T_S=300\text{K}$ (right hand side) and $T_S=600\text{K}$ (left hand side). Fig.6.7 shows again schematically the relative intensities of all absorption peaks. The spectra in the Cu submonolayer range do not differ much from each other, however the following trends can be observed:

- * With increasing Cu coverage the intensity of the absorption peak at 2000cm^{-1} attributed to CO on Pd bridge sites decreases continuously. At $\Theta_{Cu}=1$ the band has disappeared in the 600K case, whereas upon deposition of 1.2ML Cu at 300K substrate sites are still available. This is in agreement with the STM observations showing a 3D growth mode at 300K and a layerwise Cu growth at 600K.

- * The high frequency mode characterizing CO molecules on the first flat Cu layer sharpens with increasing Cu deposition temperature (18cm^{-1} at 300K, 15cm^{-1} at 400K, 12cm^{-1} at 600K, all values for $0.7 \leq \Theta_{Cu} \leq 0.8$), indicating a higher degree of order in the CO adlayer. This can be explained by the nucleation of larger Cu islands at higher substrate temperatures, permitting the formation of larger well ordered CO domains on top of the islands.

- * The intensity of the Pd top-site peak at 2090cm^{-1} - 2070cm^{-1} initially increases with Θ_{Cu} , then shows a more or less flat maximum before decreasing again for $\Theta_{Cu} \geq 0.5$. At a given Cu coverage, the peak intensity is lower for higher Cu deposition temperatures.

In the copper multilayer range, the CO infrared spectra can easily be related to the STM observations. In contrast to the 400K case, where two CO absorption bands



characterize the layer-plus-island growth mode of Cu, the layerwise Cu growth at $T_S=600\text{K}$ leads to the formation of only one single CO infrared peak up to the highest Cu coverages studied. This peak is narrowest at $\Theta_{Cu}=1$ (10cm^{-1}) but broadens and shifts to lower frequencies when the Cu coverage increases. The broadening indicates imperfections in higher Cu layers, which is indeed confirmed by STM measurements (unidirectional compression, formation of dislocations). It is interesting to note that despite the downshift of the peak frequency, even at $\Theta_{Cu}=10.5\text{ML}$ typical CO-bulk Cu vibrational frequencies are still not revealed.

The Volmer-Weber growth of Cu at $T_S=300\text{K}$ is characterized by the occurrence of a broad (40cm^{-1} at $\Theta_{Cu}=2.3$) absorption band which is assigned to CO molecules adsorbed on small three-dimensional Cu clusters. The frequency downshift is much faster than in the case of layerwise growth. The infrared spectra of CO adsorbed on Cu layers grown at low temperatures ($T_S=150\text{K}$) were likewise studied (not shown). Throughout the whole Cu coverage range, a very broad band centered around 2100cm^{-1} was observed, the contributions of CO adsorbed on Pd on-top and Cu sites to this band could not be resolved anymore. The 2000cm^{-1} substrate peak is still present at Cu coverages as large as 2ML .

6.3 Cu induced CO adsorption site change on Pd(110)

Assuming that the assignment of the 2090cm^{-1} and 2000cm^{-1} bands to Pd top sites and bridge site species, respectively, is correct, then a partial change in CO adsorption site from bridge to on-top geometry on Pd(110) terraces occurs in the presence of Cu. In the following the spatial distribution of the different substrate sites as a function of the surface morphology and possible physical origins of the Cu induced CO site change will be discussed in a semiquantitative way. Coadsorbate-induced site changes of CO in themselves are not too surprising and have been observed in a

number of systems including coadsorption with benzene [Mal85] or alkalis [Wes86]. In these cases the adsorption site change is localized, only affecting CO molecules neighbouring the coadsorbed species. In the bimetallic system Cu/Ni(111), under certain conditions, Ni top-site CO is observed instead of Ni-CO bridge species [Gar89], being thermodynamically favoured on clean Ni(111). This is attributed to 2D mixing of Ni and Cu, generating isolated Ni atoms from each other. The simultaneous observation of a mixed CuNi bridge site strongly supports this assumption.

In chapter 5.2 it was demonstrated that Cu adatoms migrate along the [001] direction on Pd(110) via exchange processes involving Pd atoms. So it seems only logical to interpret the occurrence of Pd top-site CO as a result of CuPd intermixing through cross-channel diffusion. The absence of a mixed CuPd site, of Pd sites at coverages $\Theta_{Cu} > 1.1$ upon Cu deposition at $T_S \geq 400\text{K}$ and the observation of Pd bridge sites up to $\Theta_{Cu} = 1$ however strongly disfavour this speculation. It is obvious from fig.6.7 that the intensity of the Pd top-site CO absorption band decreases with increasing Cu deposition, contradictory to a thermally activated CuPd mixing. At $T_S = 300\text{K}$, diffusion of a Cu adatom across the close packed substrate rows is still nearly frozen in (fig.5.4). In addition, it was shown that a Pd atom on top of the first substrate layer is energetically unfavourable. Consequently, the creation of isolated Pd adatoms at low temperatures is a rare event: to a first approximation, only a fraction of $\exp(-0.15\text{eV}/kT)$ (fig.5.7), that are 0.3% at 300K, of those Pd atoms which were involved in cross-channel displacements will remain as adatoms. Assuming that these Pd adatoms stick to existing Cu islands, CO molecules bond to these isolated Pd atoms would not be observable due to dielectric screening [Per81] by the surrounding CO molecules bound to Cu atoms. So CuPd intermixing is no satisfactory explanation for the presence of a strong Pd top-site CO absorption band, especially at low Cu deposition temperatures. Finally I note that only upon annealing Cu layers on Pd(110) at temperatures above 700K, CuPd alloying is indeed observed (see next

chapter).

An explanation for the occupation of the Pd on-top sites which suggests itself upon inspection of the STM images is a local site change at Cu island edges. The picture of steps as local active sites can easily be examined by comparing the step lengths of Cu islands and Pd top-site CO infrared intensities for Cu coverages below about 0.5ML. At 300K the nucleation density of Cu islands is 8.5 times higher than at 400K (fig.5.4). In addition the aspect ratio of the condensed Cu islands is 3 times larger at 300K, in total giving rise to a 13 times increased step length of Cu islands at identical coverage. Although the total Cu step length is increased by more than an order of magnitude, the total amount of CO in Pd on-top geometry increases only by about 15% (fig.6.7).

Even a superficial glance at the amount of Pd top-site CO demonstrates that a local scenario can not be appropriate: at 400K (300K) and a Cu coverage of $\Theta_{Cu}=0.45$ about 40% (55%) of the total integrated absorption intensity falls to CO molecules adsorbed on Pd on-top sites. Although the peak intensities are not exactly proportional to the population of the corresponding adsorption sites (see below), these numbers do indeed favor a rather *long-range modification* of the Pd substrate by the adsorbed Cu islands. Two phenomena might cause such mesoscopic modifications: modified electronic density of states or stress effects due to the lattice mismatch between Cu and Pd.

The Cu island edges act as barriers for electron waves. The interference between incident electron waves and waves reflected from a step edge results in the formation of standing waves and the modulation of the electronic density of states near the step. These two-dimensional electron standing waves have been measured directly in two recent STM experiments [Cro93, Has93]. The electron density modulations are indeed found to have mesoscopic decay-lengths up to 100Å. In this picture the total amount of site-converted CO should also scale with the total Cu step length reflecting

the electron waves, which is, however, not seen in the experiment (see above). The STM experiments showed in addition that the change in potential at the step leads mainly to electron reflection at the upper terraces (in our case the Cu islands or terraces). Electronic long range modifications are thus unlikely to be the cause for the observed adsorbate site change.

Long-range elastic interactions, on the other hand, offer a natural explanation for the altered chemical properties of the Pd(110) terraces. Because of the large lattice mismatch (7%) between the Cu and Pd lattice parameters the adsorbed Cu islands are substantially strained. The strained islands exert a force on the substrate which induces a build up of stress in the topmost Pd layers. From the LEED and STM investigations it can not be concluded that this effect results in a measurable displacement of the Pd atoms in the first layer, but the mentioned Cu island ordering (chapter 5.4) is an indication for the presence of surface stress. The stress in the substrate induced by adlayer islands is supposed to decay logarithmically with distance from the island center and its amplitude should scale with the mass of the island [Lan93]. It is the latter fact which explains the small difference between CO in Pd on-top geometry on the Cu/Pd(110) surface with the Cu islands grown at 300K and 400K. While at 300 K the total island boundary is about 13 times larger the mass of an average island is 8.5 times smaller than at 400K.

To get some more insight into the stress induced modification of the Pd(110) surface a detailed analysis of the 600K case is particularly useful. In chapter 5 it was shown that at this temperature the first Cu layer wets the substrate in a pure step flow mode. Thus on every substrate terrace at a given Cu submonolayer coverage, a zone reaching from the Cu step edge to a certain distance D_{max} apart from it is assumed to be elastically distorted. D_{max} , the "reach" of the substrate modification, can be estimated by analysing the intensities of the CO infrared bands. It is difficult to infer the populations of the different adsorption sites directly from the intensities since the

infrared absorption cross section depends on the site. The cross section of CO on Cu surfaces is twice as high as on Pd surfaces [Woo82], on the other hand the saturation coverage of CO on Pd(110) ($\Theta_{sat}=1$) is higher than on Cu(110) ($\Theta_{sat}=0.8$). For CO on Pt(111) [Sch89], a ratio of 0.77 is reported for the vibrational cross sections of bridge CO and top-site CO, which would mean an overestimation of the number of Pd top-site CO molecules in the case of Cu/Pd(110).

In the 600K case, the infrared absorption band assigned to CO on Pd bridge sites decreases continuously in intensity and disappears at $\Theta_{Cu}=1$ (figs.6.6, 6.7). The Pd top-site CO band intensity is more or less constant after an initial increase and decreases for $\Theta_{Cu} \geq 0.5$, being only present as a shoulder at $\Theta_{Cu}=1$. The behaviour of the band intensities of CO on Pd sites rules out the possibility that sharp domain boundaries exist between CO on top sites and on bridge sites. Otherwise, bridge CO would not be observable anymore at $\Theta_{Cu}=0.8$ and the decrease of the on-top band would start later. More likely, the amount of CO adsorbed on Pd on-top sites increases monotonically towards a Cu step edge, in coexistence with CO on Pd bridge sites. From the behaviour of the Pd on-top band it can be concluded that at low Θ_{Cu} , the penetration of the Cu island induced substrate stress increases with Θ_{Cu} until a saturation value at about $\Theta_{Cu}=0.4$ is reached. The onset of the intensity decrease of the on-top peak at $\Theta_{Cu}=0.5$ leads to an estimation of the penetration-depth of the substrate modification of 40Å or about 10 Pd atomic spacings, keeping in mind the average terrace width of only 85Å.

6.4 High temperature CuPd intermixing

As mentioned in chapter 5.4, Cu grows layerwise in a step-flow mode at substrate temperatures above about 600K. For $\Theta_{Cu} < 5\text{ML}$, Cu films appear completely flat in STM images. The observed morphology does not change upon deposition or annealing of Cu layers at higher temperatures (fig.6.8), in particular no formation of 3D Cu



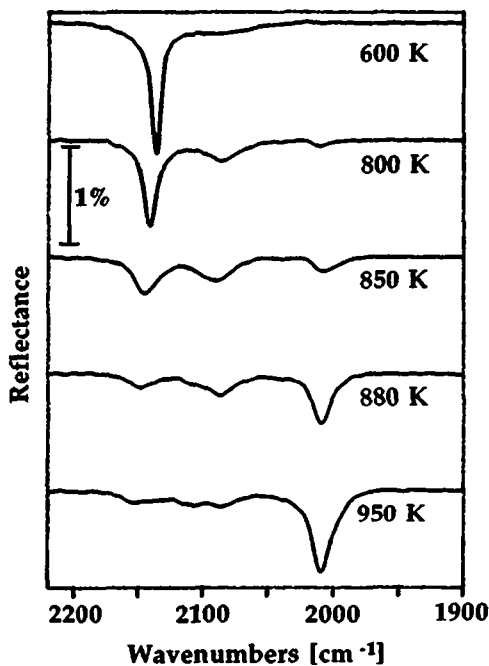
500 Å

Fig.6.8: STM image ($1200\text{\AA} \times 1200\text{\AA}$) of 1.2 ML Cu deposited at 600 K and subsequently annealed at 850 K. The image was taken after quenching the crystal to room temperature.

clusters occurs.

However, RAIRS measurements of CO deposited at $T_S=150\text{ K}$ on high temperature annealed Cu layers give a completely different picture. Fig.6.9 shows again the RAIR spectrum of CO on 1.0 ML Cu on Pd(110) deposited at 600 K (top spectrum): a sharp band at 2136 cm^{-1} characterizing CO molecules adsorbed on the flat Cu layer is present. The crystal was subsequently annealed at the indicated temperatures for 60 s, ensuring complete CO desorption. After recooling to 150 K, the surface was again exposed to CO until saturation coverage was reached. The corresponding spectra are also shown in fig.6.9. Until about 700 K no change in the spectra is seen, even after longer annealing times. After annealing at 800 K, the absorptions band at 2085 cm^{-1} and 2008 cm^{-1} reappear, indicating that Pd substrate sites become available through annealing. With increasing annealing temperatures, the Cu-CO band intensity weakens continuously and the peak maximum shifts to higher frequencies (2155 cm^{-1} after an anneal at 950 K). The intensity of 2085 cm^{-1} band remains constant until 880 K whereas the 2008 cm^{-1} band intensity increases. The CO-Pd bands show

Fig.6.9: RAIRS spectra of CO adsorbed at $T_S=150\text{K}$ on 1.0ML Cu deposited at 600K (top spectrum) and on 1.0ML Cu annealed at the indicated temperatures. Resolution 4cm^{-1} , 400 scans averaged.



no frequency shift. Finally upon annealing at 950K, the spectrum of clean Pd(110) is nearly restored.

Similar results were obtained upon direct adsorption of CO on a Cu monolayer deposited at elevated temperatures or upon annealing of thicker Cu layers. Attempts to detect Cu desorption failed, so it is concluded that CuPd intermixing occurs at $T_S \geq 800\text{K}$. The spectra show that the mixing is not confined to the first substrate layer, but that Cu diffuses into the Pd bulk, eventually forming a substitutional alloy, as suggested by the CuPd bulk alloy phase diagram [Han58]. Intensive attempts were made to detect this phenomenon by STM. Cu and Pd atoms in the same layer can not be distinguished (chapter 5.4) and no "holes" in the uppermost layer were found upon Cu/Pd-intermixing. From the flat imaging of the intermixed surface it appears

that a Cu atom is replaced by an underlying Pd atom through an interlayer exchange mechanism. From fig 6.9 it is evident that upon annealing to 800K the band at 2085cm^{-1} is much more intense than the band at 2008cm^{-1} . This is an additional confirmation for the correctness of the assignment of the bands to top-site (2085cm^{-1}) and bridged species (2008cm^{-1}). Upon intermixing isolated Pd atoms are created first before Pd patches are formed and bridge sites become available.

7. Growth and CO adsorption properties of Cu films on Pd(100)

7.1 Cu adatom diffusion on Pd(100)

In the following chapters, the growth and CO adsorption properties of Cu on Pd(100) will be examined. This system is of particular interest because recent theoretical [Mor89] and experimental [Li 89] studies reported on a new crystalline Cu phase with body-centered-tetragonal (bct) structure growing on Pd(100). Details will be presented in chapter 7.2. First, a determination of the energy barrier for copper adatom diffusion on the substrate is performed. The Pd(100) crystal (this surface exhibits a square surface unit mesh with $a=2.75\text{ \AA}$) was prepared by cycles of argon ion bombardment, oxygen treatment and high-temperature annealing as described in chapter 5.2 for Pd(110). Much less preparation cycles (ca. 10) were however necessary to obtain a sharp LEED pattern and an Auger-clean surface. The average terrace width on a well annealed surface was about 500 \AA , thus much larger than on Pd(110).

Submonolayer Cu island formation as a function of deposition temperature is shown in fig.7.1. Cu coverage ($\Theta_{Cu}=0.15\text{ ML}$) and evaporation rate ($1.4 \cdot 10^{-3}\text{ ML/s}$; $1\text{ ML}=1.32 \cdot 10^{15}\text{ atoms/cm}^2$) were the same for all deposition temperatures. Small, irregular shaped islands are formed, the average island diameter increases from 40 \AA at 300 K to 120 \AA at 450 K . Surprisingly, at $T_S \geq 400\text{ K}$ (figs. 7.1c and d) a slight elongation of the islands (ca. 20% in average) is noticed, here along the vertical axis. This is neither due to thermal drift of the microscope (this could simply be excluded by turning the scan direction of the tip) nor to the local substrate step orientation (see fig 7.1d).

The decrease of the density of Cu islands with increasing deposition temperature is shown in fig.7.2 in a logarithmic plot. At temperatures below 400 K , the island density shows Arrhenius behaviour before decreasing sharply at higher deposition temperatures, indicating probably that at this temperature the Cu trimer becomes

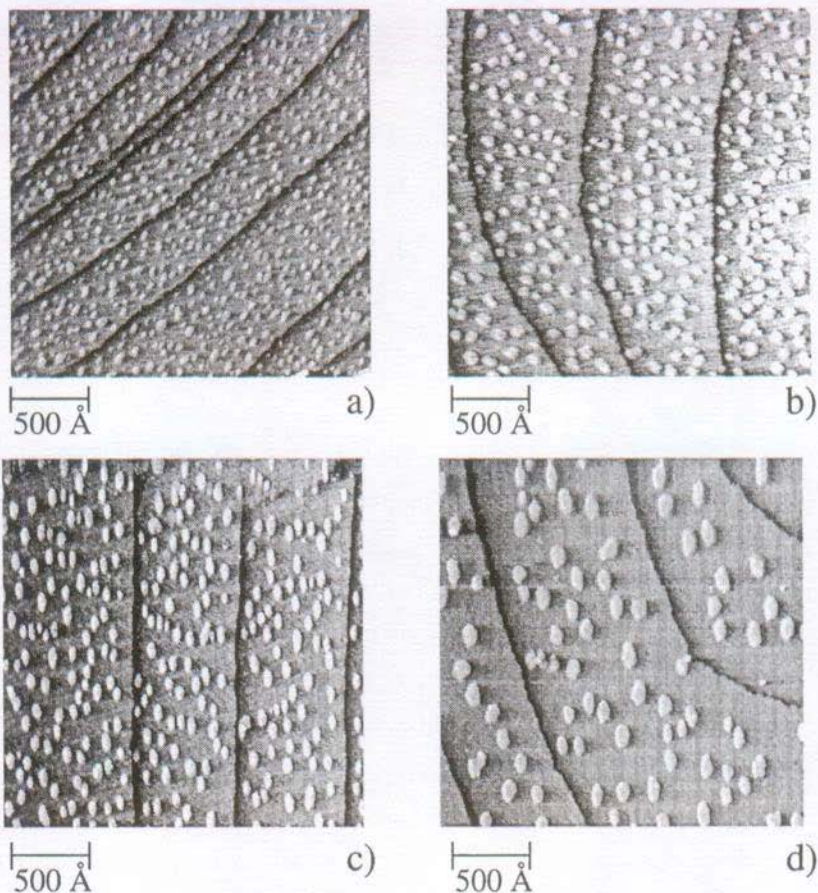


Fig.7.1: STM images showing submonolayer Cu islands ($\Theta_{Cu}=0.15\text{ML}$) deposited at a) $T_S=300\text{K}$, b) $T_S=350\text{K}$, c) $T_S=400\text{K}$, d) $T_S=450\text{K}$.

Size of the images $2400\text{Å} \times 2400\text{Å}$.

the stable nucleus. From the linear part of the curve, a migration barrier of 0.28 ± 0.03 eV has been inferred by using equation (5.8) for twodimensional adatom diffusion. For Cu on Cu(100), a similar value ($0.28 \pm 0.06\text{eV}$) was obtained by He scattering inves-

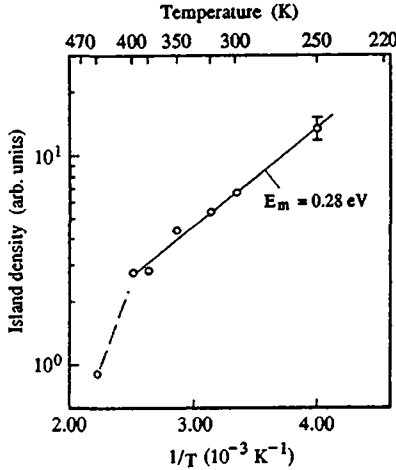


Fig.7.2: Arrhenius plot of the Cu island density on Pd(100) as a function of $1/T$, where T is the Cu deposition temperature.

tigations [Ern92]. It is likely that Cu diffusion on Cu(100) is promoted by cross exchange mechanisms: by effective medium theory a barrier of 0.21 eV was computed for the exchange process, while simple hopping is characterized by a barrier of 0.40 eV [Han91]. For Cu atoms on Pd(100), an energy barrier of 0.72 eV for hopping was obtained by molecular dynamics simulations [San91]. Thus the significantly lower experimental value suggests that Cu diffusion on Pd(100) is triggered by exchange. CO adsorption measurements (chapter 7.3) show however that no CuPd intermixing occurs at $T_S < 450$ K, so that more elaborate diffusion mechanisms might be required to explain both experimental results, in analogy with Cu/Pd(110). Currently, corresponding EAM calculations are made to investigate this question in more depth.

7.2 The growth of thin Cu films on Pd(100)

7.2.1 Bulk structural properties of bct copper

In heteroepitaxial systems with large lattice misfit, the overlayer may adopt a crystal structure that is well lattice matched to the substrate but differs from the structure that the overlayer material normally would adopt in the bulk. Examples for such

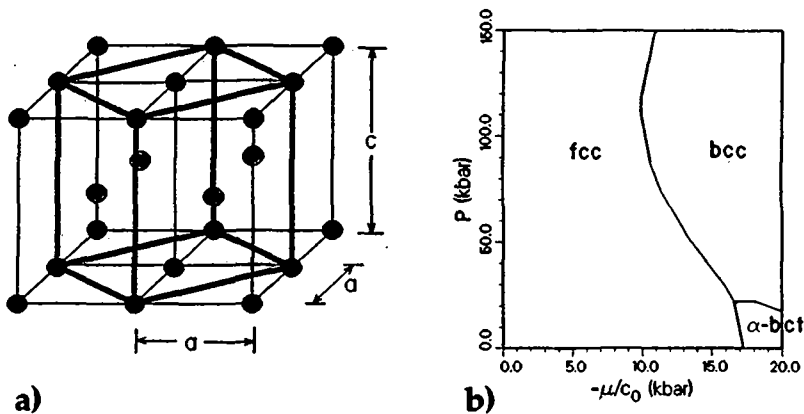


Fig.7.3: a) Relationship between bct and rotated fct unit cell.

b) Equilibrium structural phase diagram of bulk Cu as a function of biaxial tension μ scaled by the Cu lattice constant $c_0=3.61 \text{ \AA}$ vs external hydrostatic pressure P.

Both images from [Mor89].

pseudomorphic systems are Sn adopting its low temperature "gray tin" diamond structure when deposited at 300K on InSb or CdTe [Far81], or bcc Co growing on GaAs(110) [Pri85].

Ab initio total energy calculations employing pseudopotential descriptions examined the stability of a continuous range of Cu bulk structures between fcc and bcc within the (hypothetical) body-centered-tetragonal (bct) crystal system as a function of a , the side of the square cross section and c , the height of the bct cell [Mor89]. The fcc and bcc lattices are high-symmetry structures of the bct lattice (fig.7.3a): for $c/a=1$, the bct lattice reduces to a bcc lattice, for $c/a=\sqrt{2}$, the 45° rotated fct unit cell becomes a fcc unit cell. The total energy calculation with the structural parameters c/a and V/V_0 , which is the unit-cell volume scaled by the experimental fcc Cu unit-cell volume, revealed not only the global energy minimum at the fcc structure ($c=3.61 \text{ \AA}$, $a=2.55 \text{ \AA}$), but predicted two additional stable Cu bulk structures, present

as local minima in the energy contour plot: a bcc phase ($a=c=2.82\text{ \AA}$) and a bct phase ($a=2.76\text{ \AA}$, $c=3.09\text{ \AA}$). A stable bcc phase with $a=c=2.87\text{ \AA}$ was previously predicted by Chelikowsky et al. [Che88].

Phase transitions between the different lattices can be induced by external stresses. Morrison et al. constructed a phase diagram as a function of applied hydrostatic pressure P and external biaxial surface tension μ [Mor89]. For a given P and μ , the minimum value of the Gibbs free energy $G=E+PV+\mu a^2$ (E : total electronic energy per atom) was calculated for all V and a values considered, representing the equilibrium state of the system (fig.7.3b). At $\mu = 0$, the fcc phase is stable independent of external pressure P . In pure Cu, a phase transition can not be induced by biaxial tension, since the minimum stress necessary to induce plastic deformation in copper is orders of magnitude smaller than the phase transition point. Deposited on a suitable substrate, on the other hand, the microscopic stresses at the interface could be large enough to stabilize the growth of a Cu bcc or bct lattice.

Indeed bcc Cu films, however with large defect density, are formed on Fe(100) [Wan87]. Pd(100), characterized by a square surface mesh with $a=2.75\text{ \AA}$, appears favourable for epitaxy of the predicted bct Cu phase. By LEED investigations [Li 89] it was found that upon deposition of Cu on Pd(100) at room temperature, the pattern remained (1×1) and a detailed I/V analysis of a 4-6ML thick Cu films revealed that the best fit to the LEED data could be obtained for $a=2.75\text{ \AA}$ and $c/2=1.62\pm0.03\text{ \AA}$, corresponding to a true bct phase. Thicker Cu layers were however highly disordered, as indicated by a gradual increase of the diffuse LEED background with Cu coverage. At $\Theta_{Cu}=10\text{ ML}$, the LEED spots were broad and diffuse and disappeared upon deposition of 20ML Cu.

In the following chapter a survey of STM studies of Cu growth on Pd(100) in the temperature range $300\text{ K} \leq T_S \leq 600\text{ K}$ (deposition rate $1.4 \cdot 10^{-3}\text{ ML/s}$) will be given. It will be outlined that the system is more complex than the room temperature LEED

Fig.7.4 (next page): STM images showing the growth of Cu on Pd(100) at $T_S=300\text{K}$. a) 0.15ML, b) 0.55ML, c) 0.9ML, d) 1.3ML, e) 2.4ML, f) 10ML. Image sizes $2400\text{\AA} \times 2400\text{\AA}$ except for a) $1200\text{\AA} \times 1200\text{\AA}$ and c) $1430\text{\AA} \times 1430\text{\AA}$.

data suggest. Since additional investigations are still underway to understand the system completely, the description will remain phenomenologic on some points.

7.2.2 The structure of Cu films on Pd(100)

Fig.7.4 displays a series of STM images showing the growth of Cu on Pd(100) upon deposition at $T_S=300\text{K}$. At $\Theta_{Cu}=0.15\text{ML}$ (fig.7.4a) small, irregular shaped Cu islands are present on the surface. Their average diameter is about 40\AA , the size distribution is rather broad. With increasing coverage, the islands grow together and nice percolation patterns are formed (fig.7.4b). Fig.7.4c shows that at $\Theta_{Cu}=0.9\text{ML}$ there is still no indication of second layer island nucleation. Fig.7.4d ($\Theta_{Cu}=1.3\text{ML}$) and 7.4e ($\Theta_{Cu}=2.4\text{ML}$) reveal that Cu grows in the Frank-van der Merwe mode at 300K . Only one layer is growing at a time. The layer-by-layer growth mode breaks down at about $\Theta_{Cu}=5\text{ML}$, thicker Cu films (fig.7.4f) are rough and disordered. These observations are in agreement with the previous LEED study [Li 89].

Closer inspection of figs.7.4d/e reveals that in the Cu multilayer range two different step heights occur (see arrow in fig.7.4e). Fig.7.5a displays a detail of fig.7.4e in the absolute height representation. From horizontal line scans (fig.7.5b), the step heights are determined to be $1.55 \pm 0.1\text{\AA}$ and $0.4 \pm 0.1\text{\AA}$. The sum of the two step heights is equivalent to the interlayer spacing of Pd(100) (1.95\AA), which suggests the model shown in fig.7.5c. The larger step height (1.55\AA) corresponds to the distance between two layers of the deposited Cu film. This value is in good agreement with Refs.[Li 89] and [Mor89]. Since this distance is considerably smaller than the step height on the Pd substrate, the boundary between Cu which has diffused to a step edge and the adjacent terrace is visible in the STM image and gives rise to the small 0.4\AA step.



200 Å

a)



500 Å

b)



500 Å

c)



500 Å

d)



500 Å

e)



500 Å

f)

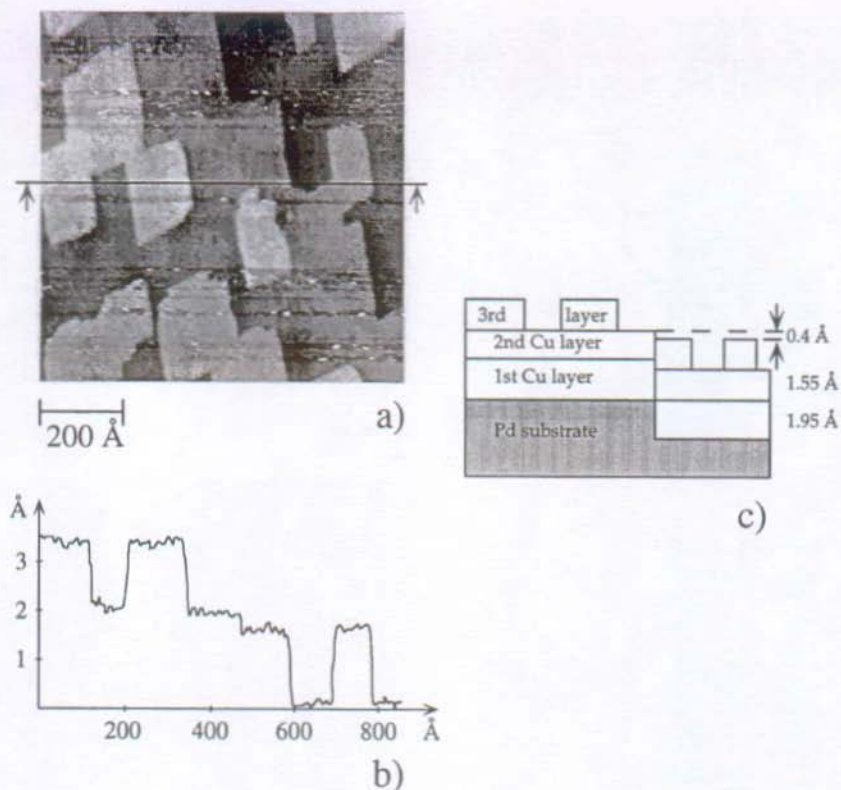


Fig.7.5: a) $600\text{ Å} \times 600\text{ Å}$ -STM image of 2.4 ML Cu on Pd(100) in a grey scale height representation. Horizontal lines are perturbations due to tip instabilities.

b) Horizontal line scan along the bar in image a)

c) Growth model explaining the occurrence of two different step heights on the Cu/Pd(100) surface.

The model assumes that the distance between the first Cu layer and the Pd substrate is equal to the interlayer spacing on Pd(100), since submonolayer Cu and Pd are undistinguishable in the STM images (still electronic effects may cancel topological height differences in the Cu submonolayer range). The determination of the Cu-Cu



Fig.7.6: (1×1) LEED- pattern of 2.4ML Cu deposited on Pd(100) at 300 K. Electron energy 110eV

interlayer spacing does however not depend on the correctness of this assumption.

The flat imaging of the Cu islands by STM, the observation of a (1×1) LEED pattern throughout the whole Cu coverage range ($\Theta_{Cu} \leq 10\text{ML}$) and the measured interlayer spacing strongly support the assumption of a Cu bct phase growing on Pd(100). One observation does however not fit to this model, that is the shape of the Cu islands in the multilayer range. On a substrate with square unit mesh one would expect the formation of square islands or at least rectangular islands. However rhombic Cu islands are actually observed, the angles between two neighbouring island edges are $60-70^\circ$ and $110-120^\circ$, respectively. It was excluded that the observed island shapes are the results of any experimental artefacts like thermal drift effects. Rhombic islands are more likely found on substrates with hexagonal (fcc(111)) or quasi-hexagonal (bcc(110)) unit cell. The formation of adlayers with (quasi-) hexagonal symmetry on a substrate with square symmetry would however result in strong diffraction superstructures. However there is not the slightest indication for the presence of any superstructure in LEED (fig.7.6). Therefore the occurrence of the rhombic islands has to be explained within the mentioned model assuming a Cu bct phase. On the basis of the present data, no compelling explanation can be found unless

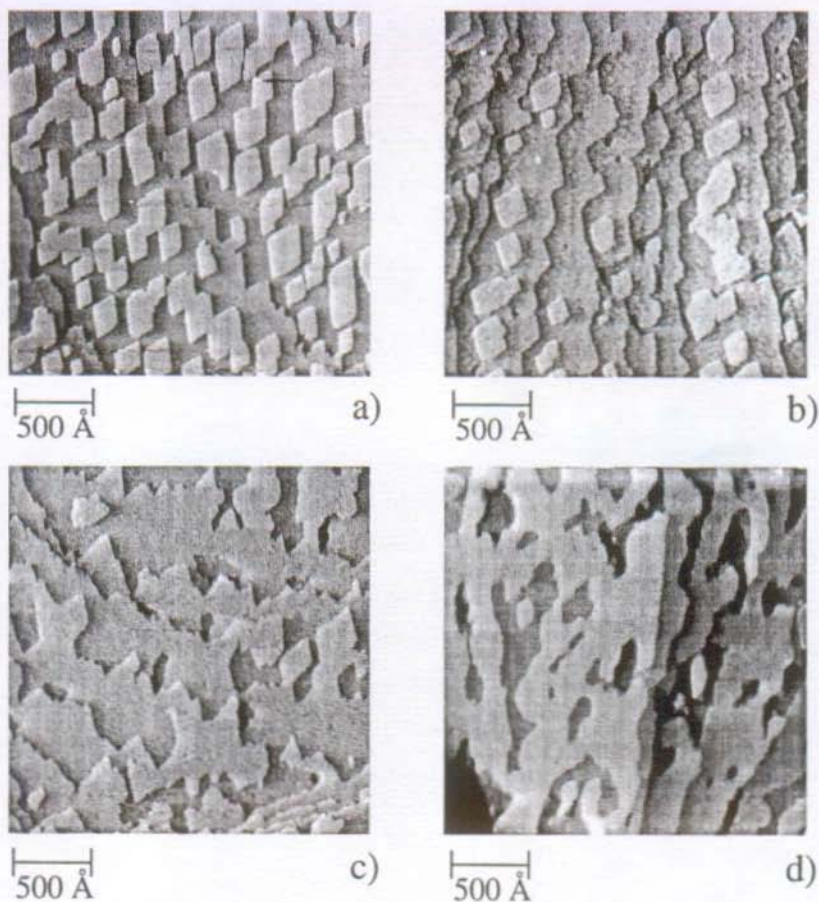


Fig.7.7: a) STM image of 2.4ML Cu deposited at $T_S=300$ K. b)-d) The same surface heated and imaged at b) 350K, c) 400K, d) 450K. Image sizes $2400\text{ \AA} \times 2400\text{ \AA}$.

the islands are imaged with atomic resolution. One might speculate that two of the island edges are oriented along the $[100]$ direction of the substrate (the preferential direction of straight substrate steps, see right hand side of fig.7.4d) and the remaining two island edges are stepped ("one-dimensionally faceted").

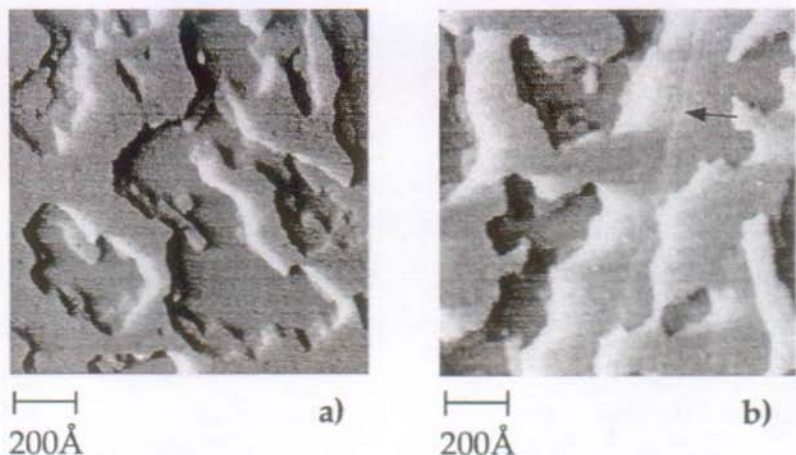


Fig.7.8: $1200\text{ \AA} \times 1200\text{ \AA}$ -STM images of 2.4 ML Cu deposited at 300 K, a) annealed and imaged at 450 K, b) after recooling to 300 K.

Fig.7.7 shows that rhombic islands and Cu bct phase are not stable towards thermal annealing. At a Cu coverage of 2.4 ML the crystal was heated from 300 K to 450 K in steps of 50 K and imaged at the same temperatures. At 350 K (fig.7.7b), the onset of island coalescence is observed. The shape of isolated islands remains nearly unchanged and the small 0.4 \AA step is still present in the STM images. At 400 K (fig.7.7c), the islands have completely dissolved. Cu has diffused to the step edges or forms large patches on the terraces. However the rhombic symmetry is not completely lost, as can be recognized by the preferential orientations of the step edges. Upon annealing at 450 K, no straight Cu step edges are present anymore and the topmost Cu layer forms a percolation network (fig.7.7d).

The drastic morphology changes in the topmost Cu layer is accompanied by a relaxation of the whole Cu film. The small 0.4 \AA step has vanished upon annealing at 450 K, which indicates an expansion of the Cu interlayer distance. Only steps of $1.9 \pm 0.1\text{ \AA}$ height are present, corresponding within the experimental error bars to the interlayer spacing in the Cu fcc(100) bulk structure. Thus it is likely that a phase

Fig.7.9: (next page): STM images showing the growth of Cu on Pd(100) at $T_S=400\text{K}$. a) 0.15ML, b) 0.55ML, c) 1.3ML, d) 2.5ML, e) 3.3ML, f) 4.3ML.

Image sizes $2400\text{\AA}\times 2400\text{\AA}$ except for e) $4800\text{\AA}\times 4800\text{\AA}$.

transition to fcc Cu has occurred between 400K and 450K. It becomes evident from fig.7.8a which shows the surface at 450K in more detail, that annealing results even in the formation of 3D Cu structures located on the first flat Cu monolayer (which remains intact as confirmed by CO adsorption measurements, see chapter 7.3). There are indications for a reversibility of the bct \rightarrow fcc transition. When the crystal is cooled again to 300K, the 0.4\AA step reappears in STM images (arrow in fig.7.8b).

The bulk phase transition point is not only determined by temperature, but also by the thickness of the Cu film. Fig.7.9 displays a series of STM images showing the growth of Cu on Pd(100) at 400K. At $\Theta_{Cu}=0.15\text{ML}$ (fig.7.9a) Cu clusters with an average size of 80\AA and a much narrower size distribution than at 300K are formed. At $\Theta_{Cu}=0.55\text{ML}$ (fig.7.9b), island coalescence has occurred. After the completion of the first monolayer, one observes the nucleation of small, irregular shaped Cu clusters (fig.7.9c), the nucleation density in the second layer is much higher than upon deposition at 300K. The upper step edges are wetted with Cu, a similar phenomenon as on Pd(110) (chapter 5.4). The surface morphology at $\Theta_{Cu}=2.5\text{ML}$ (fig.7.9d), a percolation network formed after island coalescence, resembles the corresponding submonolayer situation (fig.7.9b). The differences to the growth at 300K are obvious. The absence of the small 0.4\AA step is accompanied by a striking change in island shape: instead of large regularly shaped Cu islands small clusters are found on top of the first and second layer.

However deposition of $\geq 3\text{ML}$ Cu results in a surprising change of the growth mode (figs.7.9e and f). No Cu islands are observed anymore, even on the largest terraces, thus Cu grows thus in a step-flow mode. The reappearance of the small 0.4



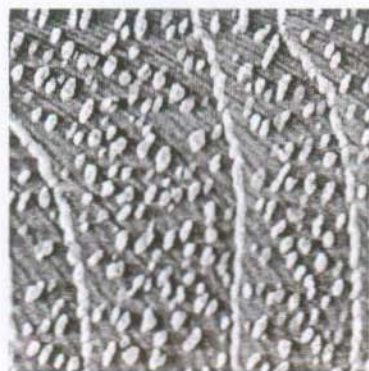
500 Å

a)



500 Å

b)



500 Å

c)



500 Å

d)



1000 Å

e)



500 Å

f)

Å step is noticed. The step edges reflect the symmetry of the islands found at 300K. Thus growth of the bct bulk phase sets in at a "critical" Cu film thickness. Studies at intermediate deposition temperatures show that below about 370K the distance between the first and second Cu layer corresponds already to the interlayer distance in a bct lattice, whereas at higher deposition temperatures Cu forms a three layer high fcc film before bct growth starts.

The delicate balance between the two structures might be explained as follows. The biaxial tension at the Cu/Pd interface depends on the temperature, since the thermal expansion of both metals is different. The thermal expansion coefficient of Cu is larger ($16.5 \cdot 10^{-6} \text{ K}^{-1}$) than the value for Pd ($11.6 \cdot 10^{-6} \text{ K}^{-1}$) [Met79]. When the temperature increases, the structural misfit between fcc Cu ($a=2.55 \text{ Å}$) and Pd substrate ($a=2.75 \text{ Å}$) is thus reduced whereas the misfit between bct Cu ($a=2.76 \text{ Å}$ at $T=0\text{K}$) and Pd becomes larger. Although this thermal expansion effect is not tremendous, in terms of tension at the interface it could be decisive in the stabilisation of either the fcc or the bct phase, when the system is near the phase transition point. On the other hand, the biaxial tension increases linearly with the film thickness [Das86]. Therefore at a critical thickness, the tension will reach the value necessary to induce the fcc \rightarrow bct phase transition.

7.2.3 CuPd intermixing at $T_S \geq 500\text{K}$

When Cu is deposited at $T_S \geq 500\text{K}$ (fig.7.10), again substantial changes in the observed surface morphology are found. In the Cu submonolayer range (fig.7.10a), the island density is low and island formation occurs only on large terraces. In the Cu multilayer range, island formation is completely missing (fig.7.10b). But this does not mean that Cu films grow in a step flow mode at this temperature. Fig.7.10c shows a more detailed STM image at a coverage of $\Theta_{\text{Cu}}=1.6\text{ML}$. On the terraces, a faint corrugation is visible, line scans reveal an amplitude of about 0.3 Å . Lighter

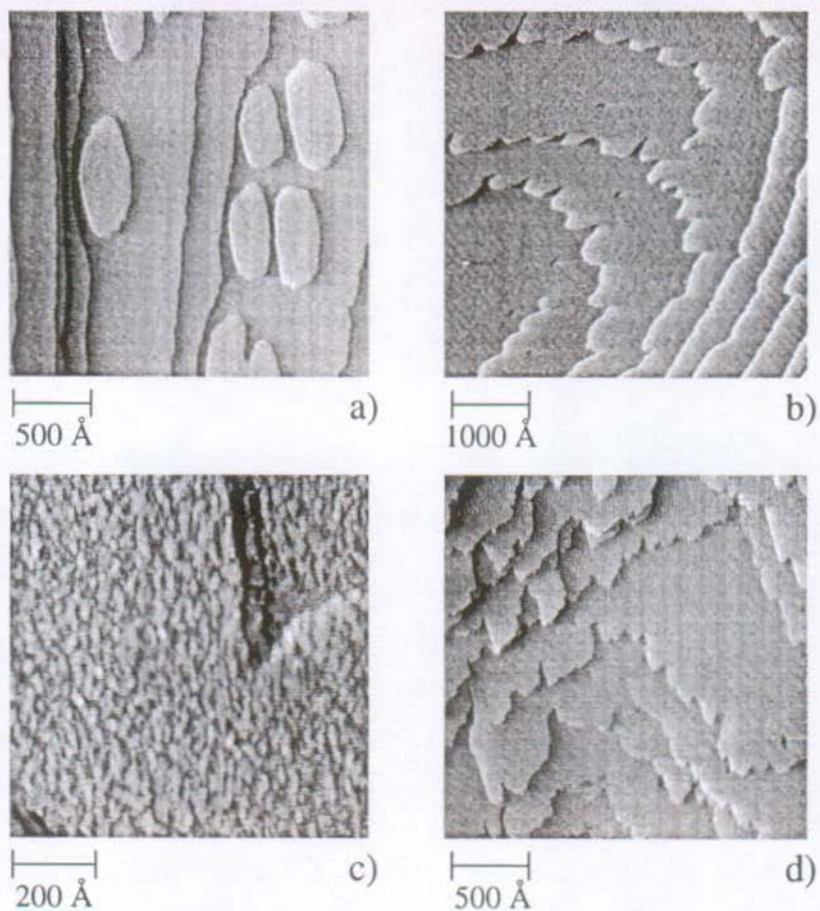


Fig.7.10: Deposition of Cu on Pd(100) at $T_S=500$ K. Coverages a) 0.55 ML, b) and c) 1.6 ML, d) 5 ML. Image sizes a) and d) $2400 \text{ \AA} \times 2400 \text{ \AA}$, b) $4800 \text{ \AA} \times 4800 \text{ \AA}$, and c) $600 \text{ \AA} \times 600 \text{ \AA}$.

imaged regions are separated from darker ones, the diameters of both types of structures on this "patchy" surface are 10-20 Å. A similar phenomenon was observed for



Fig.7.11: $c(2 \times 2)$ LEED pattern of 1.6 ML Cu deposited on Pd(100) at 500 K. Electron energy 110 eV.

Ag/Pt(111) in the submonolayer Ag range [Röd93,1] and was called a "real mixture" of Ag and Pt atoms which denotes that the AgPt mixture is not complete but consists of Ag clusters embedded in a Pt matrix or vice-versa, depending on the Ag coverage. Evidence for the interpretation of fig.7.10c as a CuPd mixture arises from AES, LEED and CO adsorption measurements.

Deposition of 2.3 ML Cu at 300 K resulted in a Cu/Pd Auger peak height ratio of 1:1.5, which is reduced to 1:1.9 after a 5 min anneal of the crystal at 500 K. This indicates a diffusion of Cu atoms into the substrate, resulting in a decrease of the Cu Auger signal due to the finite electron mean free path ($< 10 \text{ \AA}$ for 100 eV electrons [Zan88]). The surface imaged in fig 7.10c shows a $c(2 \times 2)$ LEED pattern (fig.7.11). It is well known that Pd deposition on Cu(100) results in the formation of an ordered $c(2 \times 2)$ surface alloy with alternating Pd and Cu atoms on the Cu substrate [Wu 88]. CO adsorption studies (chapter 7.3) reveal that CuPd intermixing occurs already from the very beginning of Cu deposition on Pd(100) and that at $\Theta_{Cu}=2 \text{ ML}$, still a small amount of Pd *bridge sites* is present in the uppermost layer. Thus RAIRS and LEED results suggest that the "patchy" surface corresponds rather to a mixture of pure Pd clusters and CuPd alloy clusters with a local $c(2 \times 2)$ structure than to

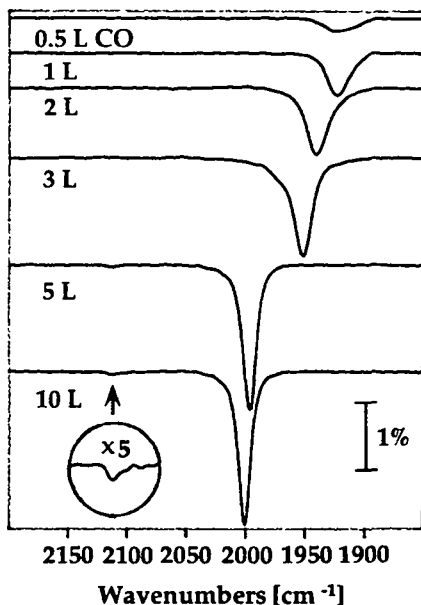


Fig.7.12: RAIR spectra of CO on Pd(100) as a function of coverage. Deposition temperature 150 K. Resolution 4 cm⁻¹, 800 spectra averaged.

a "real" mixture of the AgPt(111) type (more details in chapter 7.3). At higher coverages, Cu grows epitaxially in a step-flow mode on the mixed CuPd layers, as can be concluded from STM (fig.7.10d) and RAIRS data. Very similar results were obtained upon Cu deposition at 600 K.

7.3 CO adsorption on Cu/Pd(100)

Fig.7.12 displays the IR absorption bands due to the C-O stretching mode in the system CO/Pd(100) as a function of increasing exposure. The adsorption temperature is 150 K. Adsorption of 0.5 L CO produces a broad band at 1920 cm⁻¹. Upon further exposure the band intensity increases and the peak maximum shifts over 80 cm⁻¹ to 2000 cm⁻¹ at saturation coverage, the peak halfwidth is reduced to 13 cm⁻¹ at saturation. By LEED, an ordered $(2\sqrt{2} \times \sqrt{2})R45^\circ$ CO structure at $\Theta_{CO}=0.5$ was found

[Ber92] with the CO molecules adsorbed exclusively in bridge sites. At $\Theta_{CO} > 0.5$, several ordered compression structures, denoted by $(n\sqrt{2} \times \sqrt{2})R45^\circ$ with $n = 3, 5, 7$ were observed. The CO saturation coverage is 0.8. These compression structures were explained by the formation of phase/antiphase domains of the $(2\sqrt{2} \times \sqrt{2})R45^\circ$ structure separated by domain walls of higher local CO coverage [Ber92]. It was assumed that all molecules in the domain wall superlattices occupy bridge sites. But as fig.7.12 reveals, a small amount (ca. 7%) of the total integrated intensity falls to CO in on-top configuration (absorption peak at 2108cm^{-1}), indicating probably that some CO molecules at the domain walls undergo a lateral shift away from the bridge sites. This was also reported by [Bra78].

The vibrational behaviour of CO on Cu/Pd(100) was investigated in the same manner as described in chapter 6. Cu films were deposited at a given surface temperature T_S . The crystal was subsequently cooled down to 150K and a background spectrum was recorded. After a flash to 250K, the crystal was then exposed to CO upon recooling to 150K until saturation coverage was reached. Then, the sample spectrum was recorded at this temperature. I concentrate here on two different Cu deposition temperatures, 300K and 600K, in order to show the typical CO adsorption properties of the system.

Fig.7.13a shows absorption spectra of CO on Cu layers previously deposited at $T_S=300\text{K}$. Fig.7.15 displays the integrated intensities of the different bands as functions of Θ_{Cu} , obtained by peak fitting. The band at 2000cm^{-1} , assigned to CO on Pd bridge sites, decreases nearly linearly with Θ_{Cu} . At $\Theta_{Cu}=1\text{ML}$, still 11% of the total absorption intensity falls to Pd bridge sites. This indicates that Cu layer-by-layer growth is not perfect at this temperature. In the Cu submonolayer range, two bands characterize CO molecules on Cu on-top sites. A sharp peak at 2096cm^{-1} develops upon deposition of 0.4ML Cu and increases rapidly in intensity without any frequency shift. At $\Theta_{Cu}=1$, the halfwidth of the peak is only 7.5cm^{-1} . A second, broader band

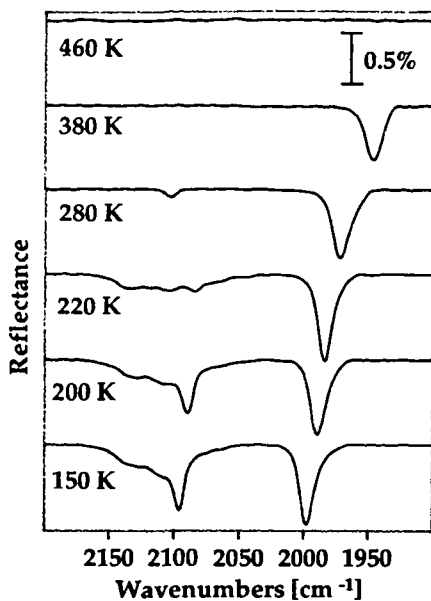
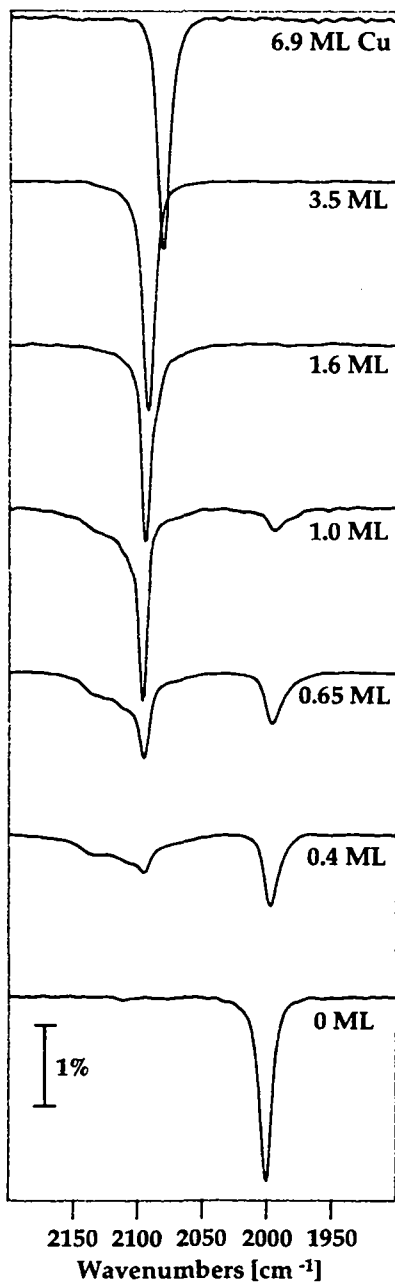


Fig.7.13 a), left hand side: RAIR spectra of CO on Cu/Pd(100) as a function of Θ_{Cu} , Cu deposition temperature 300K.

b), right hand side: Spectra of CO adsorbed on 0.55 ML Cu/Pd(100) at 150 K (bottom spectrum) and upon annealing at the indicated temperatures. Cu was deposited at 300K. Resolution for a) and b) 4 cm^{-1} , 800 spectra averaged.

at 2130cm^{-1} has maximum intensity at $\Theta_{\text{Cu}}=0.5$ before disappearing at $\Theta_{\text{Cu}}>1.2$. Following refs. [He 90] and [Rod92] and in accordance with the STM observations described in chapter 7.2, the broad, high frequency band is assigned to CO molecules on small Cu clusters and island edges whereas the sharp low frequency peak is due to CO on large Cu patches which are large enough to permit the formation of ordered CO islands. This is confirmed by LEED studies. At Cu coverages above 0.5ML, the formation of a sharp $c(2 \times 2)$ pattern is observed upon CO exposure, which may correspond to the $c(2 \times 2)$ structure of CO/Cu(100) [Ryb81].

In the Cu multilayer range, only a single CO absorption band is observed. Its frequency decreases initially slowly, from 2096cm^{-1} at $\Theta_{\text{Cu}}=1.6$ to 2093cm^{-1} at $\Theta_{\text{Cu}}=3.5$, then faster to 2082cm^{-1} at $\Theta_{\text{Cu}}=6.9$. Simultaneously the peak halfwidth increases from 8cm^{-1} to 13cm^{-1} . The faster frequency downshift at higher Cu coverages is due to the change in growth mode from 2D to 3D growth at a Cu coverage of 5ML. (It is recalled that for Cu/Pd(110) the CO absorption band frequency shifts much faster towards typical Cu bulk values in the case of 3D Cu growth than in the case of layerwise 2D growth).

Fig.7.13b shows a warming-up experiment. A Cu coverage of 0.55ML was chosen and the surface was saturated with CO. The crystal was annealed for 60s at the indicated temperatures and recooled to 150K before spectra recording. The desorption of the molecules giving rise to the sharp peak at 2096cm^{-1} occurs first (220K), the high frequency shoulder has disappeared at 280K. Besides the Pd bridge-site CO absorption band, a weak feature at 2110cm^{-1} remains, which is assigned to a small amount of Pd-top site CO, being present also on the clean Pd(100) surface. All CO species have disappeared upon annealing at 460K.

In comparison to the system CO/Cu/Pd(110) the following differences are conspicuous. There is no indication for a Cu induced CO site conversion from Pd bridge to Pd on-top sites on uncovered Pd(100) terraces. The vibrational frequency of

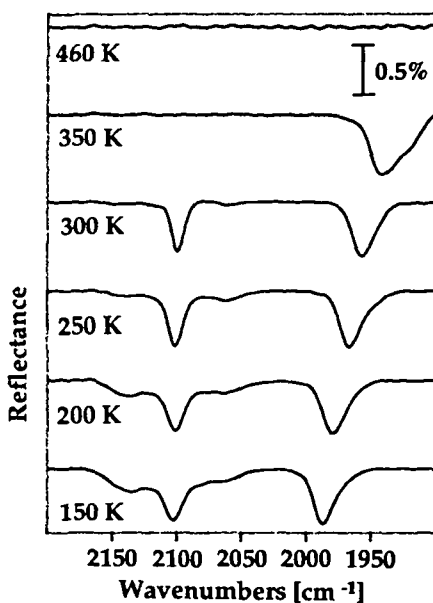
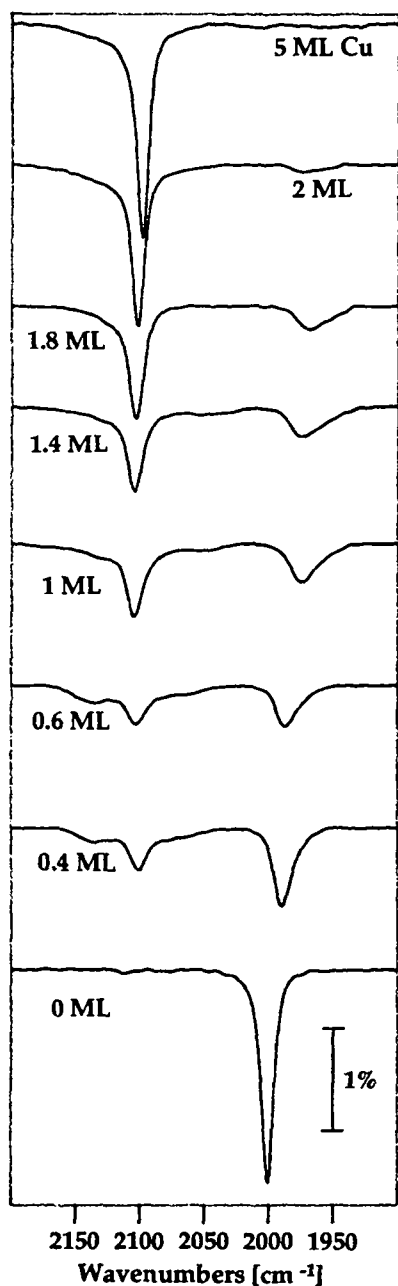


Fig.7.14 a), left hand side: RAIR spectra of CO on Cu/Pd(100) as a function of Θ_{Cu} , Cu deposition temperature 600K.

b), right hand side: Spectra of CO adsorbed on 0.55 ML Cu/Pd(100) at 150 K (bottom spectrum) and upon annealing at the indicated temperatures. The Cu was deposited at 600 K. Resolution for a) and b) 4cm^{-1} , 800 spectra averaged.

CO molecules adsorbed on the first flat Cu monolayer is 50cm^{-1} lower than on Cu/Pd(110) and lies only 10cm^{-1} above the frequency observed for CO on bulk Cu(100) (chapter 2.2). Thus the mutual modifications of the electronic and chemical properties of Cu layer and Pd substrate are supposed to be much less important for Cu/Pd(100) than for Cu/Pd(110). Surface stress effects were demonstrated to play a crucial role in the system Cu/Pd(110). By contrast, the Cu/Pd(100) interface effects which finally result in the growth of bct Cu with near-perfect lattice match, do not give rise to a CO adsorption site change on the Pd(100) terraces.

The STM, LEED and AES data of chapter 7.2 suggest intermixing when Cu is deposited on Pd(100) at temperatures $T_S \geq 500\text{K}$. Fig.7.14a shows the corresponding CO adsorption spectra. The Cu deposition temperature was 600K, the spectra for $T_{Dep}=500\text{K}$ (not shown) are very similar. The most conspicuous difference to the 300K data is the behaviour of the Pd bridge band. After an initial decrease, the band intensity remains constant for Cu coverages between 0.6 and 1.2ML (fig.7.15). At $\Theta_{Cu}=2\text{ML}$, Pd bridge sites are still available. The formation of 3D Cu clusters above $\Theta_{Cu}=0.6$, leaving parts of the Pd substrate uncovered, can be excluded from the STM measurements. So the present IR data are an additional confirmation for the formation of an intermixed CuPd phase at $T_S \geq 500\text{K}$. Above 2000cm^{-1} , three different absorption bands are present. A band at 2100cm^{-1} increases continuously in intensity and is the only band remaining upon Cu deposition of $>2\text{ML}$. Its frequency is constant up to this coverage and decreases slowly to 2095cm^{-1} at $\Theta_{Cu}=5$. Two weak shoulders at 2130cm^{-1} and 2080cm^{-1} are observed for $\Theta_{Cu} \leq 2\text{ML}$. The frequency of the latter decreases with increasing Θ_{Cu} (2050cm^{-1} at $\Theta_{Cu}=1.4$) whereas the frequency of the former does not change with Θ_{Cu} . Upon annealing (fig.7.14b), first the high frequency shoulder disappears at 250K. The CO molecules giving rise to the strong band at 2100cm^{-1} desorb only upon heating to temperatures above 300K.

The assignment of the absorption bands to the different adsorption sites in the

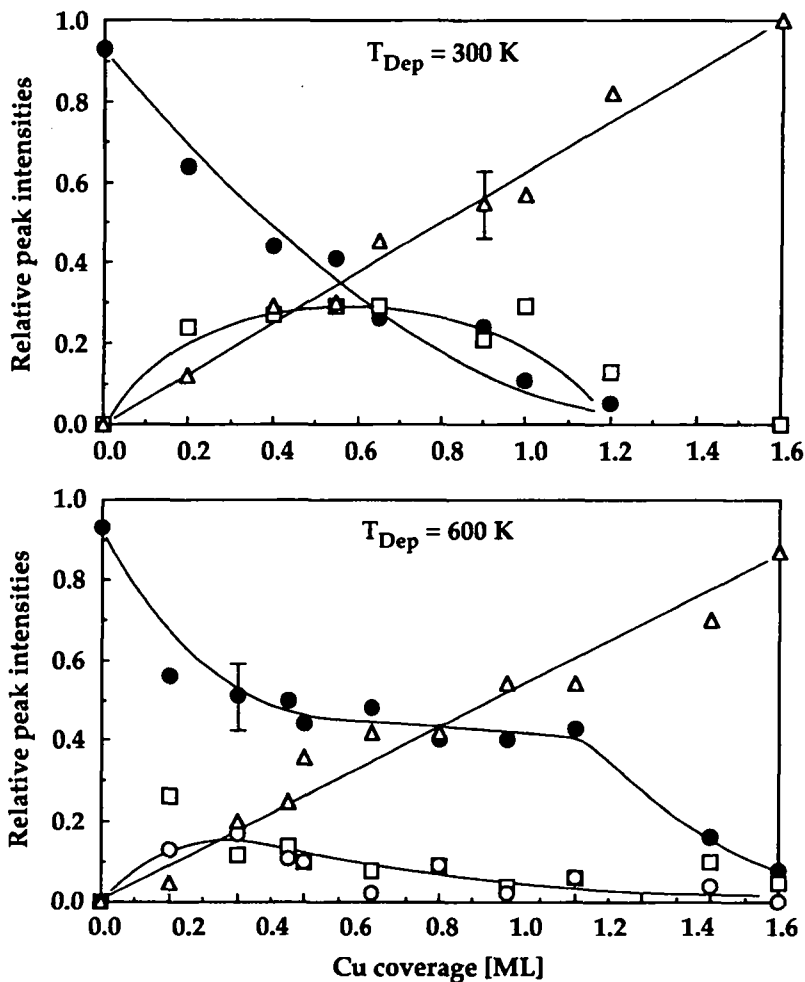


Fig.7.15: Integrated relative intensities of the infrared absorption bands of CO on Cu/Pd(100). Top: Cu deposition temperature 300K. Triangles: CO on large Cu islands. Squares: CO on Cu clusters. Full circles: CO on Pd bridge sites. Bottom: Cu deposition temperature 600K. Full circles: CO on Pd bridge sites. Triangles: band at 2100cm^{-1} . Open circles: shoulder at 2080cm^{-1} . Squares: shoulder at 2130cm^{-1} .

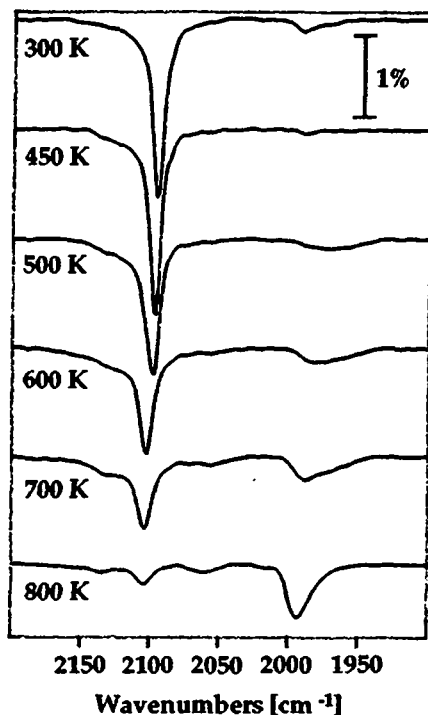


Fig.7.16: RAIRS spectra of CO adsorbed at $T_S=150\text{K}$ on 1.0ML Cu deposited at 600K (top spectrum) and on 1.0ML Cu annealed at the indicated temperatures. Resolution 4cm^{-1} , 400 scans averaged.

CuPd mixture is not trivial since the exact structure and composition of the mixture as a function of Θ_{Cu} and T_S is not yet known. The occurrence of Pd bridge sites up to high Cu coverages confirms that the mixture is not complete, but rather consists of small clusters, attributed to pure Pd and Pd alloyed with Cu. The Pd bridge band broadens considerably with increasing Θ_{Cu} , suggesting that the Pd clusters in the uppermost layer become smaller when more Cu is deposited and becomes alloyed with Pd. The band at 2100cm^{-1} , growing in intensity with increasing Cu coverage, is assigned to CO molecules on CuPd clusters, characterized by an "average" desorption temperature. At higher coverages ($\Theta_{\text{Cu}} \geq 2$), the mixture becomes Cu rich before pure

layers Cu are growing on top of the mixed layers. This results in a sharpening of the absorption band and a shift to lower frequencies. The two shoulders at 2130cm^{-1} and 2080cm^{-1} likely correspond to CO molecules on top of Cu and Pd atoms at cluster edges.

Fig.7.16 shows an annealing experiment at high temperatures. 1ML Cu was deposited at $T_S=300\text{K}$ and saturated with CO upon cooling the sample to 150K. The corresponding RAIR spectrum is shown at the top of the figure. Subsequently, the crystal was annealed for 60s at the indicated temperatures before dosing it to CO upon recooling to 150K. After an anneal at 450K, the small absorption band characterizing CO molecules on Pd bridge sites has nearly disappeared. This indicates a smoothing of the first Cu layer, the holes which remained in the first Cu layer upon deposition at room temperature are filled up. An anneal at 500K results in the onset of surface alloying, indicated by the reappearance of the Pd-CO signal. When the annealing temperature is increased furthermore, the two shoulders at 2130cm^{-1} and 2060cm^{-1} appear, whereas the Cu-CO band at 2100cm^{-1} broadens considerably and its intensity decreases. Upon heating the crystal to 800K and subsequent CO adsorption, the Pd bridge band is the dominant feature in the spectrum. The measurements suggest that, in analogy with the Cu/Pd(110) system, the CuPd surface alloy formation is followed by a diffusion of Cu into the Pd bulk, however at much lower temperatures.

8. Outlook

In this thesis, combined scanning tunneling microscopy and reflection absorption infrared spectroscopy studies of the morphology of Pt and Cu/Pd surfaces and the adsorption properties of molecules on these surfaces were presented.

In a further step, reactions between simple molecules on Cu/Pd as a function of surface morphology will be investigated in order to identify active sites and possible reaction schemes. For this purpose, the experimental setup will be continuously refined. The infrared spectrometer has already been equipped with hard- and software for time-resolved measurements (maximum recording speed 20 spectra/sec). An additional vacuum chamber containing a pulsed molecular beam source providing millisecond gas pulses is currently build, by means of which one of the reactants can be deposited onto the surface. Source and spectrometer are synchronized by a trigger pulse, thus the reaction on the surface can be followed on a fast time-scale. The extension of the STM working temperature range will be another experimental refinement. The STM/RAIRS apparatus will be provided by a special sample manipulator developed in our group [Röd93,3], allowing STM experiments at temperatures down to 25 K by means of mechanical decoupling of sample holder and cryostat.

Future investigations concern the following fields: the STM/RAIRS combination is particularly appropriate for studies of the deposition of metal films by chemical vapour deposition (CVD). By infrared spectroscopy, the decomposition of organometallic molecules on the sample surface can be followed as a function of temperature. When the decomposition is complete, the metal film left behind on the surface can be investigated by STM. Finally it is noted that the STM/RAIRS combination is not restricted to the study of metal surfaces. Recently it has been shown that epitaxial silicon films can be grown on previously prepared metal silicide samples [Erl91]. Because of the high reflectance of these samples, the silicon surfaces are accessible to IR spectroscopy in external reflection geometry. Thus the STM/RAIRS apparatus can be used in the present form to study silicide and semiconductor surfaces.

References

- [And91] J.A.Anderson and C.H.Rochester; *J.Chem.Soc.Faraday Trans.* **87**, 1485 (1991)
- [Adz92] R.R.Adzic, M.W.Hsiao, E.B.Yeager and G.Pruett; *Surf.Sci.* **273**, L425 (1992)
- [Ave83] N.R.Avery; *Surf.Sci.***131**, 501 (1993)
- [Bar87] M.E.Bartram, R.G.Windham and B.E.Koel; *Surf.Sci.* **184**, 57 (1987)
- [Bar89] M.E.Bartram and B.E.Koel; *Surf.Sci.* **213**, 137 (1989)
- [Bar90,1] N.C.Bartelt, T.L.Einstein and E.D.Williams; *Surf.Sci.* **240**, L591 (1990)
- [Bar90,2] J.V.Barth, H.Brune, G.Ertl and R.J.Behm; *Phys.Rev.B* **42**, 9307 (1990)
- [Bau58] E.Bauer; *Z.Kristallographie* **110**, 372 (1958)
- [Ber75] S.L.Bernasek and G.A.Somorjai; *J.Chem.Phys.* **62**, 3149 (1975)
- [Ber87] S.L.Bernasek, K.Lenz, B.Poelsema and G.Comsa; *Surf.Sci.* **183**, L319 (1987)
- [Ber92] W.Berndt and A.M.Bradshaw; *Surf.Sci.* **279**, L165 (1992)
- [Bes86] K.Besocke; *Surf.Sci.* **181**, 145 (1986)
- [Bin82] G.Binnig und H.Rohrer; *Helv.Phys.Acta* **55**, 726 (1982)
- [Bly64] G.Blyholder; *J.Phys.Chem.* **68**, 2772 (1964)
- [Bor89] V.Bortolani, V.Celli, A.Franchini, J.Idiodi, G.Santoro, K.Kern, B.Poelsema and G.Comsa; *Surf.Sci* **208**, 1 (1989)
- [Bot93] M.Bott, M.Hohage, T.Michely and G.Comsa; *Phys.Rev.Lett.* **70**, 1489 (1993)
- [Bra78] A.M.Bradshaw and F.M.Hoffman; *Surf.Sci.* **72**, 513 (1978)
- [Buc93] J.P.Bucher, E.Hahn, P.Fernandez, C.Massobrio and K.Kern; submitted (1993)
- [Cha85] Y.J.Chabal; *Phys.Rev.Lett.* **55**, 845 (1985)
- [Cha93] D.D.Chambliss, K.E.Johnson, R.J.Wilson and S.Chiang; *Journal of magnetism and magnetic materials* **121**, 1 (1993)
- [Che85] M.A.Chesters, G.S.McDougall, M.E.Pemle and N.Sheppard; *Surf.Sci.* **164**, 425 (1985)

- [Che88] J.R.Chelikowsky and M.Y.Chou; *Phys.Rev.B* **38**, 7966 (1988)
- [Che91] C.J.Chen; *J.Vac.Sci.Technol.* **A9**, 44 (1991)
- [Cho91] K.I.Choi and M.A.Vannice; *J.Catal.* **131**, 36 (1991)
- [Col77] D.M.Collins and W.E.Spicer; *Surf.Sci.* **69**, 85 (1977)
- [Com79] G.Comsa, G.Mechtersheimer, B.Poelsema and S.Tomoda; *Surf.Sci.* **89**, 123 (1979)
- [Com80] G.Comsa, G.Mechtersheimer and B.Poelsema; *Surf.Sci.* **97**, L297 (1980)
- [Com82] G.Comsa, G.Mechtersheimer and B.Poelsema; *Surf.Sci.* **119**, 159 (1982)
- [Cor90] J.C.L.Cornish and N.R.Avery; *Surf.Sci.* **235**, 209 (1990)
- [Cro93] M.F.Crommie, C.P.Lutz and D.M.Eigler; *Nature* **363**, 524 (1993)
- [Dam87] C.Damerow and W.Erley; *J.Vac.Sci.Technol.* **A5**, 2974 (1987)
- [Das86] J.G.Dash; *J.Vac.Sci.Technol.* **A4**, 1523 (1986)
- [Eig93] D.M.Eigler; unpublished (1993)
- [Eis58] R.P.Eischens and W.A.Pliskin; *Adv.Catal.* **10**, 1 (1958)
- [Eng91] W.Engel, M.E.Kordesch, H.H.Rotermund, S.Kubala and A.v.Oertzen; *Ultramicrosc.* **36**, 148 (1991)
- [Erl91] W.Erley, R.Butz and S.Mantl; *Surf.Sci.* **248**, 193 (1991)
- [Ern92] H.J.Ernst, F.Fabre and J.Lapujoulade; *Phys.Rev.B* **46**, 1929 (1992)
- [Ert77] G.Ertl, M.Neumann and K.M.Streit; *Surf.Sci.* **64**, 393 (1977)
- [Est31] I.Estermann, O.Frisch and O.Stern; *Z.Phys.* **73**, 348 (1931)
- [Far81] R.F.C.Farrow, D.S.Robertson, G.M.Williams, A.G.Cullis, G.R.Jones, I.M.Young and P.N.J.Dennis; *J.Cryst.Growth* **54**, 507 (1981)
- [Fen89] X.H.Feng, M.R.Yu, S.Yang, G.Meigs and E.Garfunkel; *J.Chem.Phys.* **90**, 7516 (1989)
- [Fis80] G.B.Fisher and J.L.Gland; *Surf.Sci.* **94**, 446 (1980)
- [For85] J.S.Foord and P.D.Jones; *Surf.Sci.* **152/153**, 487 (1985)
- [Fow28] R.H.Fowler and L.W.Nordheim; *Proc.Roy.Soc.A* **119**, 173 (1928)

- [Fro89] J.Frohn, J.F.Wolf, K.Besocke and M.Teske; *Rev.Sci.Instrum.* **60**, 1200 (1989)
- [Gad84] J.W.Gadzuk and A.C.Luntz; *Surf.Sci.* **144**, 429 (1984)
- [Gar89] E.Garfunkel, M.Yu, S.Yang and X.Feng; *J.Vac.Sci.Technol.* **A7(3)**, 1579 (1989)
- [Gau92] A.Gaussmann and N.Kruse; *Surf.Sci.* **279**, 319 (1992)
- [Gil81] W.D.Gillespie, R.K.Herz, E.E.Petersen and G.A.Somorjai; *J.Catal.* **70**, 147 (1981)
- [Gre66] R.G.Greenler; *J.Chem.Phys.* **44(1)**, 310 (1966)
- [Gri75] P.R.Griffiths; *Appl.Spectrosc.* **29**, 11 (1975)
- [Gri86] P.R.Griffiths and J.A. de Haseth; "Fourier Transform Infrared Spectroscopy", Wiley, New York (1986)
- [Gün93] C.Günther, S.Günther, E.Kopatzki, R.Q.Hwang, J.Schröder, J.Vrijmoeth and R.J.Behm; *Ber.Bunsenges.Phys.Chem.* **97**, 522 (1993)
- [Guo89] X.Guo and J.T.Yates; *J.Chem.Phys.* **90**, 6761 (1989)
- [Haa91] O.Haase, R.Koch, M.Borbonus and K.H.Rieder; *Ultramicrosc.* **42-44**, 541 (1991)
- [Hah90] E.Hahn; Diplomarbeit, University of Bonn (1990)
- [Hah93] E.Hahn, A.Fricke, H.Röder and K.Kern, *Surf.Sci.* **297**, 19 (1993)
- [Hah94,1] E.Hahn, E.Kampshoff and K.Kern; *Chem.Phys.Lett.*, in press (1994)
- [Hah94,2] E.Hahn, H.Schief, V.Marsico, A.Fricke and K.Kern; submitted (1994)
- [Hah94,3] E.Hahn, E.Kampshoff, A.Fricke, J.P.Bucher and K.Kern; submitted (1994)
- [Han58] M.Hansen, "Constitution of binary alloys", McGraw Hill, New York (1958)
- [Han91] L.Hansen, P.Stoltze, K.W.Jacobsen and J.K.Nørskov; *Phys.Rev.B* **44**, 6523 (1991)
- [Har84] C.Harendt, J.Goschnick and W.Hirschwald; *Surf.Sci.* **152/153**, 453 (1985)
- [Has93] Y.Hasegawa and Ph.Avouris; *Phys.Rev.Lett.* **71**, 1071 (1993)
- [Hay85,1] B.E.Hayden; "Reflection Absorption Infrared Spectroscopy"; in "Vibra-

- tional Spectroscopy of Molecules on Surfaces", Eds. J.T.Yates and T.E.Madey, Plenum Press, New York (1985)
- [Hay85,2] B.E.Hayden, K.Kretschmar, A.M.Bradshaw and R.G.Greenler; *Surf.Sci.* **149**, 394 (1985)
- [He 90] J.W.He, W.L.Shea, X.Jiang and D.W.Goodman, *J.Vac.Sci.Technol.* **A8**, 2435 (1990)
- [He 91] J.W.He, W.K.Kuhn, L.W.H.Leung and D.W.Goodman; *J.Vac.Sci.Technol.* **A9**, 1742 (1991)
- [Hec74] E.Hecht; "Optics", Addison-Wesley, New York (1974)
- [Hei90] J.Heidberg, E.Kampshoff, R.Kühnemuth, O.Schönekeas and M.Suhren; *J.Electr.Spectr.Rel.Phenom.* **54/55**, 945 (1990)
- [Hen89] M.A.Henderson, A.Szabó and J.T.Yates,Jr.; *J.Chem.Phys* **91**, 7245 (1989)
- [Her45] G.Herzberg; *Infrared and raman spectra*, Van Nostrand, New York (1945)
- [Hir90] C.J.Hirschmugl, G.P.Williams, F.M.Hoffmann and Y.J.Chabal; *Phys.Rev. Lett.* **65**(4), 480 (1990)
- [Hof87,1] F.M.Hoffmann and J.Paul; *J.Chem.Phys.* **86**(5), 2990 (1987)
- [Hof87,2] D.A.Hoffman and J.B.Hudson, *Surf.Sci.* **180**, 77 (1987)
- [Hog88] D.Hoge, M.Tüshaus and A.M.Bradshaw; *Surf.Sci.* **207**, L935 (1988)
- [Hör93] H.Hörnig, J.R.West, E.H.Conrad and R.Ellialtıoğlu; *Phys.Rev.B* **47**, 13055 (1993)
- [Hu 90] P.Hu, L.Morales de la Graza, R.Raval and D.A.King; **249**, 1 (1991)
- [Hul92] E.Hulpke (Ed.); *Helium atom scattering from surfaces*, Springer series in surface science 27 (1992)
- [Jac62] J.D.Jackson; *Classical electrodynamics*, Wiley, New York (1962)
- [Jay83] C.Jayaprakash, W.F.Saam and S.Teitel; *Phys.Rev.Lett.* **50**, 2017 (1983)
- [Jia92] L.Q.Jiand, B.E.Koel and J.L.Falconer; *Surf.Sci.* **279**, 273 (1992)
- [Ker91] K.Kern, H.Niehus, A.Schatz, P.Zeppenfeld, J.Goerge and G.Comsa; *Phys.*

- Rev.Lett. **67**, 855 (1991)
- [Kuh90] W.K.Kuhn, J.W.He and D.W.Goodman; Chem.Phys.Lett. **172**, 331 (1990)
- [Kuh92,1] K.Kuhnke, E.Hahn, R.David, P.Zeppenfeld and K.Kern; Surf.Sci. **272**, 118 (1992)
- [Kuh92,2] W.K.Kuhn, J.Szanyi and D.W.Goodman; Surf.Sci. **274**, L611 (1992)
- [Lam90] D.K.Lambert and R.G.Tobin; Surf.Sci. **232**, 149 (1990)
- [Lan93] U.Landman; private communication (1993)
- [Lap91] J.Lapujoulade and B.Salanon; Phase transitions in surface films 2, Eds. H.Taub et al., Plenum, New York, p.217 (1991)
- [Len87] K.Lenz; Ph.D.Thesis, University of Bonn (F.R.G.), Jülich-Report 2141 (1987)
- [Li 89] H.Li, S.C.Wu, D.Tian, J.Quinn, Y.S.Li, F.Jona and P.M.Marcus; Phys.Rev.B **40**, 5841 (1989)
- [Liu91] Z.M.Liu, Y.Zhou, F.Solymosi and J.M.White; Surf.Sci. **245**, 289 (1991)
- [Luo92] J.S.Luo, R.G.Tobin, D.K.Lambert, G.B.Fisher and C.L.DiMaggio; Surf.Sci. **274**, 53 (1992)
- [Mad83] T.E.Madey, N.R.Avery, A.B.Anton, B.H.Toby and W.H.Weinberg; J.Vac. Sci.Technol.A **1**(2), 1220 (1983)
- [Mah78] G.D.Mahan and A.A.Lucas; J.Chem.Phys. **68**, 1344 (1978)
- [Mal85] C.M.Male and G.A.Somorjai; Surf.Sci. **160**, 542 (1985)
- [Mar92] V.I.Marchenko, JETP Lett. **55**, 73 (1992)
- [Mas93] C.Massobrio, P.Blandin, P.Fernandez and J.Buttet; submitted (1993)
- [McC77] R.W.McCabe and L.D.Schmidt; Surf.Sci. **66**, 101 (1987)
- [Men88] F.K.Men, W.E.Packard and M.B.Webb; Phys.Rev.Lett. **61**, 2469 (1988)
- [Mes82] R.P.Messner, S.H.Larmson and D.R.Salahub; Phys.Rev.B **25**, 3576 (1982)
- [Met79] "Metals handbook", American society for metals, Ohio (1979)
- [Mic91,1] A.A.Michelson; Phil.Mag.(5) **31**, 256 (1891)
- [Mic91,2] Th.Michely and G.Comsa; Surf.Sci. **256**, 217 (1991)

- [Mic93] T.Michely, M.Hohage, M.Bott and G.Comsa; *Phys.Rev.Lett.* **70**, 3943 (1993)
- [Mo 91] Y.W.Mo, J.Kleiner, M.B.Webb and M.G.Lagally; *Phys.Rev.Lett.* **66**, 1998 (1991)
- [Mor89] I.A.Morrison, M.H.Kang and E.J.Mele; *Phys.Rev.B* **39**, 1575 (1989)
- [Nee91] R.J.Needs, M.J.Godfrey and M.Mansfield; *Surf.Sci.* **242**, 215 (1991)
- [Ngu78] T.T.Nguyen and N.Shappard; in: "Advances in infrared and raman spectroscopy", Eds. R.E.Hesler and R.H.J.Clark, Vol.5, Heyden, London (1978)
- [Ora89] B.Oral, R.Kothari and R.W.Vook; *J.Vac.Sci.Technol.* **A7**, 2020 (1989)
- [Ora90] B.Oral and R.W.Vook; *Vacuum* **41**, 227 (1990)
- [Pac91] G.Pacchioni, G.Cogliandro and P.S.Bagus; *Surf.Sci.* **255**, 344 (1991)
- [Par90] D.H.Parker, D.A.Fisher, J.Colbert, B.E.Koel and J.L.Gland; *Surf.Sci.* **236**, L372 (1990)
- [Par91] D.H.Parker, D.A.Fisher, J.Colbert, B.E.Koel and J.L.Gland; *Surf.Sci.* **258**, 75 (1991)
- [Per81] B.N.J.Persson and R.Ryberg; *Phys.Rev.B* **24**, 6954 (1981)
- [Per92] B.N.J.Persson; *Chem.Phys.Lett.* **197(1,2)**, 7 (1992)
- [Pic59] H.L.Pickering and H.C.Eckstrom; *J.Phys.Chem.* **63**, 512 (1959)
- [Pim92] A.Pimpinelli, J.Villain and D.E.Wolf; *Phys.Rev.Lett.* **69**, 985 (1992)
- [Pin93] H.M. van Pinxteren and J.W.M.Frenken; *Europhys.Lett.* **21**, 43 (1993)
- [Poe81] B.Poelsema, G.Mechtersheimer and G.Comsa; *Surf.Sci.* **111**, 519 (1981)
- [Poe83] B.Poelsema and G.Comsa; *Scattering of thermal energy atoms from disordered surfaces*, Springer tracts 115 (1983)
- [Poe86] B.Poelsema, L.S.Brown, K.Lenz, L.K.Verheij and G.Comsa; *Surf.Sci.* **171**, L395 (1986)
- [Poe90] M.Poensgen, M.Giesen, J.Frohn and H.Ibach; *Phys.Rev.Lett.* **65**, 733 (1990)
- [Poe91] B.Poelsema, R.Kunkel, N.Nagel, A.F.Becker, G.Rosenfeld, L.K.Verheij and G.Comsa; *Appl.Phys.A* **53**, 369 (1991)

- [Pri78] J.Pritchard, in: "Vibrations in adsorbed layers", KFA Jülich conference records series, Eds. H.Ibach and S.Lehwald, p.114 (1978)
- [Pri85] G.A.Prinz; Phys.Rev.Lett. **54**, 1051 (1985)
- [Rav89] R.Raval, M.A.Harrison and D.A.King; Surf.Sci. **211/212**, 61 (1989)
- [Reu88] J.E.Reutt, Y.J.Chabal and S.B.Christman; Phys.Rev.B **38**, 3112 (1988)
- [Rod91] J.A.Rodriguez and D.W.Goodman; J.Phys.Chem. **95**, 4196 (1991)
- [Rod92] J.A.Rodriguez, C.M.Truong and D.W.Goodman; J.Chem.Phys. **96**, 7814 (1992)
- [Röd91] H.Röder; Diplomarbeit, University of Bonn, 1991
- [Röd93,1] H.Röder, R.Schuster, H.Brune and K.Kern; Phys.Rev.Lett **71**, 2086 (1993)
- [Röd93,2] H.Röder, E.Hahn, H.Brune, J.P.Bucher and K.Kern; Nature **366**, 141 (1993)
- [Röd93,3] H.Röder, H.Brune, J.P.Bucher and K.Kern; Surf.Sci. **298**, 121 (1993)
- [Rou92] S.Rousset, S.Gauthier, O.Siboulet, J.C.Girard, S.de Cheveigné, M.Huerta-Garnica, W.Sacks, M.Belin and J.Klein; Ultramicrosc. **42-44**, 515 (1992)
- [Ryb89] R.Ryberg; Adv.Chem.Phys. **76**, 1 (1989)
- [San91] D.E.Sanders and A.E.DePristo; Surf.Sci. **260**, 116 (1991)
- [San93] A.R.Sandy, S.G.J.Mochrie, D.M.Zehner, G.Grübel, K.G.Huang and D.Gibbs; Phys.Rev.Lett. **68**, 2192 (1992)
- [Sau81] R.Sau and J.B.Hudson; J.Vac.Sci.Technol. **18**, 607 (1981)
- [Sch86] U.Schwalke, J.E.Parmeter and W.H.Weinberg; J.Chem.Phys. **84**, 4036 (1986)
- [Sch89] E.Schweizer, B.N.J.Persson, M.Tüshaus, D.Hoge and A.M.Bradshaw; Surf. Sci. **213**, 49 (1989)
- [Sch90] P.J.Schmitz, H.C.Kang, W.Y.Leung and P.A.Thiel; Surf.Sci. **248**, 287 (1991)
- [Sel93] A.Sellidj and B.E.Koel; Surf.Sci.**284**, 139 (1993)
- [Sib93] S.J.Sibener; private communication (1993)
- [Sin83] J.H.Sinfelt; "Bimetallic catalysts" , Wiley, New York (1983)

- [She88] I.Sherrington and E.H.Smith; *Wear* **125**, 271 (1988)
- [Som33] A.Sommerfeld and H.Bethe; in: "Handbuch der Physik von Geiger und Scheel", Volume 24/2, Springer, Berlin (1933)
- [Ste82] H.Steiningcr; Ph.D.Thesis, University of Aachen (F.R.G.), Jülich- Report 1763 (1982)
- [Swe78] R.W.Swendson; *Phys.Rev.B* **17**, 3710 (1978)
- [Tak80] M.Takagi-Kawai, M.Soma, T.Onishi and K.Tamaru; *Can.J.Chem.* **58**, 2132 (1980)
- [Ter83] J.Tersoff and D.R.Hamann; *Phys.Rev.Lett.* **50**, 1998 (1983)
- [Tso92] T.T.Tsong, J.Liu and C.W.Wu; in: "Physics and chemistry of finite systems: from clusters to crystals", Eds. P.Jena et al., Kluwer, Dordrecht, p.1039 (1992)
- [Tüs88] M.Tüshaus, E.Schweizer, P.Hollins and A.M.Bradshaw; *J.Electron Spectrosc.Rel.Phenom.* **44**, 305 (1987)
- [Van93] D.Vanderbilt, in: "Computations for the nano-scale", eds. P.E.Blöchl et al., Kluwer, N.Y., p.1 (1993)
- [Ver92] L.K.Verheij, M.Freitag, M.B.Hugenschmidt, I.Kempf, B.Poelsema and G.Comsa; *Surf.Sci.* **272**, 276 (1992)
- [Wan87] Z.Q.Wang, S.H.Lu, Y.S.Li, F.Jona and P.M.Marcus; *Phys.Rev.B* **35**, 9322 (1987)
- [Wan93,1] S.C.Wang and G.Ehrlich; *Phys.Rev.Lett.* **71**, 4174 (1993)
- [Wan93,2] A.Wander, P.Hu and D.A.King; *Chem.Phys.Lett.* **201**, 393 (1993)
- [Wat93] G.M.Watson, D.Gibbs, D.M.Zehner, M.Yoon and S.G.J.Mochrie; *Phys.Rev.Lett.* **71**, 3166 (1993)
- [Wee80] J.D.Weeks, in: "Ordering in strongly fluctuating condensed matter systems", Ed. T.Riste, Plenum, New York, p.293 (1980)
- [Wes86] D.A.Wesner, G.Pirug, F.P.Coenen and H.P.Bonzel; *Surf.Sci.* **178**, 608 (1986)
- [Whe92] A.A.Wheeler, C.Ratsch, A.Morales, H.M.Cox and A.Zangwill; *Phys.Rev.B*

46, 2428 (1992)

[Wil91] E.D.Williams and N.C.Bartelt; *Science* **251**, 393 (1991)

[Win89] J.Wintterlin, J.Wiechers, H.Brune, T.Gritsch, H.Höfer and R.J.Behm; *Phys. Rev.Lett.* **62**, 59 (1989)

[Win93] J.Wintterlin and Ph.Avouris; *Surf.Sci.* **286**, L529 (1993)

[Wol78] E.L.Wolf; *Rep.Prog.Phys.* **41**, 1439 (1978)

[Wol87] M.Wolf, A.Goschnik, J.Loboda-Cacković, M.Grunze, W.N.Unertl and J.H. Block; *Surf.Sci.* **182**, 489 (1987)

[Wol88] R.Wolkow and Ph.Avouris; *Phys.Rev.Lett.* **60**, 1049 (1988)

[Woo82] D.P.Woodruff, B.E.Hayden, K.Prince and A.M.Bradshaw; *Surf.Sci.* **123**, 397 (1982)

[Wu 88] S.C.Wu, S.H.Lu, Z.Q.Wang, C.K.C.Lok, J.Quinn, Y.S.Li, D.Tian, L.Jona and P.M.Marcus; *Phys.Rev.B* **38**, 5363 (1988)

[Zan88] A.Zangwill; "Physics at surfaces", Cambridge University Press (1988)

[Zep93] P.Zeppenfeld, M.Krzyzowski, C.Romainczyk, G.Comsa and M.G.Lagally; submitted (1993)

Merci!!

Je tiens à exprimer ma gratitude aux personnes qui ont contribué à l'élaboration de cette thèse:

- M. le Prof. K.Kern, mon directeur de thèse, pour son engagement tout au long de ce travail et les inombrables et passionnantes discussions;
- L'équipe des post-docs, Mlle E.Kampshoff, M. J.P.Bucher et M. A.Fricke pour leur collaboration;
- M. H.Röder, qui a construit le microscope à effet tunnel et le cryostat pendant son travail de diplôme et qui a participé par *deux fois* au montage du système UHV;
- Mlle C.-L. Bandelier, M. M.Fazan, M. A.Guisolan et tous les collaborateurs des ateliers de mécanique et d'électronique pour leur précieuse contribution.

La première année de ma thèse s'étant déroulée au KFA Jülich en Allemagne, je tiens donc également à remercier

- M. le Prof. G.Comsa pour son soutien pendant cette période;
- les collaborateurs de l'atelier mécanique de l'IGV pour avoir construit les chambres UHV

Je ne saurais naturellement oublier les doctorant(e)s et diplomant(e)s tant à Lausanne qu'à Jülich pour avoir créé une bonne atmosphère (aussi au travail). Finalement je remercie particulièrement mes parents qui m'ont permis d'entreprendre mes études ainsi que l'Ecole Polytechnique Fédérale de Lausanne, le Fonds National Suisse et la Deutsche Forschungsgemeinschaft pour leur soutien financier durant ce travail de thèse.

Curriculum vitae

Nom et prénom: Hahn Elmar
Date de naissance: 14 mai 1965
Lieu de naissance: Prüm (Allemagne)
Origine: Allemagne
Etat civil: Célibataire
Adresse actuelle: Avenue de Préfaully 25c
1022 Chavannes-près-Renens

Formation

1971-1975 Ecole primaire à Prüm (Allemagne)
1975-1984 Gymnase à Prüm (Allemagne), Abitur en 1984
1984-1985 Service militaire
1985-1989 Etudes de physique à l'Université de Bonn (Allemagne)
1989-1990 Travail de diplôme, effectué sous la direction de Prof.G.Comsa au KFA Jülich (Allemagne)
Titre "Diplom-Physiker" obtenu en 1990
1990-1991 Début de la thèse de doctorat au KFA Jülich sous la direction de Prof.K.Kern
1991-1994 Suite de la thèse de doctorat à l'Ecole Polytechnique Fédérale de Lausanne, assistant de cours

Domaines de recherche

"Monochromatisierung thermischer Heliumstrahlen" (Travail de diplôme)
"Structure and reactivity of vicinal Pt and low-index Cu/Pd surfaces" (Thèse de doctorat)

